# Spin Coherence in Graphene Quantum Dots

Matthias Droth

Juni 2010

Diplomarbeit im Studiengang Physik

| | |
|---|---|
| Betreuer und erster Gutachter: | Prof. Dr. Guido Burkard |
| Zweiter Gutachter: | Prof. Dr. Wolfgang Belzig |

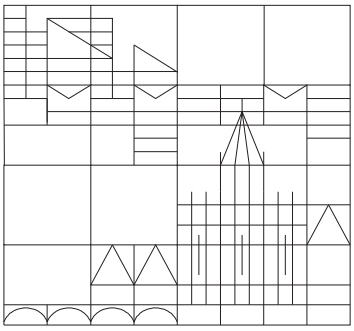

Universität Konstanz
LS Burkard

# Erklärung

1. Ich versichere hiermit, dass ich die vorliegende Arbeit mit dem Thema

   Spin Coherence in Graphene Quantum Dots

   selbständig verfasst und keine anderen Hilfsmittel als die angegebenen benutzt habe. Die Stellen, die anderen Werken dem Wortlaut oder dem Sinne nach entnommen sind, habe ich in jedem einzelnen Falle durch Angaben der Quelle, auch der benutzten Sekundärliteratur, als Entlehnung kenntlich gemacht.

2. Diese Arbeit wird nach Abschluss des Prüfungsverfahrens der Universitätsbibliothek Konstanz übergeben und ist durch Einsicht und Ausleihe somit der Öffentlichkeit zugänglich. Als Urheber der vorliegenden Arbeit stimme ich diesem Verfahren zu.

Konstanz, 30. Juni 2010, _____

Matthias Droth

# Acknowledgements

This diploma thesis and my studies of physics would not have been possible without support from many people. I also owe gratitude to those who have made the years of study such an awesome time. Proper respect to

- Prof. Guido Burkard for the interesting topic and supervision and Prof. Wolfgang Belzig for co-supervision.
- Prof. Robert Denk and Michael Pokojovy for help with the wave equations and boundary conditions.
- The entire Burkard group and Luca Chirolli for illuminating discussions about physics, a good time and motorboat sessions.
- Maria Rosner for administration and keeping everything in control.
- Nathalie Feiner, Hans Recknagel and Julia Hildmann for proofreading.
- Joe Duffy, Shelley Thompson, Kristen Conley, Callum Spence, Irene Heeß, François Grobel and Jakob Kümmel for inspiration, adventures and being.

Very special thanks to my parents and siblings for their inexhaustible support that I have always been able to rely on.

# Abstract

Quantum computing requires long coherence times. A spintronics approach is considered promising due to the readily available expertise in solid state physics and possibly long coherence times [Loss (1998), DiVincenzo (1999)]. We investigate a qubit implementation as real electron spin in graphene nanoribbon (GNR) quantum dots (QD). This system is particularly interesting because it allows for non-local QD coupling and a high threshold for fault-tolerant quantum computing [Trauzettel (2007), Svore (2005)]. QD electron spin coherence is determined by the coupling to nuclear spins and the lattice. Due to the vanishing nuclear spin of $^{12}$C, coupling to the lattice is particularly important in carbon based materials.

In a magnetic field, spin states $|\uparrow\rangle$ and $|\downarrow\rangle$ are split by the Zeeman energy $g\mu_B B$, which needs to be absorbed by the lattice to allow for a spin flip. This requires an effective spin-phonon coupling, which we assume to occur via spin-orbit and electron-phonon interaction as previously proposed [Khaetskii (2001)]. For magnetic fields perpendicular to the GNR plane only Rashba-type spin-orbit coupling contributes in lowest order. Starting from a continuum model, we derive a full phonon field theory for acoustical ribbon modes at the center of the Brillouin zone. Due to open boundary conditions at the edges of the quasi-one-dimensional GNR, the usual $q^2$-dependence for out-of-plane modes in bulk is cut off at the zone center, where we find a linear dispersion. The transverse and longitudinal sound velocities of the in-plane modes match well with literature values for comparable systems [Falkovsky (2008), Sánchez-Portal (1999)]. As expected, all modes approach bulk behavior for wavelengths much smaller than the ribbon width. In lowest order, only in-plane modes locally dilate or compress the GNR, thereby contributing to the electron-phonon coupling deformation potential which we express in terms of ribbon phonon creators and annihilators.

All couplings are treated completely analytically and we find Van Vleck cancellation, as expected for this time-reversal symmetry conserving system [Van Vleck (1940)]. To calculate the relaxation rate $\Gamma_1$ via Fermi's Golden Rule a quasi-continuous spectrum of final states is required. This is ensured by the vanishing dependence of the rate on the ribbon length, thus allowing for a continuous phonon spectrum. For conventional magnetic fields and ribbon widths ($B \sim 1\,\mathrm{T}$, $W \sim 30\,\mathrm{nm}$), $\Gamma_1$ goes with $B^5$ and $W^{-1}$ and relaxation times $T_1 = 1/\Gamma_1$ range from $180\,\mu\mathrm{s}$ to $43 \times 10^3\,\mathrm{s}$. These rather long times are caused by (i) a vanishing coupling to every second QD state, (ii) Van Vleck cancellation, (iii) the assumption of phononic vacuum (low temperatures) and (iv) a low density of states of the contributing modes and encourage a further study of this system, which so far seems to conform quantum computing coherence times.

# Zusammenfassung

Voraussetzung für einen Quantencomputer sind unter anderem lange Kohärenzzeiten der Qubits (kurz für Quanten-Bits). In dieser Hinsicht hat eine Realisierung in Form von Elektronenspins gute Aussichten, denn die Festkörperphysik ist etabliert und vielseitig - wie von klassischen elektronischen Anwendungen unter Beweis gestellt - und führt oft zu langen Kohärenzzeiten. Spin Qubits in Graphen Quantenpunkten wären eine konkrete Implementierung mit weiteren Vorteilen in Sachen Kohärenz und Kopplung entfernter Quantenpunkte. Weil Kernspin-Effekte in Kohlenstoff schwächer als in konventionellen Halbleitermaterialien (z.B. GaAs) sind, kommt der Spin-Relaxation durch Spin-Phonon-Kopplung eine wichtige Rolle zu.

In dieser Arbeit werden zunächst die elektronischen Eigenschaften von Graphen im Detail erklärt, insbesondere das quasi-relativistische Spektrum der Elektronen sowie das Klein Paradoxon. Der Spin-Bahn Hamiltonoperator wird aus der Orbitalstruktur hergeleitet und als Nebenprodukt dieser Berechnungen erhalten wir das Termschema der $n = 2$ Drehimpulsschale von Kohlenstoff, welche in Graphen einen $sp_2$-Hybrid mit entkoppelten $p_z$ Zuständen bildet. Die Entartung von bindenden und antibindenden $p_z$ Zuständen erklärt die verschwindende Energielücke in ausgedehntem Graphen. Für ein quasi eindimensionales Graphenband mit "Armchair"-Rändern ergibt sich, abhängig von der Anzahl der Atome entlang der Breite, Graphen mit bzw. ohne Bandlücke. Während es in Graphen ohne Bandlücke wegen dem Klein Paradoxon schwierig ist, Elektronen einzugrenzen, ist dies kein Problem in "Armchair"-Graphenbändern. Weiter wird das Energiespektrum von solch elektrostatisch eingegrenzten Elektronen hergeleitet: es existieren unendlich viele transversale Anregungen (d.h. Anregungen in Richtung der Breite), zu denen jeweils endlich viele longitudinale Anregungen gehören, abhängig von der Wahl der Eingrenzung.

Mit dem Ansatz eines Kontinuummodells leiten wir zum ersten Mal die Dispersion und explizite Form von Gitterschwingungen innerhalb der Graphenebene bzw. senkrecht dazu her. Dabei beschränken wir uns auf akustische Phononen im Zentrum der Brillouin Zone, wo atomare Distanzen vernachlässigbar gegenüber der Wellenlänge sind. Anders als in ausgedehntem Graphen, wo die Dispersion der Schwingung aus der Ebene heraus im Zonenzentrum quadratisch verläuft, verhält sich diese Schwingung im Graphenband linear. Alle Moden verhalten sich für genügend große Wellenzahlen wie in ausgedehntem Graphen. Die Schwingungen innerhalb der Graphenebene werden mit Phononerzeugern und -vernichtern quantisiert. Allein diese Moden tragen in führender Ordnung zum Deformationspotential, einem Elektron-Phonon Kopplungsmechanismus, bei. Wir drücken diesen Kopplungsmechanismus durch die entsprechenden Erzeuger und Vernichter von Bandphononen aus und bestätigen die Hermitezität dieses Operators.

Das Deformationspotential koppelt nicht direkt an den Spin. Eine Kombination von Elektron-Phonon Kopplung und Spin-Bahn Kopplung ermöglicht letztendlich jedoch einen Spin-Phonon Kopplungsmechanismus, über welchen die Zeeman Energie auf das Gitter übertragen werden kann. Beim "Admixture Mechanismus", welcher von Khaetskii und Nazarov vorgeschlagen wurde, verändert die Spin-Bahn Kopplung die Elektronzustände so, dass sich jeweils mehrere Bahnzustände zu neuen Zuständen überlagern. Indem es an

diese gemischten Zustände koppelt, kann das Deformationspotential den Elektronenspin umklappen. Das Mischen der Bahnzustände sowie die Kopplung des Deformationspotentials an diese gemischten Zustände werden analytisch und detailliert behandelt. Auch intrinsische Spin-Bahn Kopplung leistet einen Beitrag zum Mischen der Elektronzustände, jedoch nur in höherer Ordnung. In niedrigster Ordnung trägt der Zustand mit entgegengesetztem Spin und gleichem Bahnzustand nicht bei, was einer starken Unterdrückung des Admixture Mechanismus entspricht. Eine weitere Unterdrückung rührt von der Van Vleck Auslöschung her, welche erwartet wird, da die Elektronenzustände zeitumkehrsymmetrisch sind. Wir gehen von Phononenvakuum aus und davon, dass nur ein Phonon erzeugt wird, welches die gesamte Zeeman Energie aufnimmt. Die Zustandsdichte des einzigen beteiligten Dispersionzweiges ist bei der Zeeman Energie gering , was die Relaxation nochmals unterdrückt.

Die Relaxationsrate kann mit Hilfe Fermis Goldener Regel berechnet werden. Sie verhält sich invers proportional zu Breite des Bandes und ermöglicht so im Prinzip maßgefertigte Bauteile. Magnetfelder können i.d.R. über gut zwei Größenordnungen eingestellt werden, so dass die $B^5$-Abhängigkeit der Rate zu Kohärenzzeiten führt, die sich um etwa zehn Größenordnungen unterscheiden. Dieses Verhalten mit $B^5$ gilt nur für ein bestimmtes Parameterintervall, in welchem die Zeiten von $180\,\mu$s bis zu $43 \times 10^3$ s reichen. Für Parameter über das uns numerisch zugängliche Regime hinaus geben wir eine untere Grenze für die Kohärenzzeit an. Alle Werte genügen dem dritten DiVincenzo Kriterium und dies legt weitere Untersuchungen dieses Systems nahe, insbesondere da die Grundlagen nun im Detail verstanden sind.

# Contents

# 1. Introduction

Quantum information is based on the use of quantum bits - qubits - as the smallest unit of quantum mechanical information. Qubits are a generalization of classical bits in that they are an arbitrary superposition of 0 and 1,

$$|\psi\rangle = \alpha|0\rangle + \beta|1\rangle\,, \tag{1.1}$$

where the complex coefficients must satisfy $|\alpha|^2 + |\beta|^2 = 1$ to ensure a normalized state. Therefore, a qubit incorporates much more information than a classical bit and quantum computing aims at exploiting this feature. While it is easy to decompose the number 15 into prime factors 3 and 5 this task becomes more and more elaborate for large numbers and, for classical algorithms, practically impossible for sufficiently large integers[1]. Due to the far-reaching implications for cryptography, Peter Shor's 1994 discovery of an algorithm for solving this problem efficiently on a quantum computer has, among other promising applications, boosted interest for quantum information science.

This has culminated in significant progress of the whole field, including the proof-of-principle demonstration of Shor's algorithm on a small-scale quantum computer and the demonstration of quantum communication across a distance of 144 km. A recent proposal for space-to-ground quantum communications with the International Space Station and the appearance of commercially available quantum cryptosystems reveal the increasing maturity of the discipline. To enhance the status of quantum computing from technology demonstration to exploitation, a full-scale quantum computer is required. Such a device should conform a list of requirements, the five DiVincenzo criteria. It should have a

1. sufficient number of bits, allow for
2. initialization of the memory before each computation, have a
3. sufficiently low error rate and a
4. universal set of logic gates for computing and provide
5. reliable output of the final result.

Despite their intuitive and basic character, these requirements turn the construction of a quantum computer into a great challenge. From a physicist point of view, it is also worthwhile to work towards a quantum computer as this challenge inevitably leads to new theoretical and experimental insights into fundamental physics. New insights into qubit coherence, a translation of criterion 3 into physics language, are subject of this diploma thesis.

[1] We put the citations here to ensure readability of this introduction. RSA scheme: [Rivest (1978)]; Shor algorithm: [Shor (1994), Shor (1997)]; implementation of Shor algorithm: [Lanyon (2007), Lu (2007), Vandersypen (2001)]; demonstration of quantum teleportation: [Bennett (1993), Ursin (2004), Ursin (2007), Ursin (2009)]; commercial quantum cryptosystems: [IdqCerberis, Magiq8505]; DiVincenzo criteria: [DiVincenzo (1999)];

## 1.1. Qubit coherence

Coherence refers to the stability of a phase, which determines the interference of waves. A prominent application of coherence is the laser, where phase stability leads to constructive interference over large distances. Decoherence is the loss of coherence. Due to the wave character of quantum mechanics, coherence is intrinsically linked to qubits.

The third DiVincenzo criterion implies that the decoherence time of qubits should be $10^4$ times longer than the clock cycle [DiVincenzo (1999)]. While coherence is completely irrelevant to a classical computer, it does affect qubits and therefore it is crucial to quantum computing. The advantages of a quantum computer come at the necessity for coherent qubits (at least). We rewrite the qubit state in (1.1) as[2]

$$|\psi\rangle = \cos\frac{\theta}{2}|0\rangle + e^{i\phi}\sin\frac{\theta}{2}|1\rangle\,,$$

where $\theta$ determines the ratio $|\alpha|^2 : |\beta|^2$ and $\phi$ the relative phase. Both angles are real numbers and, together, parametrize the three-dimensional unit sphere, the Bloch sphere, figure 1.1 (a). The poles correspond to the two possible states of a classical bit. In contrast, the whole sphere is available for a qubit, [Nielsen & Chuang].

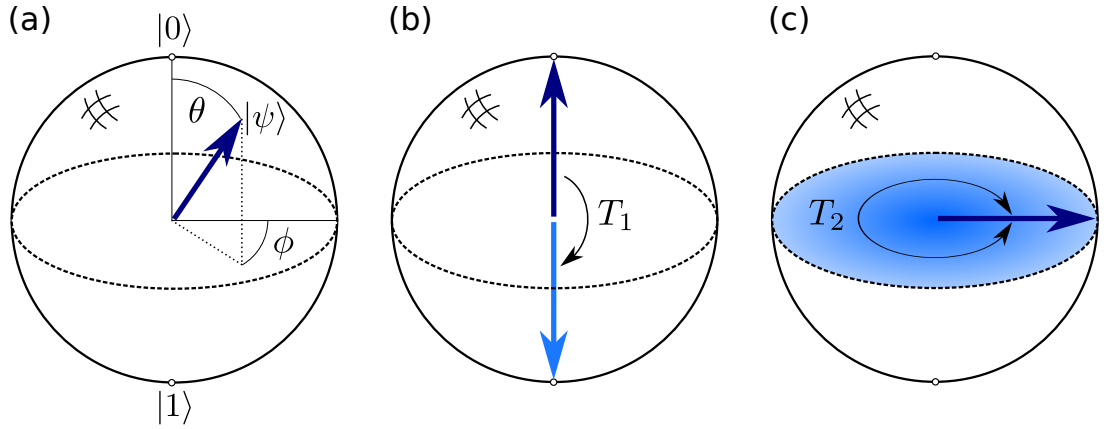


Figure 1.1.: (a): Each point on the Bloch sphere corresponds to a qubit state. The angle $\theta$ determines the contributions from $|0\rangle$ and $|1\rangle$ while $\phi$ denotes their relative phase. (b): For $E_0 > E_1$ the higher energy state $|0\rangle$ decays to $|1\rangle$ on the relaxation timescale $T_1$. This means that an initial superposition will eventually lose its $|0\rangle$ component and hence the relative phase $\phi$. (c): The phase may also fade without energy exchange, thus leading to a mixture of qubit states. Such effects further increase the decay rate of the off-diagonal elements in (1.2), which is characterized by the dephasing timescale $T_2$. If relaxation induced dephasing is the only contribution it follows that $T_2 = 2\,T_1$.

The Bloch sphere can be used to illustrate the meaning of the times $T_1$ and $T_2$, which characterize[3] the coherence of an initially well-defined qubit. If there is an energy differ-

[2] A common phase of both summands has no physical meaning and can be omitted.

[3] The authors of [DiVincenzo (1999)] refer to a set of twelve numbers in order to fully characterize the coherence of a qubit (in the markovian limit).

ence[4], say $E_0 > E_1$, the decay $|0\rangle \rightarrow |1\rangle$ is described by the relaxation time $T_1$, figure 1.1 (b). In particular, the relaxation process involves energy exchange. The dephasing time $T_2$ relates to the fading of $\phi$, which leads to a mixed state, figure 1.1 (c). No energy needs to be exchanged but the process is still irreversible as it leads to an increase of entropy.

Since coherence is the topic of this diploma thesis we go a little into detail. Initially, the qubit is represented by the density matrix

$$\rho(t=0) = |\psi\rangle\langle\psi| = \begin{pmatrix} \cos^2\frac{\theta}{2} & \cos\frac{\theta}{2}\sin\frac{\theta}{2}e^{-i\phi} \\ \cos\frac{\theta}{2}\sin\frac{\theta}{2}e^{i\phi} & \sin^2\frac{\theta}{2} \end{pmatrix} = \begin{pmatrix} |\alpha|^2 & \alpha\beta^* \\ \beta\alpha^* & |\beta|^2 \end{pmatrix}, \tag{1.2}$$

corresponding to a pure state. Due to dephasing, $\phi$ eventually smears out uniformly and the density matrix becomes a mixture of states of all phases,

$$\rho(t\rightarrow\infty) = \int_{\phi=0}^{2\pi}\frac{\mathrm{d}\phi}{2\pi}|\psi\rangle\langle\psi| = \int_{\phi=0}^{2\pi}\frac{\mathrm{d}\phi}{2\pi}\begin{pmatrix} \cos^2\frac{\theta}{2} & \cos\frac{\theta}{2}\sin\frac{\theta}{2}e^{-i\phi} \\ \cos\frac{\theta}{2}\sin\frac{\theta}{2}e^{i\phi} & \sin^2\frac{\theta}{2} \end{pmatrix} = \begin{pmatrix} |\alpha|^2 & 0 \\ 0 & |\beta|^2 \end{pmatrix}.$$

The off-diagonal elements vanish since $e^{i\phi} + e^{i(\phi+\pi)} = 0$. This is the effect of dephasing. Unaffected by this consideration, the relaxation $|0\rangle \rightarrow |1\rangle$ demands

$$\rho(t\rightarrow\infty) = \begin{pmatrix} 0 & 0 \\ 0 & 1 \end{pmatrix}.$$

Here, the off-diagonal terms vanish, as well, and this means that relaxation is always accompanied by dephasing. On the other hand, dephasing can occur independently of relaxation. It can be shown that $T_2 \leq 2\,T_1$, making $T_2$ the more restrictive time for qubit coherence. The equality holds if relaxation induced dephasing is the only contribution to $1/T_2$, [Chirolli (2008), Levitt].

## 1.2. Spin qubits

For real applications, qubits need to be represented by physical systems with at least two levels, to which the values 0 and 1 can be assigned. A great many proposals for physical implementations have been made from pretty much all disciplines of physics [DiVincenzo (1999)]. These proposals include internal states of ions in a trap [Cirac (1995)], atoms in optical lattices [Brennen (1999), Jaksch (1999)], nuclear magnetic resonance of small molecules in solution [Chuang (1998)] and superconducting electrons in a Josephson Junction [Devoret (2004)], to name just a few.

Loss and DiVincenzo have proposed a solid state implementation using the electron spin states in coupled QD [Loss (1998)]. This can be called a *spintronics* implementation in that it is envisioned to exploit as many techniques of standard electronics as possible but with spin replacing the electron charge as the relevant physical quantity. With a view to the DiVincenzo criteria, we shortly comment on the perspective of this proposal[5]. Due to

[4]This is particularly the case for Zeeman-split spin qubits, which we focus on (see section 1.2).

[5]For a more elaborate disquisition, we refer the reader to the original articles, [Loss (1998), DiVincenzo (1999)].

the applications in classical computing there is an unmatched experience in the fabrication of solid state devices. Extrapolating to quantum systems, it is natural to assume that a solid state implementation could be scaled up to a full-scale quantum computer (criterion 1). At sufficiently low temperatures, the spin memory can easily be initialized by applying a strong magnetic field (criterion 2). Another advantage is the expectedly long coherence times and control over them via design parameters (criterion 3). This is the topic we deal with in this diploma thesis. Logic gates can be realized by controlling magnetic fields and the overlap of distinct QD electrons (criterion 4). The result of a spin-based computation could be read out by converting the spin to a charge degree of freedom, which can be measured conveniently (criterion 5).

Electron spin is a two level system with states $|\uparrow\rangle$ and $|\downarrow\rangle$, which are Zeeman-split in the presence of a magnetic field, $E_\uparrow - E_\downarrow = g\mu_B B$. It is natural to assign these states the values $|0\rangle$ and $|1\rangle$, respectively (or the other way round), such that one electron spin represents one qubit. On the other hand, two electron spins form singlet or triplet states which can also be interpreted as $|0\rangle$ or $|1\rangle$. Thereby, two electrons represent one qubit. Here, we focus on the former, more intuitive notion of spin qubits. Due to the Zeeman splitting, decoherence of such spin qubits is related to spin relaxation, as explained in section 1.1. Additionally, the nuclear spins of the solid state sample interact with the spin and randomize its phase. The effects of these two processes are depicted in figures 1.1 (b) and (c), respectively.

## 1.3. Spin qubits in graphene

To maintain control over the electron in a QD it is highly desirable, although not compelling, that the dot be made of semiconducting material. Indeed, GaAs QD are probably the most successful and most studied system [Hanson (2007)]. Before we explain what motivates us to examine QD in graphene, we give a few remarks on graphene, a fascinating material of its own.

Graphene is a flat, monatomic sheet of carbon. The carbon atoms in graphene are $sp_2$-hybridized and form a hexagonal lattice as depicted in figures 1.2 and 2.1. The name originates from *graph*ite and -*ene*, the suffix used in organic chemistry to describe the −C=C− character of atomic bonds. Due to its atomic structure, graphene (2D allotrope of $sp_2$ hybridized carbon) stands in line with fullerenes (0D), carbon nanotubes (1D) and graphite (3D). In fact, graphite consists of many graphene sheets stacked on one another and the most common means to produce graphene is to peel such a sheet off graphite [Geim (2007), Castro Neto (2009)].

Graphene, also called two-dimensional graphite, has been under theoretical study since more than sixty years ago [Wallace (1947)]. According to the Mermin-Wagner theorem, however, there can be no crystalline order in two dimensions, thus dooming the physical existence of two-dimensional graphite from a theoretical point of view [Mermin (1966), Mermin (1968)]. Although this theorem holds for isolated graphene, there is a way out by embedding it into a three-dimensional, stabilizing structure. Suspended graphene, graphene in solution and graphene on a substrate are stable materials that feature elec-

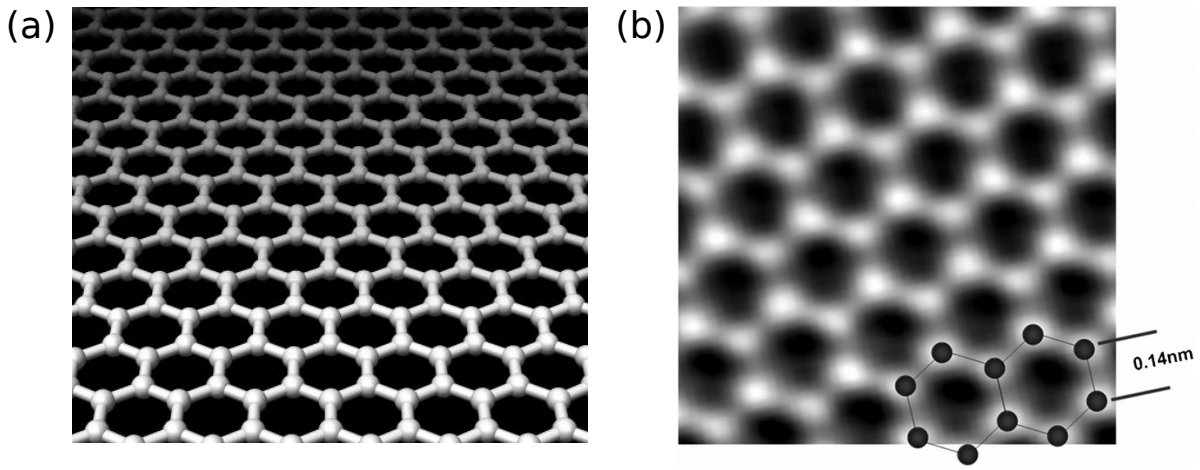


Figure 1.2.: Graphene is a two-dimensional monolayer of $sp_2$-hybridized carbon atoms. The atoms are separated by 1.42 Å and arranged in benzene rings, forming a hexagonal structure. Figure (a) shows a computer model of the atomic honeycomb lattice [Szkopek (2008)] and figure (b) is a transmission electron microscope image of graphene with indication of the atomic structure [Dato (2009)].

tronic properties of freestanding graphene and there is promising progress in the effort to fully restore freestanding properties [Geim (2007-2), Varykhalov (2008)].

Graphene is a promising material with many possible applications. In particular, its excellent conductance and its response to external electric fields have triggered progress in the production of next-generation ballistic field effect transistors [Lin (2008), Wei (2010)]. Also, the surface-to-mass ratio, unchallenged among conducting materials, suggests it as a main component of supercapacitors [Stoller (2008), Wu (2010)].

The low atomic weight of carbon leads to a small spin-orbit coupling and therefore long spin coherence times[6]. Natural carbon consists of 99% $^{12}$C and 1% $^{13}$C with nuclear spins 0 and 1/2, respectively[7]. The low nuclear spin in carbon relates to weak decoherence effects that can be even further suppressed by removing the $^{13}$C atoms (e.g. purification techniques or preselection of samples). This makes carbon based materials interesting for solid state spin qubit implementations. Indeed, a lot of research focuses on spin coherence in carbon nanotubes, diamond vacancies and graphene [Struck (2010), Steele (2009), Gaebel (2006)].

Due to the Klein paradox the quasirelativistic electronic behavior in graphene makes it hard to confine particles [Katsnelson (2006)]. A semiconducting spectrum is required to allow for the confinement of electrons in QD via tunable electrostatic barriers. Among other approaches to obtain gapped graphene, armchair GNR lead to a semiconducting spectrum with a typical gap of $\sim 40\,\mathrm{meV}$ for a ribbon width of $\sim 30\,\mathrm{nm}$. This specific

[6]This implication will become clear as we proceed, particularly in chapter 7. Strictly speaking, the origin of intrinsic spin-orbit coupling is the nuclear charge and not the nuclear/atomic weight, see (3.3). Of course, these quantities are closely related.

[7]The radioactive isotope $^{14}$C, famous for radiocarbon dating of archaeological samples, is completely irrelevant for our considerations. It has zero nuclear spin and a natural abundance of only $10^{-12}$.

system is particularly interesting because Klein tunneling allows for long-range coupling of distant QD by detuning of intermediate dots [Trauzettel (2007)]. In short, the dot electrons can couple not only via conduction state tunneling but also via valence state tunneling. This is a great asset as it enables direct logic operations between distant QD and since it increases the threshold for fault-tolerant quantum computing [Svore (2005)].

These features motivate us to study coherence times of spin qubits in armchair GNR. As nuclear spin effects are of minor significance in this system we assume $T_2 \approx 2\,T_1$ which makes the relaxation time a good overall measure for qubit coherence. That is why we focus on spin relaxation, in particular on the admixture mechanism (section 7.1) proposed by Khaetskii & Nazarov [Khaetskii (2001)].

## 1.4. Outline

Using a tight-binding ansatz, we review the electronic properties of graphene in chapter 2. From a generalized tight-binding calculation, that employs all orbitals of the second atomic shell, the energy level diagram of $sp_2$-hybridized carbon and the spin-orbit hamiltonian for the conducting $p_z$-orbitals is inferred (chapter 3). In chapter 4, we show how armchair edges lead to gapped spectrum in armchair GNR and describe electrostatically confined electrons.

The following chapters are a demonstration of our recent work. Assuming a continuum model, we derive the classical vibrational properties of a graphene ribbon. For acoustical modes at the center of the Brillouin zone the dispersion and explicit displacements are obtained (chapter 5). After introducing a field theory for ribbon phonons we turn to electron-phonon coupling and express the deformation potential in terms of in-plane phonon modes in chapter 6. Having prepared all its components we turn to the admixture mechanism and the calculation of a relaxation rate via Fermi's Golden Rule in chapter 7. Finally, we summarize our results and indicate the next steps in chapter 8.

Appendices A and B provide supplementary information on the continuum model and partial differential equations (PDE).

# 2. Tight-binding model

In this chapter, we derive the electronic properties that make graphene such an outstanding material. By and large we follow [Castro Neto (2009)] with deviations in explicit calculations that arise from a lattice orientation consistent with [Trauzettel (2007)].

Graphene is a two-dimensional hexagonal lattice with two carbon atoms per unit cell, separated by $a = 1.42\,\text{Å}$. These two equivalent sublattices are referred to as $A$ and $B$, figure 2.1.

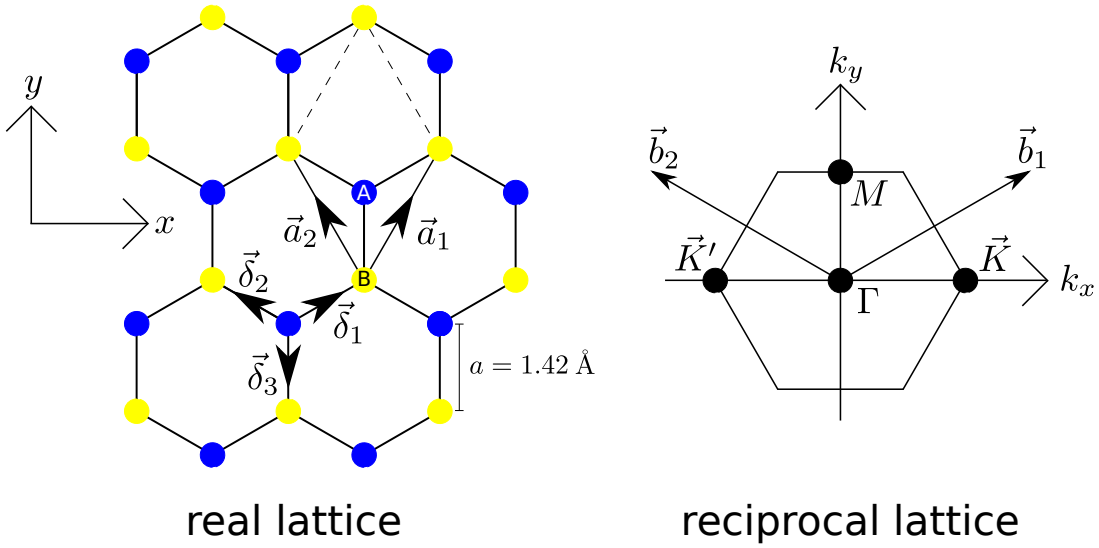


Figure 2.1.: Graphene is a hexagonal structure with two sublattices $A$ and $B$. We choose an orientation that conforms a GNR with armchair edges along the $y$-direction. Electron-hole degeneracy occurs at the $K$ and $K'$ points in reciprocal lattice. Each corner of the Brillouin zone corresponds to one of these *Dirac points*.

The two lattice vectors are

$$\vec{a}_1 = \frac{\sqrt{3}a}{2}(1, \sqrt{3})\,, \quad \vec{a}_2 = \frac{\sqrt{3}a}{2}(-1, \sqrt{3})$$

and the reciprocal lattice vectors are

$$\vec{b}_1 = \frac{2\pi}{3a}(\sqrt{3}, 1)\,, \quad \vec{b}_2 = \frac{2\pi}{3a}(-\sqrt{3}, 1)$$

such that $\vec{a}_i \cdot \vec{b}_j = 2\pi\delta_{ij}$ is satisfied. The three nearest neighbors are

$$\vec{\delta}_1 = \frac{a}{2}(\sqrt{3}, 1)\,, \quad \vec{\delta}_2 = \frac{a}{2}(-\sqrt{3}, 1)\,, \quad \vec{\delta}_3 = (0, -a) \tag{2.1}$$

for an atom of the $A$ sublattice and $-\delta_j$ for an atom of the $B$ sublattice. The six second-nearest neighbors are

$$\vec{a}_1\,, \quad \vec{a}_2\,, \quad \vec{a}_3 = \vec{a}_2 - \vec{a}_1\,, \quad \vec{a}_4 = -\vec{a}_1\,, \quad \vec{a}_5 = -\vec{a}_2\,, \quad \vec{a}_6 = -\vec{a}_3$$

for both sublattices and as $K$ and $K'$ points we choose

$$\vec{K} = \frac{4\pi}{3\sqrt{3}a}(1,0)\,, \quad \vec{K}' = \frac{4\pi}{3\sqrt{3}a}(-1,0)\,. \tag{2.2}$$

## 2.1. Energy spectrum

We consider a tight-binding hamiltonian with nearest and second-nearest neighbor hopping,

$$\begin{aligned} H &= \sum_i H_i\,, \\ H_i &= -t\sum_{j=1}^{3}\left(a_i^\dagger b_{ij} + b_i^\dagger a_{ij}\right) - t'\sum_{l=1}^{6}\left(a_i^\dagger a_{il} + b_i^\dagger b_{il}\right)\,, \end{aligned} \tag{2.3}$$

where $H_i$ is the contribution of unit cell $i$ and cannot be considered a hamiltonian of its own due to lack of hermiticity. Nearest neighbors of atoms in unit cell $i$ are labelled with indices $ij$ and their coupling constant is $t$. Accordingly, we use $il$ and $t'$ for second-nearest neighbors. While only hopping *to* the atoms of unit cell $i$ is considered in $H_i$, hopping *from* these atoms is restored via the summation over all unit cells for the total hamiltonian. The Fourier representations of the fields $a_i$ and $b_i$ are

$$a_i = \frac{1}{\sqrt{N}}\sum_{\vec{k}} e^{-i\vec{k}\cdot\vec{R}_i} a(\vec{k})\,, \quad b_i = \frac{1}{\sqrt{N}}\sum_{\vec{k}} e^{-i\vec{k}\cdot\vec{R}_i} b(\vec{k})\,, \tag{2.4}$$

where $N$ is the number of unit cells and $\vec{k} = (k_x, k_y)$ is a vector in momentum space. We substitute these representations in momentum space:

$$\begin{aligned} H_i &= -\frac{t}{N}\sum_{\vec{k},\vec{k}'} a^\dagger(\vec{k})\left(e^{i\vec{k}\cdot\vec{R}_i - i\vec{k}'\cdot(\vec{R}_i+\vec{\delta}_1)} + e^{i\vec{k}\cdot\vec{R}_i - i\vec{k}'\cdot(\vec{R}_i+\vec{\delta}_2)} + e^{i\vec{k}\cdot\vec{R}_i - i\vec{k}'\cdot(\vec{R}_i+\vec{\delta}_3)}\right) b(\vec{k}') \\ &\quad + b^\dagger(\vec{k})\left(e^{i\vec{k}\cdot\vec{R}_i - i\vec{k}'\cdot(\vec{R}_i-\vec{\delta}_1)} + e^{i\vec{k}\cdot\vec{R}_i - i\vec{k}'\cdot(\vec{R}_i-\vec{\delta}_2)} + e^{i\vec{k}\cdot\vec{R}_i - i\vec{k}'\cdot(\vec{R}_i-\vec{\delta}_3)}\right) a(\vec{k}') \\ &\quad - \frac{t'}{N}\sum_{\vec{k},\vec{k}'} a^\dagger(\vec{k})\left(e^{i\vec{k}\cdot\vec{R}_i - i\vec{k}'\cdot(\vec{R}_i+\vec{a}_1)} + e^{i\vec{k}\cdot\vec{R}_i - i\vec{k}'\cdot(\vec{R}_i+\vec{a}_2)} + e^{i\vec{k}\cdot\vec{R}_i - i\vec{k}'\cdot(\vec{R}_i+\vec{a}_3)}\right. \\ &\qquad \left. + e^{i\vec{k}\cdot\vec{R}_i - i\vec{k}'\cdot(\vec{R}_i+\vec{a}_4)} + e^{i\vec{k}\cdot\vec{R}_i - i\vec{k}'\cdot(\vec{R}_i+\vec{a}_5)} + e^{i\vec{k}\cdot\vec{R}_i - i\vec{k}'\cdot(\vec{R}_i+\vec{a}_6)}\right) a(\vec{k}') \\ &\quad + b^\dagger(\vec{k})\left(e^{i\vec{k}\cdot\vec{R}_i - i\vec{k}'\cdot(\vec{R}_i+\vec{a}_1)} + e^{i\vec{k}\cdot\vec{R}_i - i\vec{k}'\cdot(\vec{R}_i+\vec{a}_2)} + e^{i\vec{k}\cdot\vec{R}_i - i\vec{k}'\cdot(\vec{R}_i+\vec{a}_3)}\right. \\ &\qquad \left. + e^{i\vec{k}\cdot\vec{R}_i - i\vec{k}'\cdot(\vec{R}_i+\vec{a}_4)} + e^{i\vec{k}\cdot\vec{R}_i - i\vec{k}'\cdot(\vec{R}_i+\vec{a}_5)} + e^{i\vec{k}\cdot\vec{R}_i - i\vec{k}'\cdot(\vec{R}_i+\vec{a}_6)}\right) b(\vec{k}')\,. \end{aligned}$$

We can exclude the factor $e^{i\vec{R}_i\cdot(\vec{k}-\vec{k}')}/N$ from each term[1] and note and with the orthonormality relation

$$\delta_{\vec{k},\vec{k}'} = \frac{1}{N}\sum_{\vec{R}_i} e^{i\vec{R}_i\cdot(\vec{k}-\vec{k}')}$$

we find

$$\begin{aligned}
H &= \sum_i H_i \\
&= -t\sum_{\vec{k}} a^\dagger(\vec{k}) \underbrace{\left(e^{-i\vec{k}\cdot\vec{\delta}_1}+e^{-i\vec{k}\cdot\vec{\delta}_2}+e^{-i\vec{k}\cdot\vec{\delta}_3}\right)}_{=:H_{ab}(\vec{k})} b(\vec{k}) \\
&\quad +b^\dagger(\vec{k}) \underbrace{\left(e^{i\vec{k}\cdot\vec{\delta}_1}+e^{i\vec{k}\cdot\vec{\delta}_2}+e^{i\vec{k}\cdot\vec{\delta}_3}\right)}_{=:H_{ba}(\vec{k})} a(\vec{k}) \\
&\quad -t'\sum_{\vec{k}} a^\dagger(\vec{k}) \underbrace{\left(e^{-i\vec{k}\cdot\vec{a}_1}+e^{-i\vec{k}\cdot\vec{a}_2}+e^{-i\vec{k}\cdot\vec{a}_3}+e^{-i\vec{k}\cdot\vec{a}_4}+e^{-i\vec{k}\cdot\vec{a}_5}+e^{-i\vec{k}\cdot\vec{a}_6}\right)}_{=:H_{aa}(\vec{k})} a(\vec{k}) \\
&\quad +b^\dagger(\vec{k}) \underbrace{\left(e^{-i\vec{k}\cdot\vec{a}_1}+e^{-i\vec{k}\cdot\vec{a}_2}+e^{-i\vec{k}\cdot\vec{a}_3}+e^{-i\vec{k}\cdot\vec{a}_4}+e^{-i\vec{k}\cdot\vec{a}_5}+e^{-i\vec{k}\cdot\vec{a}_6}\right)}_{=:H_{bb}(\vec{k})} b(\vec{k})
\end{aligned}$$

which can be written as

$$H = \sum_{\vec{k}} \left(a^\dagger(\vec{k}), b^\dagger(\vec{k})\right) \underbrace{\begin{pmatrix} -t'H_{aa}(\vec{k}) & -tH_{ab}(\vec{k}) \\ -tH_{ba}(\vec{k}) & -t'H_{bb}(\vec{k}) \end{pmatrix}}_{=:E(\vec{k})} \begin{pmatrix} a(\vec{k}) \\ b(\vec{k}) \end{pmatrix} .$$

With MATHEMATICA we diagonalize $E(\vec{k})$ and simplify its eigenvalues to

$$E_\pm(\vec{k}) = \pm t\sqrt{3+f(\vec{k})} + t' f(\vec{k}) ,$$

where

$$f(\vec{k}) = 2\cos(\sqrt{3}k_x a) + 4\cos\left(\frac{\sqrt{3}}{2}k_x a\right)\cos\left(\frac{3}{2}k_y a\right) .$$

These eigenvalues correspond to the conduction band (+) and valence band (−). A plot of $E_\pm(\vec{k})$ is shown in figure 2.2.

At the corners of the Brillouin zone (Dirac points $K$ and $K'$) we find $E_+(\vec{k}) = E_-(\vec{k})$ which suggests a taylor expansion around $\vec{K}$. For $\vec{k} = \vec{K} + \vec{q}$ with $|\vec{q}| \ll |\vec{K}|$, we find up

[1] For total strictness we ought to use $\vec{R}_i^{(A)} = \vec{R}_i$ for the $A$ atom and $\vec{R}_i^{(B)} = \vec{R}_i + \vec{\delta}_3$ for the $B$ atom in unit cell $i$. One easily checks that this disambiguation does not change the calculation and we omit it for readability.

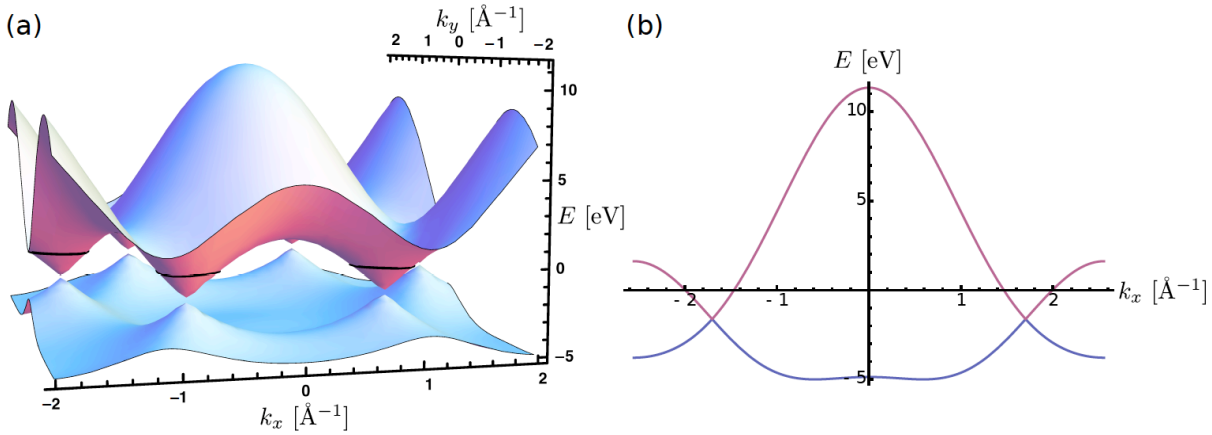


Figure 2.2.: Graph (a) is to be compared with the reciprocal lattice in figure 2.1. At the Dirac points the energy spectrum is degenerate and behaves linear. We choose $t = 2.7\,\mathrm{eV}$, $t' = 0.2t$ and the black horizontal indicates zero energy. Indeed, energy degeneracy occurs at $E < 0$ for $t' > 0$, in agreement with (2.5). A periodic cut for $k_y = 0$ is shown in (b).

to second order in $|\vec{q}|$

$$\begin{aligned} E_\pm(\vec{k}) &\approx \pm t \underbrace{\sqrt{\frac{9a^2|\vec{q}|^2}{4} - \frac{27a^4|\vec{q}|^4}{64} + \frac{9a^3(q_x^3 - 3q_x q_y^2)}{8}}}_{\approx \frac{3a|\vec{q}|}{2} + \frac{1}{2\frac{3a|\vec{q}|}{2}}\left(-\frac{27a^4|\vec{q}|^4}{64} + \frac{9a^3(q_x^3-3q_xq_y^2)}{8}\right)} + t'\left(-3 + \frac{9a^2|\vec{q}|^2}{4}\right) \\ &\approx \pm \underbrace{\frac{3at}{2}}_{=:\hbar v_F}|\vec{q}| \pm t\left(\underbrace{-\frac{9}{64}a^3|\vec{q}|^3}_{\mathcal{O}(|\vec{q}|^3)\approx 0} + \frac{3}{8}a^2|\vec{q}|^2 \underbrace{\frac{q_x^3 - 3q_xq_y^2}{|\vec{q}|^3}}_{=-\sin(3\alpha_{\vec{q}})}\right) + t'\left(-3 + \frac{9a^2|\vec{q}|^2}{4}\right) \\ &\approx -3t' \pm \hbar v_F|\vec{q}| + \left(\frac{9t'a^2}{4} \mp \frac{3ta^2}{8}\sin(3\alpha_{\vec{q}})\right)|\vec{q}|^2\,. \end{aligned} \tag{2.5}$$

With $\alpha_{\vec{q}} := \arcsin\frac{q_x}{|\vec{q}|}$ (see figure 2.3 (a)) we confirm

$$-\sin(3\alpha_{\vec{q}}) = 4\sin^3\alpha_{\vec{q}} - 3\sin\alpha_{\vec{q}} = 4\left(\frac{q_x}{|\vec{q}|}\right)^3 - 3\frac{q_x}{|\vec{q}|}\frac{q_x^2+q_y^2}{|\vec{q}|^2} = \frac{q_x^3 - 3q_xq_y^2}{|\vec{q}|^3}\,.$$

The linear dispersion in the vicinity the $K$ points explains the terminology *Dirac points*. Here, the *Fermi velocity* $v_F = \frac{3ta}{2\hbar} = 8.8\times10^5\,\frac{\mathrm{m}}{\mathrm{s}} \approx 1\times10^6\,\frac{\mathrm{m}}{\mathrm{s}}$ (we choose $t = 2.7\,\mathrm{eV}$) takes the role of the speed of light for massless particles. In the next section, we derive the hamiltonian describing the quasi-relativistic electrons near the Dirac points.

## 2.2. Dirac hamiltonian

We are interested in a hamiltonian, that describes the quasi-relativistic electrons in the vicinity of the Dirac points. The momentum of such an electron must satisfy $\vec{k}_0 = \vec{K} + \vec{q}$

with $|\vec{q}| \ll |\vec{K}|$ or $\vec{k}_0 = \vec{K}' + \vec{q}'$ with $|\vec{q}'| \ll |\vec{K}'|$. The quantities $\vec{q}$ and $\vec{q}'$ can be understood as placeholders for momenta with respect to the Dirac points which will be substituted by operators at the end of our calculation. All Fourier components that deviate significantly from the Dirac points can be neglected such that the summations in (2.4) simplify to

$$\sum_{\vec{k}} \to \sum_{\substack{\vec{k} = (\vec{K} + \vec{q}) + \delta\vec{k} \\ |\delta\vec{k}| \ll |\vec{K}|}} + \sum_{\substack{\vec{k} = (\vec{K}' + \vec{q}') + \delta\vec{k}' \\ |\delta\vec{k}'| \ll |\vec{K}'|}}$$

and the summations on the r.h.s. do not overlap. We infer

$$\begin{aligned} a_i &\overset{(2.4)}{\approx} \frac{1}{\sqrt{N}} \sum_{|\delta\vec{k}| \ll |\vec{K}|} e^{-i((\vec{K}+\vec{q})+\delta\vec{k})\cdot\vec{R}_i} a((\vec{K}+\vec{q})+\delta\vec{k}) \\ &\quad + \frac{1}{\sqrt{N}} \sum_{|\delta\vec{k}'| \ll |\vec{K}'|} e^{-i((\vec{K}'+\vec{q}')+\delta\vec{k}')\cdot\vec{R}_i} a((\vec{K}'+\vec{q}')+\delta\vec{k}') \\ &\approx e^{-i(\vec{K}+\vec{q})\cdot\vec{R}_i} \underbrace{\frac{1}{\sqrt{N}} \sum_{|\delta\vec{k}| \ll |\vec{K}|} e^{-i\delta\vec{k}\cdot\vec{R}_i} a(\vec{K}+\delta\vec{k})}_{=:a_{1,i}} \\ &\quad + e^{-i(\vec{K}'+\vec{q}')\cdot\vec{R}_i} \underbrace{\frac{1}{\sqrt{N}} \sum_{|\delta\vec{k}'| \ll |\vec{K}'|} e^{-i\delta\vec{k}'\cdot\vec{R}_i} a(\vec{K}'+\delta\vec{k}')}_{=:a_{2,i}} . \end{aligned} \tag{2.6}$$

In the second step we have relied on $|\vec{q}| \ll |\vec{K}|$ and $|\vec{q}'| \ll |\vec{K}'|$. The fields $a_{1,i}$ and $a_{2,i}$ are defined in analogy to $a_i$ (2.4) and describe particles near the Dirac points. An analog calculation leads to $b_{1,i}$ and $b_{2,i}$ and we summarize

$$\begin{aligned} a_i &\approx e^{-i(\vec{K}+\vec{q})\cdot\vec{R}_i} a_{1,i} + e^{-i(\vec{K}'+\vec{q}')\cdot\vec{R}_i} a_{2,i} , \\ b_i &\approx e^{-i(\vec{K}+\vec{q})\cdot\vec{R}_i} b_{1,i} + e^{-i(\vec{K}'+\vec{q}')\cdot\vec{R}_i} b_{2,i} . \end{aligned}$$

We now impose $t' = 0$ and (2.3) becomes

$$H = -t \sum_{i,j} \left( a_i^\dagger b_{ij} + b_i^\dagger a_{ij} \right) . \tag{2.7}$$

Assuming momenta close to the Dirac points we infer

$$\begin{aligned} H &= -t \sum_{i,j} (e^{i(\vec{K}+\vec{q})\cdot\vec{R}_i} a_{1,i}^\dagger + e^{i(\vec{K}'+\vec{q}')\cdot\vec{R}_i} a_{2,i}^\dagger)(e^{-i(\vec{K}+\vec{q})\cdot(\vec{R}_i+\vec{\delta}_j)} b_{1,i} + e^{-i(\vec{K}'+\vec{q}')\cdot(\vec{R}_i+\vec{\delta}_j)} b_{2,i}) \\ &\quad + (e^{i(\vec{K}+\vec{q})\cdot\vec{R}_i} b_{1,i}^\dagger + e^{i(\vec{K}'+\vec{q}')\cdot\vec{R}_i} b_{2,i}^\dagger)(e^{-i(\vec{K}+\vec{q})\cdot(\vec{R}_i-\vec{\delta}_j)} a_{1,i} + e^{-i(\vec{K}'+\vec{q}')\cdot(\vec{R}_i-\vec{\delta}_j)} a_{2,i}) , \end{aligned}$$

where we have used $a_{1,ij} = a_{1,i}$ and likewise since these fields vary slowly over the unit cell such that translations $\vec{\delta}_j$ can be neglected, [Castro Neto (2009)]. Due to momentum conservation it is clear that an electron cannot hop from $K$ to $K'$, such that $a_{1,i}^\dagger b_{2,i} = 0$ and likewise (the summations in (2.6) do not overlap):

$$H = -t \sum_{i,j} a_{1,i}^\dagger e^{-i(\vec{K}+\vec{q})\cdot\vec{\delta}_j} b_{1,i} + a_{2,i}^\dagger e^{-i(\vec{K}'+\vec{q}')\cdot\vec{\delta}_j} b_{2,i} + b_{1,i}^\dagger e^{i(\vec{K}+\vec{q})\cdot\vec{\delta}_j} a_{1,i} + b_{2,i}^\dagger e^{i(\vec{K}'+\vec{q}')\cdot\vec{\delta}_j} a_{2,i} .$$

Since $|\vec{q}| \ll |\vec{K}|$ we expand $\sum_j e^{-i(\vec{K}+\vec{q})\cdot\vec{\delta}_j}$ about $\vec{K}$ and $\sum_j e^{-i(\vec{K}'+\vec{q}')\cdot\vec{\delta}_j}$ analog. With the explicit quantities (2.1) and (2.2) we find in first order

$$\begin{aligned}\sum_j e^{-i(\vec{K}+\vec{q})\cdot\vec{\delta}_j} &\approx \sum_j (1 - i\vec{\delta}_j\cdot\vec{q}) e^{-i\vec{K}\cdot\vec{\delta}_j} = -\frac{3a}{2}(q_x - iq_y)\,,\\ \sum_j e^{-i(\vec{K}'+\vec{q}')\cdot\vec{\delta}_j} &\approx \frac{3a}{2}(q_x + iq_y)\end{aligned}$$

and the hamiltonian further simplifies to

$$\begin{aligned}H &= -t\sum_i \begin{pmatrix} a_{1,i}^\dagger, b_{1,i}^\dagger\end{pmatrix}\begin{pmatrix} 0 & -\frac{3a}{2}(q_x - iq_y)\\ -\frac{3a}{2}(q_x + iq_y) & 0\end{pmatrix}\begin{pmatrix} a_{1,i}\\ b_{1,i}\end{pmatrix}\\ &\quad + \begin{pmatrix} a_{2,i}^\dagger, b_{2,i}^\dagger\end{pmatrix}\begin{pmatrix} 0 & \frac{3a}{2}(q_x + iq_y)\\ \frac{3a}{2}(q_x - iq_y) & 0\end{pmatrix}\begin{pmatrix} a_{2,i}\\ b_{2,i}\end{pmatrix}.\end{aligned}$$

In the next step we transform to a continuous field:

$$\begin{aligned}\sum_i &\to \int \mathrm{d}x\,\mathrm{d}y\,,\\ \begin{pmatrix} a_{1,i}\\ b_{1,i}\end{pmatrix} &\to \begin{pmatrix} a_1(\vec{r})\\ b_1(\vec{r})\end{pmatrix} =: \Psi_1(\vec{r})\,,\\ \vec{q}, \vec{q'} &\to \frac{\vec{\nabla}}{i}\,.\end{aligned}$$

We remember that $\vec{q}$, $\vec{q'}$ are the momenta with respect to the Dirac points such that the last assignment is indeed correct as $\Psi_{1,2}(\vec{r})$ describe particles with momenta close to these points. The hamiltonian becomes

$$\begin{aligned}H &= -\frac{3ta}{2}\int \mathrm{d}x\,\mathrm{d}y\,\Psi_1^\dagger(\vec{r})\begin{pmatrix} 0 & i\partial_x + \partial_y\\ i\partial_x - \partial_y & 0\end{pmatrix}\Psi_1(\vec{r})\\ &\qquad + \Psi_2^\dagger(\vec{r})\begin{pmatrix} 0 & -i\partial_x + \partial_y\\ -i\partial_x - \partial_y & 0\end{pmatrix}\Psi_2(\vec{r})\\ &= -i\frac{3ta}{2}\int \mathrm{d}x\,\mathrm{d}y\,\Psi_1^\dagger(\vec{r})\left(\begin{pmatrix} 0 & 1\\ 1 & 0\end{pmatrix}\partial_x + \begin{pmatrix} 0 & -i\\ i & 0\end{pmatrix}\partial_y\right)\Psi_1(\vec{r})\\ &\qquad + \Psi_2^\dagger(\vec{r})\left(\begin{pmatrix} 0 & -1\\ -1 & 0\end{pmatrix}\partial_x + \begin{pmatrix} 0 & -i\\ i & 0\end{pmatrix}\partial_y\right)\Psi_2(\vec{r})\\ &= -i\hbar v_F\int \mathrm{d}x\,\mathrm{d}y\,\Big(\underbrace{\Psi_1^\dagger(\vec{r})\vec{\sigma}\cdot\vec{\nabla}\Psi_1(\vec{r})}_{\vec{K}} + \underbrace{\Psi_2^\dagger(\vec{r})\vec{\sigma}^*\cdot\vec{\nabla}\Psi_2(\vec{r})}_{\vec{K}'}\Big)\,,\end{aligned} \tag{2.8}$$

where we have used $\vec{\sigma} := (\sigma_x, \sigma_y)$ and $\vec{\sigma}^* := (-\sigma_x, \sigma_y)$ with the standard representation of Pauli matrices. Due to our orientation of the graphene lattice this result agrees with the hamiltonian used in [Trauzettel (2007)].

## 2.3. Pseudo-spin and Klein paradox

If we go back from second quantization to first quantization the hamiltonian (2.8) becomes

$$\begin{aligned} -i\hbar v_F \vec{\sigma}\cdot\vec{\nabla}\psi_1(\vec{r}) &= E\psi_1(\vec{r}) \quad \text{at the } K \text{ point}, \\ -i\hbar v_F \vec{\sigma}^*\cdot\vec{\nabla}\psi_2(\vec{r}) &= E\psi_2(\vec{r}) \quad \text{at the } K' \text{ point}. \end{aligned} \tag{2.9}$$

The eigenstates in momentum space are

$$\begin{aligned} \psi_{1,\pm}(\vec{q}) &= \frac{1}{\sqrt{2}}\begin{pmatrix} e^{-i\vartheta_{\vec{q}}/2} \\ \pm e^{i\vartheta_{\vec{q}}/2}\end{pmatrix}, \\ \psi_{2,\pm}(\vec{q}) &= \frac{1}{\sqrt{2}}\begin{pmatrix} e^{i\vartheta_{\vec{q}}/2} \\ \mp e^{-i\vartheta_{\vec{q}}/2}\end{pmatrix}, \end{aligned} \tag{2.10}$$

where we have used $\vartheta_{\vec{q}} := \arcsin\frac{q_y}{|\vec{q}|}$ (see figure 2.3 (a)). Indeed we verify

$$\begin{aligned} H_K\psi_{1,\pm}(\vec{q}) &= \hbar v_F \vec{\sigma}\cdot\vec{q}\frac{1}{\sqrt{2}}\begin{pmatrix} e^{-i\vartheta_{\vec{q}}/2} \\ \pm e^{i\vartheta_{\vec{q}}/2}\end{pmatrix} \\ &= \hbar v_F\left(|\vec{q}|\cos\vartheta_{\vec{q}}\begin{pmatrix}0&1\\1&0\end{pmatrix} + |\vec{q}|\sin\vartheta_{\vec{q}}\begin{pmatrix}0&-i\\i&0\end{pmatrix}\right)\frac{1}{\sqrt{2}}\begin{pmatrix} e^{-i\vartheta_{\vec{q}}/2} \\ \pm e^{i\vartheta_{\vec{q}}/2}\end{pmatrix} \\ &= \frac{\hbar v_F|\vec{q}|}{\sqrt{2}}\left(\frac{e^{i\vartheta_{\vec{q}}}+e^{-i\vartheta_{\vec{q}}}}{2}\begin{pmatrix}\pm e^{i\vartheta_{\vec{q}}/2}\\ e^{-i\vartheta_{\vec{q}}/2}\end{pmatrix} + \frac{e^{i\vartheta_{\vec{q}}}-e^{-i\vartheta_{\vec{q}}}}{2i}\begin{pmatrix}\mp ie^{i\vartheta_{\vec{q}}/2}\\ ie^{-i\vartheta_{\vec{q}}/2}\end{pmatrix}\right) \\ &= \frac{\hbar v_F|\vec{q}|}{\sqrt{2}}\begin{pmatrix}\pm(e^{i\vartheta_{\vec{q}}/2})e^{-i\vartheta_{\vec{q}}}\\ (e^{-i\vartheta_{\vec{q}}/2})e^{i\vartheta_{\vec{q}}}\end{pmatrix} = \pm\hbar v_F|\vec{q}|\frac{1}{\sqrt{2}}\begin{pmatrix} e^{-i\vartheta_{\vec{q}}/2} \\ \pm e^{i\vartheta_{\vec{q}}/2}\end{pmatrix} \\ &= \pm\hbar v_F|\vec{q}|\psi_{1,\pm}(\vec{q})\,. \quad \checkmark \end{aligned}$$

The *helicity* operator

$$h = \frac{\vec{\sigma}\cdot\vec{q}}{2|\vec{q}|}$$

has the same form as $H_K$, yet with a prefactor $\frac{1}{2|\vec{q}|}$ instead of $\hbar v_F$. Therefore it is obvious that its eigenstates are $\psi_{1,\pm}(\vec{q})$:

$$h\psi_{1,\pm}(\vec{q}) = \pm\frac{1}{2}\psi_{1,\pm}(\vec{q})\,. \tag{2.11}$$

With $\psi_{2,\pm}(\vec{q})$ and $\vec{\sigma}^*$ we obtain equivalent results for $H_{K'}$ and its according helicity operator $h'$ such that electrons ($\psi_{1/2,+}(\vec{q})$) have positive helicity and holes ($\psi_{1/2,-}(\vec{q})$) have negative helicity.

We emphasize that the spin operators $\vec{\sigma}$ and $\vec{\sigma}^*$ do not act on real spin but on the two components of the wave function, which correspond to the $A$ and $B$ sublattices, and is therefore referred to as *pseudo-spin*. Pseudo-spin is related to the lattice site. Equations (2.8) and (2.11) do not hold for arbitrary momenta such that only electrons near the Dirac points have well-defined helicity.

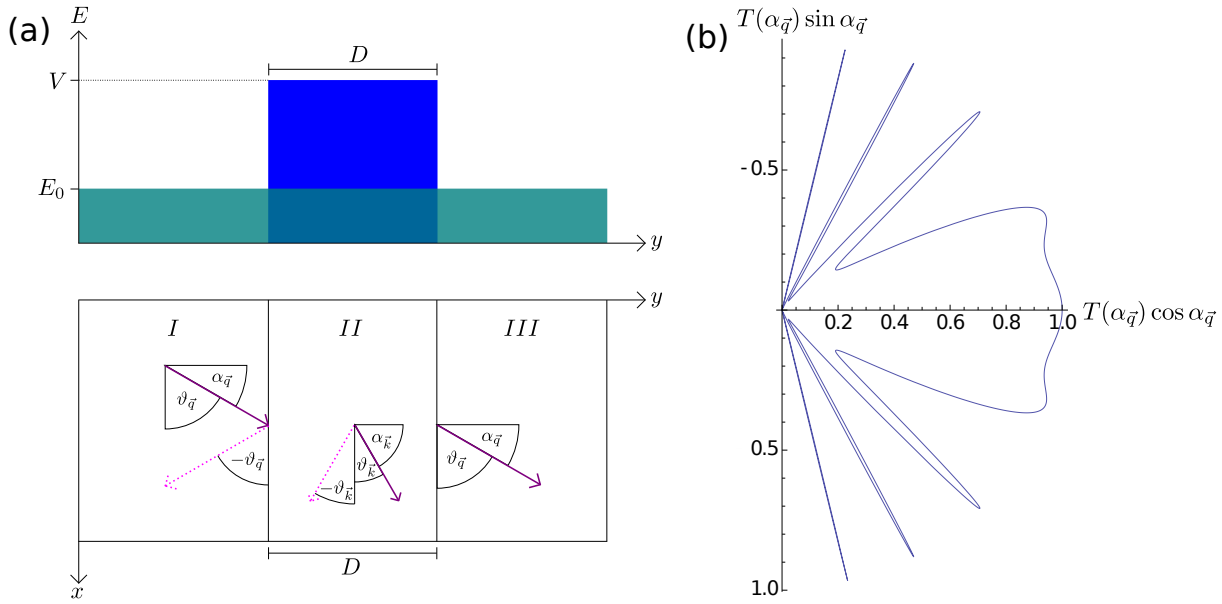


Figure 2.3.: The scattering setup is shown in (a). Top: Particle energy and potential barrier. Bottom: Angles that enter the wavefunction in regions $I$, $II$ and $III$. Figure (b) shows the tunneling probability as a function of the incident angle with parameters $E_0 = 80\,\text{meV}$, $V = 160\,\text{meV}$ and $D = 110\,\text{nm}$, see (2.12).

With a gauge transformation the wave equation (2.10) can be written as

$$\psi_{1,\pm}(\vec{q}) = \frac{1}{\sqrt{2}} \begin{pmatrix} 1 \\ \pm e^{i\vartheta_{\vec{q}}} \end{pmatrix} .$$

Figure 2.3 sketches a particle with energy $E_0$ that is scattered at a square potential barrier of height $V$ and width $D$, [Katsnelson (2006)]. In region $I$ the wave function is a superposition of incident and reflected waves,

$$\psi_1^{(I)}(\vec{r}) = \frac{1}{\sqrt{2}} \begin{pmatrix} 1 \\ s e^{i\vartheta_{\vec{q}}} \end{pmatrix} e^{i(q_x x + q_y y)} + \frac{r}{\sqrt{2}} \begin{pmatrix} 1 \\ s e^{-i\vartheta_{\vec{q}}} \end{pmatrix} e^{i(q_x x - q_y y)} ,$$

where $s := \text{sgn} E_0$. Accordingly, we have

$$\psi_1^{(II)}(\vec{r}) = \frac{a}{\sqrt{2}} \begin{pmatrix} 1 \\ s' e^{i\vartheta_{\vec{k}}} \end{pmatrix} e^{i(k_x x + k_y y)} + \frac{b}{\sqrt{2}} \begin{pmatrix} 1 \\ s' e^{-i\vartheta_{\vec{k}}} \end{pmatrix} e^{i(k_x x - k_y y)}$$

in region $II$, where $s' := \text{sgn}(E_0 - V)$, $k_x := q_x$ and $k_y := \sqrt{\left(\frac{E_0 - V}{v_F}\right)^2 - q_x^2}$. Only a transmitted wave occurs in region $III$:

$$\psi_1^{(III)}(\vec{r}) = \frac{t}{\sqrt{2}} \begin{pmatrix} 1 \\ s e^{i\vartheta_{\vec{q}}} \end{pmatrix} e^{i(q_x x + q_y y)} .$$

Since the Dirac hamiltonian is of first order the wave function must be continuous (not so its derivative as for classical second order hamiltonians). We use the continuity conditions

$$\begin{aligned} \psi_1^{(I)}(x,0) &\stackrel{!}{=} \psi_1^{(II)}(x,0) , \\ \psi_1^{(II)}(x,D) &\stackrel{!}{=} \psi_1^{(III)}(x,D) \end{aligned}$$

to resolve the coefficients $r, a, b, t$. With MATHEMATICA we find long but simple expressions that depend on $\vartheta_{\vec{q}}$ and $\vartheta_{\vec{k}}$. Due to the definition of $k_x$ and $k_y$ we have $\vartheta_{\vec{k}} = \vartheta_{\vec{k}}(\vartheta_{\vec{q}})$ and the transition probability is given by

$$\begin{aligned} T(\vartheta_{\vec{q}}) &= t(\vartheta_{\vec{q}})t^*(\vartheta_{\vec{q}}) \\ &= \frac{\sin^2\vartheta_{\vec{q}}\sin^2\vartheta_{\vec{k}}}{\cos^2(Dk_y)\sin^2\vartheta_{\vec{q}}\sin^2\vartheta_{\vec{k}} + \left(1 - ss'\cos\vartheta_{\vec{q}}\cos\vartheta_{\vec{k}}\right)^2\sin^2(Dk_y)} \,. \end{aligned}$$

It is common to express this quantity in terms of the angles $\alpha_{\vec{q}}$ and $\alpha_{\vec{k}}$, see figure 2.3. We use $\sin\vartheta_{\vec{q}} = \cos(\frac{\pi}{2} - \vartheta_{\vec{q}}) = \cos\alpha_{\vec{q}}$, $\cos\vartheta_{\vec{q}} = \sin(\frac{\pi}{2} - \vartheta_{\vec{q}}) = \sin\alpha_{\vec{q}}$ and likewise for $\vartheta_{\vec{k}}$ and $\alpha_{\vec{k}}$ to find

$$T(\alpha_{\vec{q}}) = \frac{\cos^2\alpha_{\vec{q}}\cos^2\alpha_{\vec{k}}}{\cos^2(Dk_y)\cos^2\alpha_{\vec{q}}\cos^2\alpha_{\vec{k}} + \left(1 - ss'\sin\alpha_{\vec{q}}\sin\alpha_{\vec{k}}\right)^2\sin^2(Dk_y)} \,. \tag{2.12}$$

We note $T(\alpha_{\vec{q}}) = T(-\alpha_{\vec{q}})$ and that the barrier becomes completely transparent ($T = 1$) for $Dk_y = n\pi$ with integer $n$. This phenomenon is called the Klein paradox. A plot of $T(\alpha_{\vec{q}})$ is shown in figure 2.3 (b). For $V \gg E_0$ it follows that $k_y \gg k_x$ and hence $\alpha_{\vec{k}} \approx 0$ such that $T(\alpha_{\vec{q}})$ simplifies to

$$\begin{aligned} T(\alpha_{\vec{q}}) &\approx \frac{\cos^2\alpha_{\vec{q}}}{\cos^2(Dk_y)\cos^2\alpha_{\vec{q}} + \sin^2(Dk_y) + (\cos^2(Dk_y)\sin^2\alpha_{\vec{q}} - \cos^2(Dk_y)\sin^2\alpha_{\vec{q}})} \\ &= \frac{\cos^2\alpha_{\vec{q}}}{\underbrace{\cos^2(Dk_y)\underbrace{(\cos^2\alpha_{\vec{q}} + \sin^2\alpha_{\vec{q}})}_{=1} + \sin^2(Dk_y) - \cos^2(Dk_y)\sin^2\alpha_{\vec{q}}}_{=1}} \\ &= \frac{\cos^2\alpha_{\vec{q}}}{1 - \cos^2(Dk_y)\sin^2\alpha_{\vec{q}}} \,. \end{aligned}$$

# 3. Spin-orbit interaction

The hamiltonian that couples the electron's spin to its orbital motion in graphene can be derived from symmetry arguments [Kane (2005)] or coupling of the $n = 2$ $s$ and $p$ orbitals. We follow the latter ansatz, yet with a different lattice orientation (see (2.1), (3.2) and [Min (2006)]). There has been a controversy concerning the coupling constants for intrinsic and extrinsic spin-orbit coupling. As pointed out by Gmitra *et al.* the $d$ orbitals cannot be neglected as they might bring the major contribution of 96% to the intrinsic coupling constant [Gmitra (2009)]. As they do not affect the derivation of the spin-orbit hamiltonian we can choose appropriate constants in the very end.

As a side effect of our calculations we find the $sp_2$-hybridization and the energy level diagram in this chapter.

## 3.1. Tight-binding with $s$ and $p$ orbitals

In (2.7) and subsequent steps, only the $p_z$ orbitals are considered. Here, we specify all $s$ and $p$ hoppings and also include on-site terms which are merely the $s$ and $p$ orbital energies. The resulting hamiltonian, $H_{sp}$, is

$$
\begin{aligned}
H_{sp} \;=\; & \sum_i (a^\dagger_{i,s}, a^\dagger_{i,p_x}, a^\dagger_{i,p_y}, a^\dagger_{i,p_z}) \\
& \times \left( \underbrace{\begin{pmatrix} t_s & 0 & 0 & 0 \\ 0 & t_p & 0 & 0 \\ 0 & 0 & t_p & 0 \\ 0 & 0 & 0 & t_p \end{pmatrix}}_{\text{on-site terms}} \begin{pmatrix} a_{i,s} \\ a_{i,p_x} \\ a_{i,p_y} \\ a_{i,p_z} \end{pmatrix} + \sum_j \underbrace{\overset{\overset{!}{\downarrow}}{\begin{pmatrix} t_{s,s} & t_{s,p_x} & t_{s,p_y} & t_{s,p_z} \\ t_{p_x,s} & t_{p_x,p_x} & t_{p_x,p_y} & t_{p_x,p_z} \\ t_{p_y,s} & t_{p_y,p_x} & t_{p_y,p_y} & t_{p_y,p_z} \\ t_{p_z,s} & t_{p_z,p_x} & t_{p_z,p_y} & t_{p_z,p_z} \end{pmatrix}}}_{\text{hopping terms between } \textit{all } s \text{ and } p \text{ orbitals}} \begin{pmatrix} b_{ij,s} \\ b_{ij,p_x} \\ b_{ij,p_y} \\ b_{ij,p_z} \end{pmatrix} \right) \\
& + \sum_i (b^\dagger_{i,s}, b^\dagger_{i,p_x}, b^\dagger_{i,p_y}, b^\dagger_{i,p_z}) \\
& \times \left( \underbrace{\begin{pmatrix} t_s & 0 & 0 & 0 \\ 0 & t_p & 0 & 0 \\ 0 & 0 & t_p & 0 \\ 0 & 0 & 0 & t_p \end{pmatrix}}_{=:H_{B,\mu;B,\nu}} \begin{pmatrix} b_{i,s} \\ b_{i,p_x} \\ b_{i,p_y} \\ b_{i,p_z} \end{pmatrix} + \sum_j \underbrace{\begin{pmatrix} t_{s,s} & t_{s,p_x} & t_{s,p_y} & t_{s,p_z} \\ t_{p_x,s} & t_{p_x,p_x} & t_{p_x,p_y} & t_{p_x,p_z} \\ t_{p_y,s} & t_{p_y,p_x} & t_{p_y,p_y} & t_{p_y,p_z} \\ t_{p_z,s} & t_{p_z,p_x} & t_{p_z,p_y} & t_{p_z,p_z} \end{pmatrix}}_{=:H_{B,\mu;A,\nu}} \begin{pmatrix} a_{ij,s} \\ a_{ij,p_x} \\ a_{ij,p_y} \\ a_{ij,p_z} \end{pmatrix} \right) .
\end{aligned}
\tag{3.1}
$$

All matrix elements $t_{\dots}$ are real and we simply label the on-site constants with $t_s = s$

and $t_p = p$, and choose the latter as zero energy. The hopping parameters also depend on the connecting vectors: $t_{\mu,\nu} = t_{\mu,\nu}(\vec{\delta}_j)$, where $\mu$, $\nu$ label the four orbitals. These *transfer integrals* are commonly labelled with two latin letters corresponding to the orbital quantum numbers and a third greek letter that denotes the angular momentum along the connecting axis, see figure 3.1 (a), [Sutton]. It is crucial to point out that the $s$ orbital is even with respect to reflections and the $p_i$ orbital is even under all reflections but $x_i$, where it is odd (see for example [Haken & Wolf]). This is why some coupling constants vanish.

In order to distinguish $p_x$, $p_y$ and $p_z$ orbitals one needs to define a coordinate system. This also allows us to find explicit expressions for $t_{\mu,\nu}(\vec{\delta}_j)$. Be $(n_x^{(j)}, n_y^{(j)})$ the unit vector pointing along $\vec{\delta}_j$. Figures 3.1 (b) and (c) explain how we obtain $t_{s,p_x}(\vec{\delta}_1) = n_x^{(1)}(sp\sigma)$. Similarly[1] we obtain the remaining coupling constants in table 3.1.

| | | | |
|---|---|---|---|
| $t_s$ | $= s$ | $t_{p_z,p_z}$ | $= (pp\pi)$ |
| $t_p$ | $= p$ | $t_{s,p_x}(\vec{\delta}_j)$ | $= n_x^{(j)}(sp\sigma)$ |
| $t_{s,s}$ | $= (ss\sigma)$ | $t_{s,p_y}(\vec{\delta}_j)$ | $= n_y^{(j)}(sp\sigma)$ |
| $t_{s,p_z}$ | $= 0$ | $t_{p_x,p_x}(\vec{\delta}_j)$ | $= (n_x^{(j)})^2(pp\sigma) + (n_y^{(j)})^2(pp\pi)$ |
| $t_{p_x,p_z}$ | $= 0$ | $t_{p_x,p_y}(\vec{\delta}_j)$ | $= n_x^{(j)} n_y^{(j)}\,((pp\sigma) - (pp\pi))$ |
| $t_{p_y,p_z}$ | $= 0$ | $t_{p_y,p_y}(\vec{\delta}_j)$ | $= (n_y^{(j)})^2(pp\sigma) + (n_x^{(j)})^2(pp\pi)$ |

Table 3.1.: The matrix elements for $s$ and $p$ orbital hopping along a certain direction specified by $\vec{\delta}_j$, [Min (2006)].

With exactly the same procedure that follows (2.7) the matrix elements of $H_{sp}$ act on separate fields at $K$ and $K'$. We include the summation over $j$ as well as the phases of said fields to write these matrix elements as[2]

$$\begin{aligned} H_{A,\mu;A,\nu}(\vec{k}) &= H_{B,\mu;B,\nu}(\vec{k}) = t_\mu \delta_{\mu,\nu}\,, \\ H_{A,\mu;B,\nu}(\vec{k}) &= H^*_{B,\mu;A,\nu}(\vec{k}) = \sum_{j=1}^{3} t_{\mu,\nu}(\vec{\delta}_j) e^{-i\vec{k}\cdot\vec{\delta}_j}\,, \end{aligned} \tag{3.2}$$

with $\vec{k} \in \{\vec{K}, \vec{K}'\}$. As an example, the matrix element highlighted by the exclamation mark in (3.1) becomes $H_{A,s;B;s} = \sum_j t_{s,s} e^{-i\vec{k}\cdot\vec{\delta}_j}$.

## 3.2. Eigenenergies and eigenstates

To specify the matrix elements of $H_{sp}$ at the Dirac points, (3.2), we define $\alpha := \frac{3}{2}(sp\sigma)$ and $\beta := \frac{3}{4}\left((pp\sigma) - (pp\pi)\right)$. With

$$\vec{n}^{(1)} = \frac{1}{2}(\sqrt{3}, 1)\,, \quad \vec{n}^{(2)} = \frac{1}{2}(-\sqrt{3}, 1)\,, \quad \vec{n}^{(3)} = (0, -1)$$

[1] Some of the transfer integrals vanish trivially due to the orbitals' behavior with respect to reflection. For $p$-$p$ transfer integrals the central orbital needs to be rotated, too. $p_y = \sin\theta p_{x'} + \cos\theta p_{y'}$, $p_z = p_{z'}$;

[2] Note that we do *not* sum over double indices in the next equation.

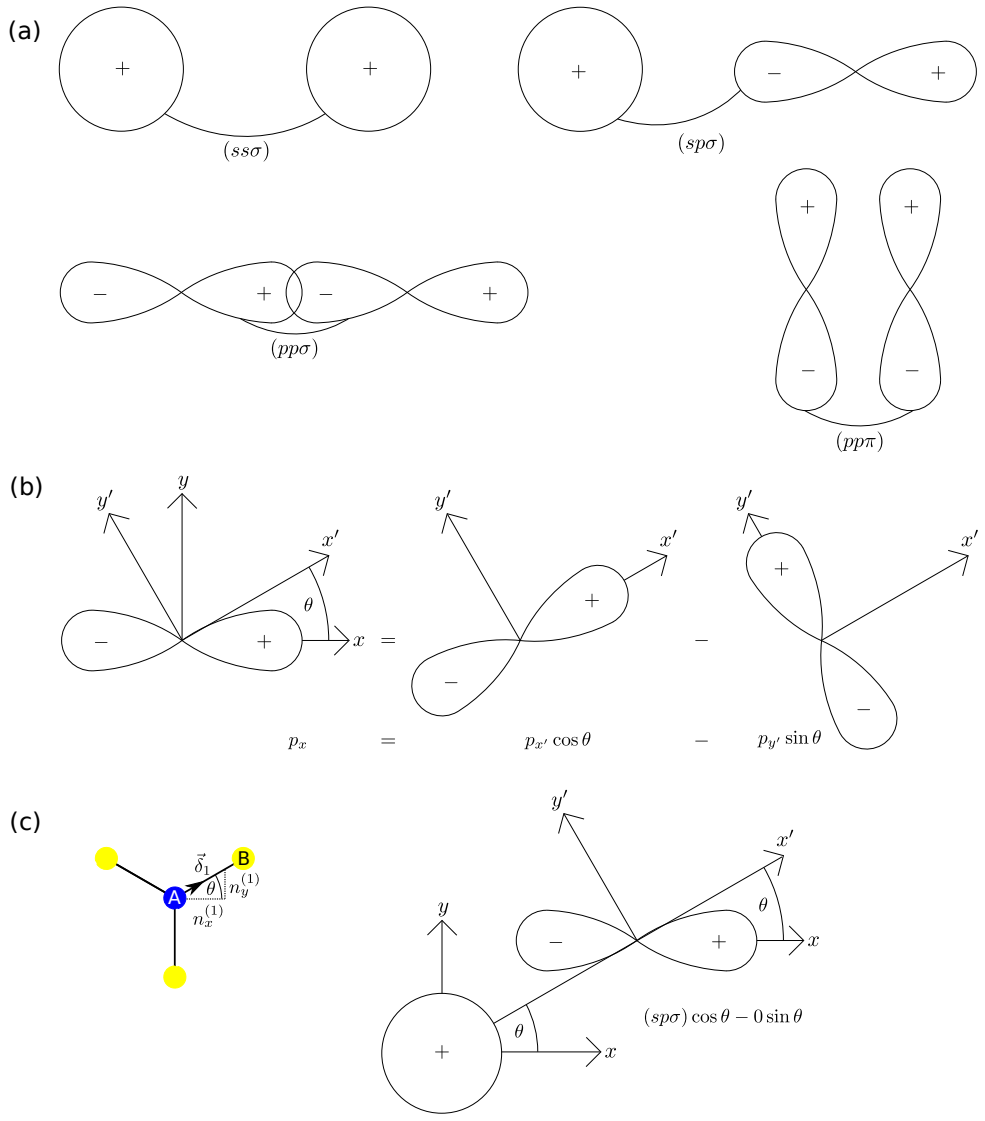


Figure 3.1.: (a): There are only four fundamental transfer integrals between $s$ and $p$ orbitals. Other integrals vanish for symmetry reasons. All of them have zero angular momentum along the connection axis $(ab\sigma)$ but the $(pp\pi)$ integral. The signs indicate the orbital's behavior under reflection. (b): After rotation about an angle $\theta$ the $p_x$ orbital can be expressed in terms of $p_{x'}$ and $p_{y'}$ orbitals in the rotated system. (c): By virtue of this rotation we can express the hopping to a neighboring orbital in terms of the fundamental transfer integrals shown in (a), [Sutton].

we find for example

$$\begin{aligned} H_{A,s;B,p_x}(\vec{K}) &= \sum_j t_{s,p_x}(\vec{\delta}_j)e^{-i\vec{K}\cdot\vec{\delta}_j} = (sp\sigma)\left(n_x^{(1)}e^{-i\frac{2\pi}{3}} + n_x^{(2)}e^{i\frac{2\pi}{3}} + n_x^{(3)}e^{0}\right) \\ &= (sp\sigma)\left(\frac{\sqrt{3}}{2}\left(-\frac{1}{2} - \frac{\sqrt{3}}{2}i\right) + \frac{-\sqrt{3}}{2}\left(-\frac{1}{2} + \frac{\sqrt{3}}{2}i\right) + 0\cdot 1\right) = \\ &= -\frac{3i}{2}(sp\sigma) = -i\alpha\,. \end{aligned}$$

The other matrix elements are found accordingly and the results are listed in table 3.2.

| Orbital | $A,s$ | $A,p_x$ | $A,p_y$ | $A,p_z$ | $B,s$ | $B,p_x$ | $B,p_y$ | $B,p_z$ |
|---|---|---|---|---|---|---|---|---|
| $A,s$ | $s$ | 0 | 0 | 0 | 0 | $\mp i\alpha$ | $-\alpha$ | 0 |
| $A,p_x$ | 0 | 0 | 0 | 0 | $\pm i\alpha$ | $-\beta$ | $\mp i\beta$ | 0 |
| $A,p_y$ | 0 | 0 | 0 | 0 | $\alpha$ | $\mp i\beta$ | $\beta$ | 0 |
| $A,p_z$ | 0 | 0 | 0 | 0 | 0 | 0 | 0 | 0 |
| $B,s$ | 0 | $\mp i\alpha$ | $\alpha$ | 0 | $s$ | 0 | 0 | 0 |
| $B,p_x$ | $\pm i\alpha$ | $-\beta$ | $\pm i\beta$ | 0 | 0 | 0 | 0 | 0 |
| $B,p_y$ | $-\alpha$ | $\pm i\beta$ | $\beta$ | 0 | 0 | 0 | 0 | 0 |
| $B,p_z$ | 0 | 0 | 0 | 0 | 0 | 0 | 0 | 0 |

Table 3.2.: Matrix elements of $H_{sp}$ near the Dirac points. The upper (lower) sign corresponds to $K$ ($K'$).

We do not derive the eigenenergies and eigenstates of the hamiltonian but only check the results we infer from [Min (2006)], which are listed in table 3.3. With $\gamma_\pm := \frac{\sqrt{s^2+8\alpha^2}\pm s}{2}$ we confirm for example $|\psi_1\rangle$:

$$H|\psi_1\rangle = \begin{pmatrix} -\gamma_- s + \alpha^2 + \alpha^2 \\ \mp i\alpha\beta \pm i\alpha\beta \\ \alpha\beta - \alpha\beta \\ 0 \\ 0 \\ \mp i\alpha\gamma_- \\ \alpha\gamma_- \\ 0 \end{pmatrix} = -\gamma_- \begin{pmatrix} -\gamma_- \\ 0 \\ 0 \\ 0 \\ 0 \\ \pm i\alpha \\ -\alpha \\ 0 \end{pmatrix} = -\gamma_- |\psi_1\rangle\,, \quad \checkmark$$

where we have used $-\gamma_- s + 2\alpha^2 = -\frac{\sqrt{s^2+8\alpha^2}-s}{2}s + \frac{8\alpha^2}{4} = \frac{s^2}{4} - \frac{\sqrt{s^2+8\alpha^2}}{2}s + \frac{s^2+8\alpha^2}{4} = \gamma_-^2$ for the first component in the second equality.

| $\|\psi_\#\rangle$ | $E$ | $A,s$ | $A,p_x$ | $A,p_y$ | $A,p_z$ | $B,s$ | $B,p_x$ | $B,p_y$ | $B,p_z$ |
|---|---|---|---|---|---|---|---|---|---|
| $\|\psi_1\rangle$ | $-\gamma_-$ | $-\gamma_-$ | 0 | 0 | 0 | 0 | $\pm i\alpha$ | $-\alpha$ | 0 |
| $\|\psi_2\rangle$ | $-\gamma_-$ | 0 | $\pm i\alpha$ | $\alpha$ | 0 | $-\gamma_-$ | 0 | 0 | 0 |
| $\|\psi_3\rangle$ | $-2\beta$ | 0 | $\mp i$ | 1 | 0 | 0 | $\mp i$ | $-1$ | 0 |
| $\|\psi_4\rangle$ | 0 | 0 | 0 | 0 | 1 | 0 | 0 | 0 | 0 |
| $\|\psi_5\rangle$ | 0 | 0 | 0 | 0 | 0 | 0 | 0 | 0 | 1 |
| $\|\psi_6\rangle$ | $\gamma_+$ | $\gamma_+$ | 0 | 0 | 0 | 0 | $\pm i\alpha$ | $-\alpha$ | 0 |
| $\|\psi_7\rangle$ | $\gamma_+$ | 0 | $\pm i\alpha$ | $\alpha$ | 0 | $\gamma_+$ | 0 | 0 | 0 |
| $\|\psi_8\rangle$ | $2\beta$ | 0 | $\pm i$ | $-1$ | 0 | 0 | $\mp i$ | $-1$ | 0 |

Table 3.3.: Eigenenergies (ordered from low to high) and components of the corresponding unnormalized eigenstates of $H_{sp}$ at the Dirac points, [Min (2006)]. The upper (lower) sign corresponds to $K$ ($K'$).

As expected from the hexagonal structure of graphene, the $s$, $p_x$ and $p_y$ orbitals couple to form an $sp_2$ hybrid. These hybridized states are referred to as $\sigma$ bands (bonding and

antibonding). The $p_z$ orbitals form the $\pi$ bands which are decoupled from the $\sigma$ bands. Both for $K$ and $K'$ the $\pi$ bands comprise a twofold degenerate manifold at $E = 0$, which we refer to as $D_K$ and $D_{K'}$, respectively. (We do *not* include real spin, yet.)

Carbon has six electrons, four of which occupy the $n = 2$ shell under consideration. With the energies given in [Saito (1992)] we find $-\gamma_- = -17.074\,\text{eV}$, $-2\beta = -12.106\,\text{eV}$, $\gamma_+ = 8.206\,\text{eV}$ and $2\beta = 12.106\,\text{eV}$ such that rows one through four in table 3.3 correspond to valence bands and rows five through eight to conduction bands. The resulting energy level diagram is shown in figure 3.2.

We infer that the Fermi energy corresponds to $E = 0$ on our energy scale and that the $\pi$ bands (rows four and five) are the relevant bands for electron/hole transport. The highest valence band and the lowest conduction band ($\pi$ bands) are degenerate and orthonormal, thus justifying the description of graphene as a gapless semiconductor.

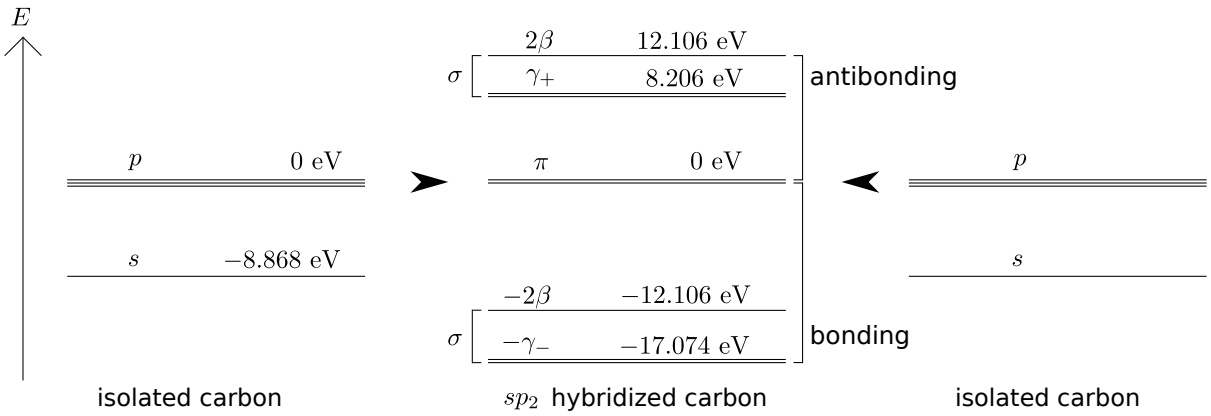


Figure 3.2.: The $n = 2$ orbitals in carbon hybridize to form bonding and antibonding $\sigma$ and $\pi$ bands. This $sp_2$ configuration explains the hexagonal structure of graphene. The vanishing gap between the highest valence band and the lowest conduction band justifies the terminology of a gapless semiconductor.

## 3.3. Intrinsic and extrinsic perturbations

We first address an individual atom $i$ within a graphene sheet. Relativistic effects lead to the atomic spin-orbit interaction

$$H_{AS,i} = -\frac{e}{4(m_e c)^2}\vec{s}\cdot\left(\vec{E}\times(\vec{p_c} - e\vec{A})\right),$$

where $\vec{s}$ are standard Pauli matrices that act on real spin and $\vec{p_c}$ is the canonical momentum, see e. g. [Burkard (QII)]. With the kinetic momentum $\vec{p} = \vec{p_c} - e\vec{A}$ and spin $\vec{S} := \hbar\vec{s}/2$ we infer

$$H_{AS,i} = \frac{e}{2(m_e c)^2}\frac{\vec{s}}{2}\cdot(\vec{\nabla}V\times\vec{p}) = \frac{e}{2\hbar(m_e c)^2}(\vec{\nabla}V\times\vec{p})\cdot\vec{S}\,. \tag{3.3}$$

The gradient $\vec{\nabla}V$ is greatest near the nuclei (otherwise $V \approx const$). In coordinates $\vec{r}_i$, which are centered at atom $i$, this gradient is

$$\vec{\nabla}V(r_i) = \frac{\partial V(r_i)}{\partial r_i}\frac{\vec{r}_i}{r_i}$$

such that the atomic spin-orbit operator becomes

$$H_{AS,i} = \frac{e}{2\hbar(m_e c)^2}\frac{\partial V(r_i)}{r_i \partial r_i}(\vec{r}_i \times \vec{p}) \cdot \vec{S} = \underbrace{\frac{e}{2\hbar(m_e c)^2}\frac{\partial V(r_i)}{r_i \partial r_i}}_{=:\xi(r_i)} \vec{L}_i \cdot \vec{S}\,,$$

where $\vec{L}_i$ is the angular momentum with respect to atom $i$. Suitable operators $P_{i,l}$ with $\sum_l P_{i,l} = 1$ project the angular momentum on orbital eigenvalues $l$. Each eigenvalue corresponds to a different prefactor $\xi_l$,

$$H_{AS,i} = \sum_l P_{i,l}\xi_l \vec{L}_i \cdot \vec{S}\,.$$

Finally, we include the summation over all atoms within the graphene sheet and get the operator that *intrinsically* couples an electron spin to the orbitals of those atoms:

$$H_{AS} = \sum_i H_{AS,i} = \sum_{i,l} P_{i,l}\xi_l \vec{L}_i \cdot \vec{S}\,.$$

Another mechanism is the quantum confined Stark effect, [Fox]. A back / top gate or impurities in the substrate / cap layer can give rise to an *extrinsic* electric field $\vec{E} = E\vec{e}_z$ perpendicular to the graphene sheet. The $z$-position of an electron with respect to the graphene plane relates to an electric dipole $\vec{d} = -ez\vec{e}_z$, which interacts with this extrinsic field:

$$H_{EF} = -\vec{d} \cdot \vec{E} = eEz\,.$$

The perturbations $H_{AS}$ and $H_{EF}$ shift the eigenenergies of $H_{sp}$ (see table 3.3). Next, we calculate these energy shifts and derive the effective spin-orbit hamiltonian.

## 3.4. Effective spin-orbit hamiltonian

To obtain an effective spin-orbit hamiltonian we calculate the second order energy corrections[3] caused by the perturbations $H_{AS}+H_{EF}$ and express them in terms of operators. We are only interested in states near the Dirac points and hence concentrate on the $\pi$ bands. The second order energy corrections of these states are given by (see e.g. [Nolting 5/2])

$$E^{(2)}_{m,n;K} = \sum_{l \notin D_K} \frac{\langle m|^{(0)} H_{AS} + H_{EF}|l\rangle^{(0)} \langle l|^{(0)} H_{AS} + H_{EF}|n\rangle^{(0)}}{E^{(0)}_{D_K} - E^{(0)}_l}\,, \tag{3.4}$$

[3]Similar to the explicit calculation of matrix elements below one easily checks that the first order corrections $\langle m|^{(0)} H_{AS} + H_{EF}|m\rangle^{(0)}$ vanish. $H_{AS}$: $L_z|m\rangle^{(0)} = 0$ and $\langle m|^{(0)} L_+ \pm L_-|m\rangle^{(0)} = 0$. $H_{EF}$: see symmetry argument below.

where $m, n \in D_K$. An equivalent expression holds for $E^{(2)}_{m,n;K'}$. The summation runs over all rows of table 3.3 but rows four and five. Obviously, we need the matrix elements $H_{AS;m,l}$ and $H_{EF;m,l}$. We find for example

$$\begin{aligned}
\langle\psi_4|H_{AS}|\psi_2\rangle &= i\alpha\langle A,p_z|H_{AS}|A,p_x\rangle + \alpha\langle A,p_z|H_{AS}|A,p_y\rangle - \gamma_- \underbrace{\langle A,p_z|H_{AS}|B,s\rangle}_{=0} \\
&= i\alpha\langle p_z|\xi \underbrace{L_y}_{\substack{\uparrow \\ iL_y = L_+ - L_x}} S_y|p_x\rangle + \alpha\langle p_z|\xi \underbrace{L_x}_{\substack{\uparrow \\ = L_+ - iL_y}} S_x|p_y\rangle \\
&= \alpha\frac{\xi S_y}{\sqrt{2}}\,(\underbrace{\langle 1,0|L_+|1,-1\rangle}_{=\hbar\sqrt{2}} - \underbrace{\langle 1,0|L_+|1,+1\rangle}_{=0}) \\
&\quad +\alpha\frac{i\xi S_x}{\sqrt{2}}\,(\overbrace{\langle 1,0|L_+|1,-1\rangle}^{=\hbar\sqrt{2}} + \overbrace{\langle 1,0|L_+|1,+1\rangle}^{=0}) \\
&= \alpha\xi\hbar(S_y + iS_x) = i\alpha\xi\hbar S_- \,.
\end{aligned}$$

In the first step we split the states in their explicit components listed in table 3.3 (fourth and second row) and use sublattice orthonormality[4]. Then we simplify $H_{AS} = \xi(L_xS_x + L_yS_y + L_zS_z)$ for a specific site (atom $i$). Here, only $p$ orbitals are considered such that we can combine their according projection $P_{i,1}$ as well as $\xi_1$ in $\xi$. We also use the step operator for angular momentum, $L_+ := L_x + iL_y$, and $L_i|p_i\rangle = 0$ $(i = x, y, z)$. In the third equality we substitute (see e.g. [Haken & Wolf])

$$|p_x\rangle = \frac{1}{\sqrt{2}}(|1,-1\rangle - |1,+1\rangle)\,, \quad |p_y\rangle = \frac{i}{\sqrt{2}}(|1,-1\rangle + |1,+1\rangle)\,, \quad |p_z\rangle = |1,0\rangle$$

and use $L_+|l,m\rangle = \sqrt{l(l+1) - m(m+1)}\hbar|l,m+1\rangle$. The result is an operator that acts on real spin, which has not been considered up to now. We note that the components of $|\psi_2\rangle$ have a combined amplitude of $\sqrt{\gamma_-^2 + 2\alpha^2}$ such that the state is unnormalized.

For $H_{EF}$ we demonstrate

$$\begin{aligned}
\langle\psi_4|H_{EF}|\psi_1\rangle &= -\gamma_-\langle A,p_z|H_{EF}|A,s\rangle + i\alpha\underbrace{\langle A,p_z|H_{EF}|B,p_x\rangle}_{=0} - \alpha\underbrace{\langle A,p_z|H_{EF}|B,p_y\rangle}_{=0} \\
&= -\gamma_-\underbrace{\langle p_z|eEz|s\rangle}_{=:eEz_0} = -\gamma_- eEz_0\mathbb{1}_2\,,
\end{aligned}$$

where we respect real spin explicitly with the unit matrix in the last step. The integral $\langle p_z|z|s\rangle$ is assigned the value $z_0$ and indeed all other integrals $\langle p_z|z|\mu\rangle$ $(\mu \neq s)$ vanish for symmetry reasons, for example

$$\langle p_z|z|p_x\rangle \propto \int_{-\infty}^{\infty} p_z(x)p_x(x)\,\mathrm{d}x = 0\,,$$

since $p_z(x)$ is even in $x$ and $p_x(x)$ is odd. We need to consider the same normalization as for $H_{AS}$. An overview of all matrix elements and normalizations is given in table

[4]Sublattice orthonormality can be confirmed using a representation of Wannier functions centered on different sites.

3.4. The explicit calculation of $E^{(2)}_{m,n;K}$ is straightforward and lengthy and therefore we do not demonstrate it here. The results for $K$ and $K'$ are shown in table 3.5. With[5] $S_+ = ((0,1),(0,0))$ and $S_- = ((0,0),(1,0))$ we include real spin explicitly so that we obtain operators acting on spin states,

$$E^{(2)}_{m,n;K/K'} \to \hat{E}^{(2)}_{m,n;K/K'}\,.$$

| Orbital | $\lvert\psi_1\rangle$ | $\lvert\psi_2\rangle$ | $\lvert\psi_3\rangle$ | $\lvert\psi_6\rangle$ | $\lvert\psi_7\rangle$ | $\lvert\psi_8\rangle$ |
|---|---|---|---|---|---|---|
| $\langle\psi_4\rvert$ | $\mathbb{0}_2$ | $i\alpha\xi S_-$ | $i\xi S_+$ | $\mathbb{0}_2$ | $i\alpha\xi S_-$ | $-i\xi S_+$ |
| $\langle\psi_5\rvert$ | $-i\alpha\xi S_+$ | $\mathbb{0}_2$ | $-i\xi S_-$ | $-i\alpha\xi S_+$ | $\mathbb{0}_2$ | $-i\xi S_-$ |
| $\langle\psi_4\rvert$ | $-\gamma_- eEz_0\mathbb{1}_2$ | $\mathbb{0}_2$ | $\mathbb{0}_2$ | $\gamma_+ eEz_0\mathbb{1}_2$ | $\mathbb{0}_2$ | $\mathbb{0}_2$ |
| $\langle\psi_5\rvert$ | $\mathbb{0}_2$ | $-\gamma_- eEz_0\mathbb{1}_2$ | $\mathbb{0}_2$ | $\mathbb{0}_2$ | $\gamma_+ eEz_0\mathbb{1}_2$ | $\mathbb{0}_2$ |
| Amp. | $\sqrt{\gamma_-^2+2\alpha^2}$ | $\sqrt{\gamma_-^2+2\alpha^2}$ | 2 | $\sqrt{\gamma_+^2+2\alpha^2}$ | $\sqrt{\gamma_+^2+2\alpha^2}$ | 2 |

Table 3.4.: Matrix elements of $H_{AS}$ (top) and $H_{EF}$ (middle) that enter (3.4) at the $K$ point. According results can be obtained for $K'$. For correct normalization each element needs to be divided by the amplitude listed in the bottom row.

| Orbital | $\lvert\psi_4,\uparrow\rangle$ | $\lvert\psi_4,\downarrow\rangle$ | $\lvert\psi_5,\uparrow\rangle$ | $\lvert\psi_5,\downarrow\rangle$ |
|---|---|---|---|---|
| $\langle\psi_4,\uparrow\rvert$ | 0 | 0 | 0 | 0 |
| $\langle\psi_4,\downarrow\rvert$ | 0 | $\frac{s\xi^2}{4\alpha^2}$ | $-\frac{ieEz_0\xi}{\alpha}$ | 0 |
| $\langle\psi_5,\uparrow\rvert$ | 0 | $\frac{ieEz_0\xi}{\alpha}$ | $\frac{s\xi^2}{4\alpha^2}$ | 0 |
| $\langle\psi_5,\downarrow\rvert$ | 0 | 0 | 0 | 0 |
| $\langle\psi_4,\uparrow\rvert$ | $\frac{s\xi^2}{4\alpha^2}$ | 0 | 0 | $-\frac{ieEz_0\xi}{\alpha}$ |
| $\langle\psi_4,\downarrow\rvert$ | 0 | 0 | 0 | 0 |
| $\langle\psi_5,\uparrow\rvert$ | 0 | 0 | 0 | 0 |
| $\langle\psi_5,\downarrow\rvert$ | $\frac{ieEz_0\xi}{\alpha}$ | 0 | 0 | $\frac{s\xi^2}{4\alpha^2}$ |

Table 3.5.: Energy corrections from (3.4) at $K$ (top) and $K'$ (bottom) with the explicit inclusion of real spin.

Recalling $\lvert\psi_{4(5)}\rangle = \lvert A(B), p_z\rangle$ and with

$$\frac{s\xi^2}{4\alpha^2} = \frac{s\xi^2}{9(sp\sigma)^2} = -2\underbrace{\frac{|s|\xi^2}{18(sp\sigma)^2}}_{=:\lambda_I} = -2\lambda_I \quad (s = -8.868\,\mathrm{eV})$$

and

$$\frac{ieEz_0\xi}{\alpha} = 2i\underbrace{\frac{eEz_0\xi}{3(sp\sigma)}}_{=:\lambda_R} = 2i\lambda_R$$

[5]For simplicity we set $\hbar$ to unity.

we can combine these operators to the effective spin-orbit hamiltonian near the Dirac points:

$$\tilde{H}_{SO} = -\lambda_I \mathbb{1}_4 + \lambda_I \sigma_z \tau_z s_z - \lambda_R (\sigma_x \tau_z s_y - \sigma_y s_x) \,.$$

We select the $K$ ($K'$) point with $\tau_z = +1$ ($-1$), $\vec{\sigma}$ refers to pseudo-spin (section 2.3) with $\sigma_z$ eigenstates localized on a definite site and $\vec{s}$ describes real spin. Representing both $\vec{\sigma}$ and $\vec{s}$ with standard Pauli matrices we confirm

$$\begin{aligned} \tilde{H}_{SO,K} &= -\lambda_I \mathbb{1}_4 + \lambda_I \begin{pmatrix} s_z & \mathbb{0}_2 \\ \mathbb{0}_2 & -s_z \end{pmatrix} - \lambda_R \left( \begin{pmatrix} \mathbb{0}_2 & s_y \\ s_y & \mathbb{0}_2 \end{pmatrix} - \begin{pmatrix} \mathbb{0}_2 & -is_x \\ is_x & \mathbb{0}_2 \end{pmatrix} \right) \\ &= -2\lambda_I \begin{pmatrix} 0 & 0 & 0 & 0 \\ 0 & 1 & 0 & 0 \\ 0 & 0 & 1 & 0 \\ 0 & 0 & 0 & 0 \end{pmatrix} + 2i\lambda_R \begin{pmatrix} 0 & 0 & 0 & 0 \\ 0 & 0 & -1 & 0 \\ 0 & 1 & 0 & 0 \\ 0 & 0 & 0 & 0 \end{pmatrix} , \end{aligned}$$

at the $K$ point (see table 3.5).

The constant $-\lambda_I \mathbb{1}_4$ can be omitted as it merely regauges the energy scale of the $\pi$ bands:

$$H_{SO} = \lambda_I \sigma_z \tau_z s_z - \lambda_R (\sigma_x \tau_z s_y - \sigma_y s_x) \,. \tag{3.5}$$

We emphasize that this result agrees with [Min (2006), Kane (2005)] up to a different sign[6] in front of $\lambda_R$, that results from a lattice orientation consistent with (2.8).

There has been disagreement concerning numerical values of $\lambda_I$ and $\lambda_R$ [Kane (2005), Min (2006), Gmitra (2009)]. We stick to the latest results, which suggest $\lambda_I = 12\,\mu\text{eV}$ and $\lambda_R = 5\,\mu\text{eV} \times E[\text{V/nm}]$.

[6] In table 3.5 the sign in front of $\lambda_R$ is different from [Min (2006)]. This arises from an interchange of $A$ and $B$ sublattices (2.1) and $K$ and $K'$ (2.2), (3.2) with respect to the lattice orientation in that reference.

# 4. Electronic states in armchair nanoribbons

Due to the Klein paradox it is hard to spatially confine electrons in graphene. Recher and Trauzettel review three systems that allow for confinement via creation of band gap [Recher (2010)]:

- Nanoribbons with armchair boundaries,
- a disc in single-layer graphene and
- a disc in bilayer graphene.

Focussing on the first system, we explicitly derive the band gap and properties of electrostatically confined electronic states in this chapter.

## 4.1. Gapped graphene from armchair boundaries

We consider the hamiltonian (2.9) and follow [Brey (2006)] and [Castro Neto (2009)] in this section. Assuming the GNR to be aligned with the $y$-direction, translational invariance ensures plane waves $e^{iky}$ along this direction, see figure 4.1.

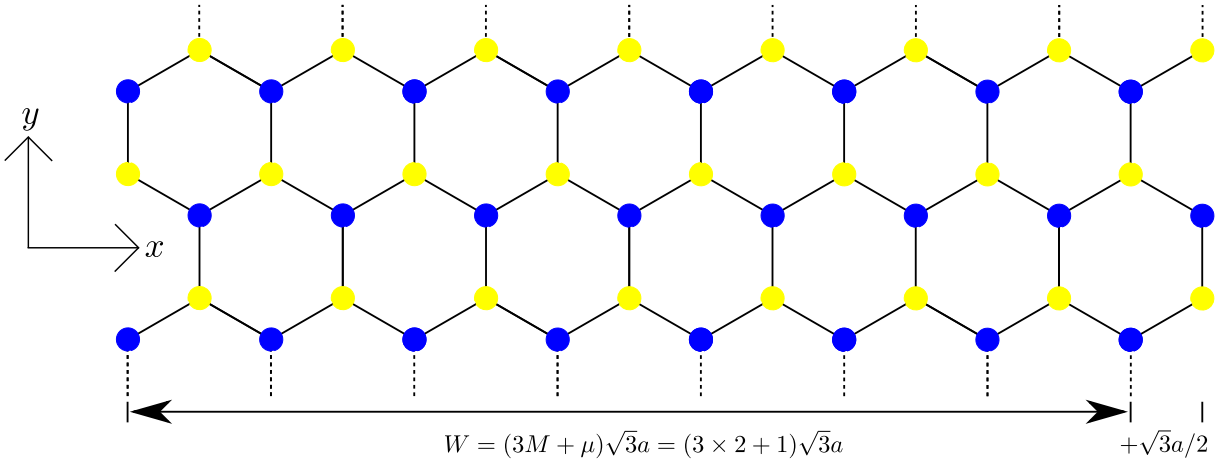


Figure 4.1.: Translational invariance ensures plane waves along the $y$-direction. With $W = (3M + \mu)\sqrt{3}a$ the shown ribbon ($\mu = 1$) is gapped or *semiconducting*. The overall ribbon width is half a unit cell more than the width for fixed $y$.

The ansatz $\psi^{(K)}_{A/B}(x,y) = \chi^{(K)}_{A/B}(x)e^{iky}$, $\psi^{(K')}_{A/B}(x,y) = -\chi^{(K')}_{A/B}(x)e^{iky}$ leads to

$$E\begin{pmatrix}\chi^{(K)}_A(x)\\ \chi^{(K)}_B(x)\end{pmatrix} = -i\hbar v_F\begin{pmatrix}0 & \partial_x + k\\ \partial_x - k & 0\end{pmatrix}\begin{pmatrix}\chi^{(K)}_A(x)\\ \chi^{(K)}_B(x)\end{pmatrix} = -i\hbar v_F\begin{pmatrix}(\partial_x + k)\chi^{(K)}_B(x)\\ (\partial_x - k)\chi^{(K)}_A(x)\end{pmatrix}.$$

We infer

$$\begin{aligned} & E\chi^{(K)}_A(x) = -i\hbar v_F(\partial_x + k)\chi^{(K)}_B(x) = -\frac{\hbar^2 v_F^2(\partial_x^2 - k^2)}{E}\chi^{(K)}_A(x)\,,\\ \Rightarrow\quad & \partial_x^2\chi^{(K)}_A(x) = -\underbrace{\left(\frac{E^2}{\hbar^2 v_F^2} - k^2\right)}_{=:\,q_n^2}\chi_A(x) \end{aligned} \tag{4.1}$$

and $\partial_x^2\chi^{(K)}_B(x) = -q_n^2\chi_B(x)$. Similar equations hold for the $K'$ components leading to the general solutions

$$\chi^{(K)}_j(x) = a_j e^{iq_n x} + b_j e^{-iq_n x} \quad\text{and}\quad \chi^{(K')}_j(x) = c_j e^{iq_n x} + d_j e^{-iq_n x}\,,\quad (j\in\{A,B\})\,.$$

Since an electron cannot exist beyond the ribbon edges its wavefunction must be zero at the boundaries, just like at the rim of an infinite pot potential. Armchair GNR are characterized by the fact that their edges involve both $A$ and $B$ sublattices, figure 4.1. Consequently, both wavefunctions $\psi_j(x,y) = e^{i\vec{K}\cdot\vec{r}}\psi^{(K)}_j(x,y) + e^{i\vec{K}'\cdot\vec{r}}\psi^{(K')}_j(x,y)$ must vanish for $x = 0, W$. With $K = 4\pi/3\sqrt{3}a$ (see (2.2)) this requires[1]

$$\begin{aligned} 0 &= \psi_j(0,y) = \psi^{(K)}_j(0,y) + \psi^{(K')}_j(0,y) \quad\Rightarrow\quad 0 = a_j + b_j - c_j - d_j\,, \\ 0 &= \psi_j(W,y) = e^{iKW}\psi^{(K)}_j(W,y) + e^{-iKW}\psi^{(K')}_j(W,y)\,. \end{aligned} \tag{4.2}$$

With $a_j = d_j$, $b_j = c_j = 0$, the former condition is satisfied and the second becomes

$$\begin{aligned} & 0 = a_j e^{i(q_n+K)W} - a_j e^{-i(q_n+K)W}\,,\\ \Rightarrow\quad & e^{2i(q_n+K)W} = e^{2i\pi\tilde{n}}\,,\\ \Rightarrow\quad & q_n = \frac{\pi\tilde{n}}{W} - K\,, \end{aligned} \tag{4.3}$$

with an integer $\tilde{n}$. We write the width[2] as $W = (3M+\mu)\sqrt{3}a$, where $M$ is a positive integer, $\mu\in\{-1,0,+1\}$ and $\sqrt{3}a = 2.46\,\text{Å}$ is the lattice constant, and resolve

$$q_n = \frac{\pi\tilde{n}}{(3M+\mu)\sqrt{3}a} - \frac{4\pi}{3\sqrt{3}a} = \frac{\pi}{\sqrt{3}a}\left(\frac{\tilde{n}}{3M+\mu} - \frac{4}{3}\right).$$

[1] With $2KW = 2(4\pi/3)(3M+\mu) = 8M\pi + \mu 8\pi/3 \to \mu(6+2)\pi/3 \to \mu 2\pi/3$ Trauzettel *et al.* rewrite these boundary conditions as
$\psi^{(K)}_j(0,y) = -\psi^{(K')}_j(0,y)$ and $\psi^{(K)}_j(W,y) = -e^{-i2KW}\psi^{(K')}_j(W,y) = -e^{-i\mu 2\pi/3}\psi^{(K')}_j(W,y)$.

[2] While we consider the width *for a given y* it is also possible to deal with the *overall* width of the ribbon. The latter case describes the transverse separation of the outmost left atoms from the outmost right atoms, thus augmenting the width by half a unit cell. From (4.3) one easily confirms that the ribbon becomes gapless for $\tilde{W} = ((3M+1)+1/2)\sqrt{3}a$, [Brey (2006)]. This means that the ribbon shown in figure 4.1 would be gapped for $W$ and gapless for $\tilde{W}$. ↯
We point out that the quasi-relativistic Dirac hamiltonian only describes the slowly varying envelope function and does not account for width shifts by half a unit cell. Both ansatzes produce gapped and ungapped ribbons; the physical reality is to be identified by experiment.

The term in parentheses vanishes for $4(M+\mu/3) = \tilde{n} \in \mathbb{Z}$, i.e. only for $\mu = 0$. Since $E = \pm\hbar v_F\sqrt{q_n^2 + k^2}$ (see (4.1) and chapter 2) a gap

$$\Delta E = 2\hbar v_F q_n \tag{4.4}$$

between the valence and conduction band opens for $\mu = \pm 1$. This is a direct result of the armchair topology. Gapless GNR ($\mu = 0$) are usually referred to as being *metallic*, and gapped GNR ($\mu = \pm 1$) as being *semiconducting*.

The transverse wavenumber $q_n$ can be simplified to

$$\begin{aligned} q_n &= \frac{\pi\tilde{n} - KW}{W} = \frac{\pi\tilde{n} - 4\pi(M+\mu/3)}{W} = \frac{\pi}{W}\left(\underbrace{\tilde{n} - 4M - \mu}_{=:n} - \mu/3\right) \\ &= \frac{\pi}{W}(n - \mu/3)\,, \quad (n \in \mathbb{Z})\,. \end{aligned} \tag{4.5}$$

## 4.2. Electrostatically confined states

The calculations are based on [Trauzettel (2007)], with emphasis on the explicit form of electronic states. By virtue of the gap $\Delta E$ produced by armchair boundaries (4.4) it is possible to confine electrons with an electric potential $V(y)$. The low energy electrons in a QD of length $L$ (figure 4.2) are described by

$$-i\hbar v_F \begin{pmatrix} \sigma_x\partial_x + \sigma_y\partial_y & \mathbb{0}_2 \\ \mathbb{0}_2 & -\sigma_x\partial_x + \sigma_y\partial_y \end{pmatrix} \psi(x,y) + eV(y)\psi(x,y) = E\psi(x,y)\,, \tag{4.6}$$

where $\sigma_{x,y}$ are the standard Pauli matrices (see (2.9)) and

$$V(y) = \begin{cases} V_G\,, & 0 \le y \le L \text{ (gate region)}, \\ V_B\,, & \text{otherwise (barrier region)}. \end{cases}$$

We are free to use a negative phase in the $K'$ components of the four component envelope wavefunction $\psi = (\psi_A^{(K)}, \psi_B^{(K)}, -\psi_A^{(K')}, -\psi_B^{(K')})$. As mentioned above translational invariance ensures plane waves in the $y$-direction and the solutions of (4.6) are

$$\psi_{n,k}^{(+)}(x,y) = \chi_{n,k}^{(+)}(x)e^{iky}\,, \quad \psi_{n,k}^{(-)}(x,y) = \chi_{n,k}^{(-)}(x)e^{-iky}\,,$$

where

$$\begin{aligned} \chi_{n,k}^{(+)}(x) &= a_n^{(+)} \begin{pmatrix} 1 \\ z_{n,k} \\ 0 \\ 0 \end{pmatrix} e^{iq_n x} + b_n^{(+)} \begin{pmatrix} -z_{n,k} \\ 1 \\ 0 \\ 0 \end{pmatrix} e^{-iq_n x} \\ &\quad + c_n^{(+)} \begin{pmatrix} 0 \\ 0 \\ -z_{n,k} \\ 1 \end{pmatrix} e^{iq_n x} + d_n^{(+)} \begin{pmatrix} 0 \\ 0 \\ 1 \\ z_{n,k} \end{pmatrix} e^{-iq_n x} \end{aligned}$$

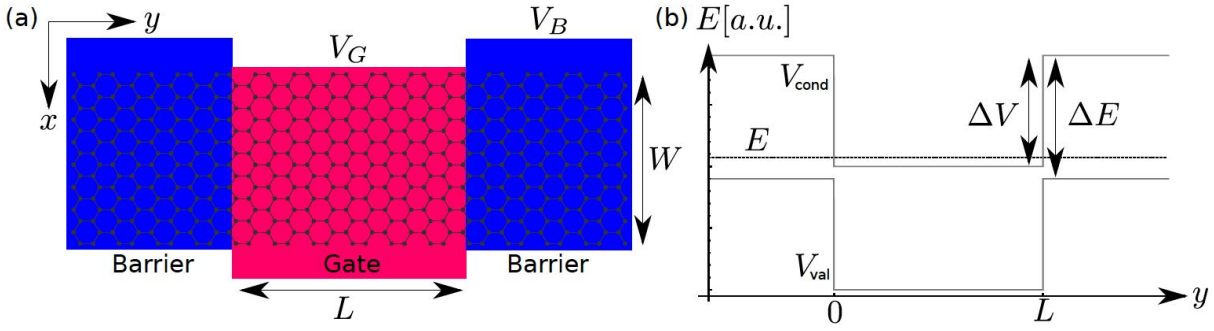


Figure 4.2.: The dot architecture is shown in (a). By applying different potentials (local potential indicated by color) to the barrier and gate regions it is possible to confine a particle. The armchair edges are crucial for the band gap $\Delta E$, see (4.4). The energy relations are depicted in (b). The conduction (valence) band is obtained by adding (subtracting) $\hbar v_F q_0$ to the local barrier/gate potential. A bound conduction band state with energy $E$ exists if $E > V_G + \hbar v_F q_0$ and $|E - V_B| < \hbar v_F q_0$ are satisfied.

and $\chi^{(-)}_{n,k}(x)$ accordingly (see [Trauzettel (2007)]). With

$$z_{n,k} = \pm \frac{q_n + ik}{\sqrt{q_n^2 + k^2}}\,, \tag{4.7}$$

$$E = eV(y) \pm \hbar v_F \sqrt{q_n^2 + k^2} \tag{4.8}$$

we confirm e.g. the $a_n^{(+)}$-term:

$$\begin{aligned}
&(-i\hbar v_F(\sigma_x\partial_x + \sigma_y\partial_y) + eV(y))\,\psi^{(K)}(x,y) \\
&\quad = \left(\hbar v_F \begin{pmatrix} 0 & q_n - ik \\ q_n + ik & 0 \end{pmatrix} + eV(y)\right) \begin{pmatrix} 1 \\ \pm\frac{q_n+ik}{\sqrt{q_n^2+k^2}} \end{pmatrix} e^{i(q_n x + ky)} \\
&\quad = \hbar v_F \begin{pmatrix} \pm\frac{q_n^2+ik}{\sqrt{q_n^2+k^2}} \\ q_n + ik \end{pmatrix} e^{i(q_n x + ky)} + eV(y)\psi^{(K)}(x,y) \\
&\quad = \pm\hbar v_F \sqrt{q_n^2+k^2} \begin{pmatrix} 1 \\ z_{n,k} \end{pmatrix} e^{i(q_n x + ky)} + eV(y)\psi^{(K)}(x,y) = E\psi^{(K)}(x,y)\,. \quad \checkmark
\end{aligned} \tag{4.9}$$

The $+$ $(-)$ sign in equations (4.7) to (4.9) corresponds to the conduction (valence), leading to the band gap $\Delta E$ (4.4). Due to (4.8) the longitudinal wavenumber depends on $V(y)$, $k = k(y)$, and we substitute it by $k_G$ ($k_B$) in the gate (barrier) region. In fact, $k_G$ is real and $k_B$ is purely imaginary for a bound state:

$$k_G = \sqrt{\left(\frac{E - eV_G}{\hbar v_F}\right)^2 - q_n^2}\,, \quad k_B = i\sqrt{q_n^2 - \left(\frac{E - eV_B}{\hbar v_F}\right)^2}\,. \tag{4.10}$$

For an armchair GNR the boundary conditions (4.2) apply and again we conform them with $a_n^{(\pm)} = d_n^{(\pm)}$, $b_n^{(\pm)} = c_n^{(\pm)} = 0$ and a transverse wavenumber $q_n$ that is quantized according to (4.5), where we are free to choose $\mu = \pm 1$.

A bound state will have the form

$$\psi(x,y) = \begin{cases} \alpha'_n \chi^{(-)}_{n,k_B}(x) e^{-ik_B y}\,, & \text{if } y \le 0, \\ \beta'_n \chi^{(+)}_{n,k_G}(x) e^{ik_G y} + \gamma'_n \chi^{(-)}_{n,k_G}(x) e^{-ik_G y}\,, & \text{if } 0 \le y \le L, \\ \delta'_n \chi^{(+)}_{n,k_B}(x) e^{ik_B (y-L)}\,, & \text{if } L \le y, \end{cases} \tag{4.11}$$

where the coefficients follow from the matching conditions at $y = 0, L$,

$$\begin{aligned} \alpha_n \begin{pmatrix} z_{n,k_B} \\ 1 \end{pmatrix} &= \beta_n \begin{pmatrix} 1 \\ z_{n,k_G} \end{pmatrix} + \gamma_n \begin{pmatrix} z_{n,k_G} \\ 1 \end{pmatrix}, \\ \delta_n \begin{pmatrix} 1 \\ z_{n,k_B} \end{pmatrix} &= \beta_n \begin{pmatrix} 1 \\ z_{n,k_G} \end{pmatrix} e^{ik_G L} + \gamma_n \begin{pmatrix} z_{n,k_G} \\ 1 \end{pmatrix} e^{-ik_G L}, \end{aligned}$$

with $\alpha_n = \alpha'_n a_n^{(-)}$, $\beta_n = \beta'_n a_n^{(+)}$, $\gamma_n = \gamma'_n a_n^{(-)}$ and $\delta_n = \delta'_n a_n^{(+)}$. These conditions can be written in matrix form and the determinant of said matrix has to vanish such that its kernel contains the coefficients. Further calculations follow exactly the supplementary

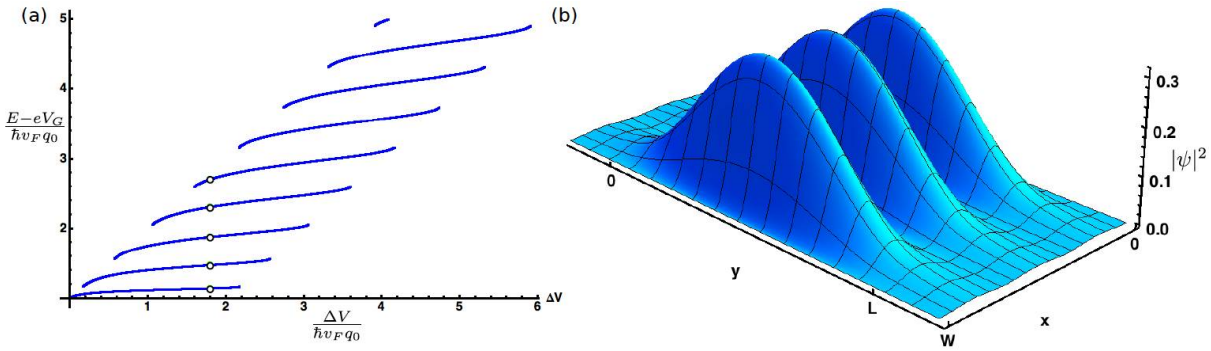


Figure 4.3.: Solutions of (4.12) are shown in (a) for $q_{n=0}$. We assume $\mu = -1$ and $L = 5W$. There are five bound states for $q_0$ and $\Delta V = 1.8\hbar v_F q_0$, as indicated by the circles. Each circle corresponds to another *longitudinal* excitation. Further bound states exist for higher *transverse* excitations $q_n$, e.g. for $E - V_G \ge \hbar v_F q_1 = 4\hbar v_F q_0$ (see (4.5), not shown). The state plotted in (b) corresponds to the lowest circle, i.e. to the absolute ground state for said $\Delta V$. The transverse oscillation comes about from the phases $e^{\pm iKx}$ that need to be included to conform the boundary conditions for armchair edges, (4.2). Due to this oscillation we assume $W = 2\sqrt{3}a$ in the last subfigure for perceptibility.

information for [Trauzettel (2007)] and we only repeat that bound conduction band states exist for $E - V_G \ge \hbar v_F q_n \ge |E - V_B|$ and that the determinant vanishes if the wavenumbers satisfy the transcendental equation

$$\tan(k_G L) = \frac{-ik_G k_B}{\pm\sqrt{q_n^2 + k_B^2}\sqrt{q_n^2 + k_G^2} - q_n^2}\,, \tag{4.12}$$

where $\pm = \operatorname{sgn}(E - V_B)$. The normalization condition is

$$\iint |e^{iKx}\psi^{(K)}_{A/B}(x,y) + e^{-iKx}\psi^{(K')}_{A/B}(x,y)|^2 \mathrm{d}x\,\mathrm{d}y = \frac{1}{2}\,.$$

Solutions of (4.12) are plotted in figure 4.3.

# 5. Classical vibrations in a graphene nanoribbon

Usual magnetic fields of $B \approx 1\,\mathrm{T}$ relate to a Zeeman energy that only allows for coupling to low energy acoustical phonons at the center of the Brillouin zone. For sufficiently long wavelengths, the atomic structure becomes negligible such that these low energy acoustic phonons can be described by a classical continuum model. This model has been studied extensively in [Landau & Lifschitz] and [Chaikin & Lubensky] and in appendix A we review some relevant quantities.

## 5.1. Elastic specifications

We assume the GNR to lie in the $x-y$-plane as depicted in figure 5.1. Its dimension along the $x$-direction is referred to as width $W$. The length[1] along the $y$-direction is much larger than $W$ and although physically finite we can assume it to be infinite by imposing periodic boundaries. Typical values are $L \sim 1\,\mu\mathrm{m}$ and $W \sim 30\,\mathrm{nm}$ [Jiao (2009), Kosynkin (2009), Li (2008)]. It is unclear what thickness to assign to a monatomic layer. Moreover, we need an effective thickness that relates to the elastic properties of graphene. Since such a value is unknown it is common to use the interlayer spacing in graphite, $h = 3.4\,\text{Å}$ [Faccio (2009), Lee (2008), Reddy (2006)].

The mass density per area $\rho$ can be calculated from the atomic distance in graphene, $a = 1.42\,\text{Å}$, and the standard atomic weight of carbon, $m_C = 12.01\,\mathrm{u}$. There are two atoms per unit cell (see figure 2.1) and we find

$$\rho = \frac{2m_C}{2(3a\,\sqrt{3}a/2)} = \frac{2m_C}{3\sqrt{3}a^2} = \frac{2}{3\sqrt{3}} \cdot \frac{12.01 \times 1.6605 \times 10^{-27}\,\mathrm{kg}}{(1.42 \times 10^{-10}\,\mathrm{m})^2} = 3.81 \times 10^{-7}\,\frac{\mathrm{kg}}{\mathrm{m}^2}\,.$$

Most elastic constants depend on several parameters like temperature or stress such that different values occur throughout the literature. Moreover, there are relations between some constants (see (A.34), (A.35), (A.14) and (A.22)). Eventually, the right elastic constants will be settled by experiment.

Cited values for Poisson's ratio $\sigma$ range from 0.145 to 0.416, [Reddy (2006)] but cumulate around $\sigma = 0.16$ [Lee (2008), Faccio (2009), Kudin (2001)]. This value is also consistent with relations to other elastic constants.

[1] Note, that here, $L$ describes the length of the *whole* ribbon while in the previous chapter we have used the same letter to specify the QD dimension.

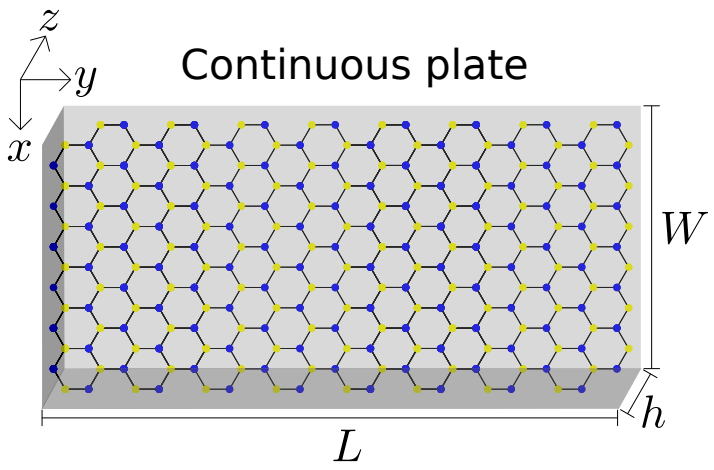


Figure 5.1.: For low energy acoustic phonons near the center of the Brillouin zone the atomic structure of the material becomes negligible such that the continuum model is justified. For GNR the inequalities $L \gg W \gg h$, where $h$ is the interlayer spacing of graphite, hold ($L \sim 1\,\mu$m, $W \sim 30\,$nm and $h = 3.4\,$Å).

While the most common literature value for Young's modulus is $\mathcal{E} = 1\,$TPa [Lee (2008), Faccio (2009), Kudin (2001)], a much smaller value, namely $0.5\,$TPa, has been found in at least one experiment [Frank (2007)]. In effect, only the product of Young' s modulus and thickness, $\mathcal{E}h$, will enter our calculations. According to [Faccio (2009)] this product increases significantly with decreasing width of the GNR, starting from a ribbon width of ten atoms. The width $W = 30\,$nm corresponds to more than a hundred atoms such that the bulk value $\mathcal{E}h = 3.4\,$TPa Å is a reasonable choice.

With Poisson's ratio and Young's modulus fixed we turn to expressions (see (A.34) and (A.35) below) for the bulk modulus, $B$, and the shear modulus, $\mu$:

$$\begin{aligned} B &= \frac{\mathcal{E}h}{2(1-\sigma)} = \frac{3.4\,\text{TPa Å}}{2(1-0.16)} = 2.024\,\text{TPa Å} = 12.63\,\frac{\text{eV}}{\text{Å}^2}\,, \\ B+\mu &= \frac{\mathcal{E}h}{1-\sigma^2} = \frac{3.4\,\text{TPa Å}}{1-0.0256} = 3.489\,\text{TPa Å} = 21.78\,\frac{\text{eV}}{\text{Å}^2}\,. \end{aligned}$$

These values compare well with literature, where we find $B = 11\,\text{eV/Å}^2$, $\mu = 9.4\,\text{eV/Å}^2$ and $B + \mu = 20\,\text{ev/Å}^2$ [Gazit (2009), Kudin (2001)]).

So far the choice of elastic constants is self-consistent. It has been shown that the bending rigidity of graphene, $\kappa$, decreases with increasing temperature, [Liu (2009)]. Since temperature dependencies for (A.22) are not known we do not consider this relation here but choose the literature value for zero temperature, $\kappa = 1.1\,$eV [Fasolino (2007), Gazit (2009), Kudin (2001)]. Below, we list the choice of elastic constants as used in our calculations.

| | |
|---|---|
| Mass density | $\rho = 3.81 \cdot 10^{-7}\,\mathrm{kg/m^2}$ |
| Thickness | $h = 3.4\,\text{Å}$ |
| Young's modulus | $\mathfrak{E} = 1.0\,\mathrm{TPa}$ |
| Poisson's ratio | $\sigma = 0.16$ |
| Bulk modulus | $B = 12.63\,\mathrm{eV/Å^2}$ |
| Shear modulus | $\mu = 9.15\,\mathrm{eV/Å^2}$ |
| Bending rigidity | $\kappa = 1.1\,\mathrm{eV}$ |

Table 5.1.: Elastic constants that specify graphene. Note that the interlayer spacing of graphite is not necessarily the effective elastic thickness of graphene. None of the constants (but the mass density) have been definitely settled by experiment.

## 5.2. Wave equations and boundary conditions

When subjected to external areal forces $P_x$, $P_y$, $P_z$ a continuous body will be deformed until internal forces counteract these external forces. We describe the graphene ribbon as a thin, continuous plate as shown in figure 5.1 such that its equilibrium conditions are

$$\kappa \triangle^2 \zeta - P_z = 0$$

for out-of-plane deformations ($\zeta$ describes the vertical displacement $u_z$ of the *neutral plane* of a thin plate, see figure A.2; (A.24); $\Delta = \partial_x^2 + \partial_y^2$) and

$$\begin{aligned}(B+\mu)\frac{\partial^2 u_x}{\partial x^2} + \mu\frac{\partial^2 u_x}{\partial y^2} + B\frac{\partial^2 u_y}{\partial x \partial_y} + P_x &= 0\,,\\ (B+\mu)\frac{\partial^2 u_y}{\partial y^2} + \mu\frac{\partial^2 u_y}{\partial x^2} + B\frac{\partial^2 u_x}{\partial x \partial_y} + P_y &= 0\,.\end{aligned}$$

for in-plane deformations (see (A.36), (A.37)). It is straightforward to obtain wave equations describing the vibrations of said plate by replacing the external forces per area with the negative acceleration of these area elements,

$$\begin{aligned}P_x &= -\rho\ddot{u}_x\,,\\ P_y &= -\rho\ddot{u}_y\,,\\ P_z &= -\rho\ddot{\zeta}\,,\end{aligned}$$

where $\rho$ is the mass density per area. Consequently, out-of-plane vibrations need to satisfy the partial differential equation (PDE)

$$\rho\ddot{\zeta} = -\kappa\left(\partial_x^2 + \partial_y^2\right)^2 \zeta\,, \tag{5.1}$$

and[2] the in-plane vibrations are described by the coupled PDE

$$\begin{aligned}\rho\ddot{u}_x &= (B+\mu)\frac{\partial^2 u_x}{\partial x^2} + \mu\frac{\partial^2 u_x}{\partial y^2} + B\frac{\partial^2 u_y}{\partial x \partial_y}\,, \qquad (5.2)\\ \rho\ddot{u}_y &= (B+\mu)\frac{\partial^2 u_y}{\partial y^2} + \mu\frac{\partial^2 u_y}{\partial x^2} + B\frac{\partial^2 u_x}{\partial x \partial_y}\,.\end{aligned}$$

[2]These PDE agree with those previously found for carbon nanotubes, which can easily be checked by assuming an infinite nanotube radius in [Suzuura (2002)] or [Mariani (2009)].

Obviously, the PDE for out-of-plane vibrations is of fourth order while those for in-plane vibrations are of second order. This is due to the fact that for a two-dimensional material there is no direct restoring force for out-of-plane deformations while an in-plane displacement will be counteracted directly by neighboring material.

Explicit solutions to the PDE will depend on the boundary conditions. Since $L \gg W$, we assume a ribbon unbounded in the $y$-direction. For free boundaries no force and no torque may act on the ribbon edges ($x = 0, W$).

For out-of-plane deformations we find explicit expressions by minimizing the free energy, which would be augmented by a non-zero torque or force. From variation of the free energy we infer equations (A.25) and (A.26) in appendix A. In the case of a graphene ribbon these equations simplify to

$$\begin{aligned} \partial_x^2 \zeta + \sigma \partial_y^2 \zeta &= 0\,, \\ \partial_x \partial_y^2 \zeta &= 0 \end{aligned} \tag{5.3}$$

along the ribbon edges ($x = 0, W$; see (A.28), (A.29)). For in-plane deformations vanishing forces directly translate to vanishing components $\sigma_{xi}$ ($i = x, y, z$) of the stress tensor, (see figure A.1 and equation (A.31)). Since $\sigma_{xz}$ vanishes independently for the ribbon, we infer the boundary conditions from $\sigma_{xx} = \sigma_{xy} = 0$:

$$\begin{aligned} \partial_x u_x + \sigma \partial_y u_y &= 0\,, \\ \partial_x u_y + \partial_y u_x &= 0 \end{aligned} \tag{5.4}$$

at the ribbon edges ($x = 0, W$; see (A.32), (A.33)). Solutions of the PDE and boundary conditions listed here are shown in figures 5.5 (out-of-plane modes) and 5.8 (in-plane modes).

## 5.3. Solving the wave equations

Out-of-plane vibrations obey a PDE of fourth order, (5.1), while in-plane vibrations are described by two coupled PDEs of second order, (5.2). Since we assume no boundaries in the $y$-direction, $u_x(x, y, t)$, $u_y(x, y, t)$ and $\zeta(x, y, t)$ can be defined for $y \in (-\infty, \infty)$ and $t \in (-\infty, \infty)$. Fourier transformation[3] of the displacements in variables $y$ and $t$ leads to

$$\begin{aligned} \tilde{\zeta} &= \frac{1}{2\pi} \iint_{-\infty}^{\infty} \zeta e^{i(\omega t - qy)} \,\mathrm{d}t \,\mathrm{d}y\,, \\ \begin{pmatrix} \tilde{u}_x \\ \tilde{u}_y \end{pmatrix} &= \frac{1}{2\pi} \iint_{-\infty}^{\infty} \begin{pmatrix} u_x \\ u_y \end{pmatrix} e^{i(\omega t - qy)} \,\mathrm{d}t \,\mathrm{d}y\,, \end{aligned}$$

where $q$ is a wavenumber and $\omega$ an angular frequency. Both equations are independent from one another since there is no coupling between out-of-plane and in-plane modes.

[3] We use a mathematician's definition of Fourier transformation with the same prefactor $1/\sqrt{2\pi}$ for the transformation and its inverse.

Possible indices $_{xy}$ and $_{\zeta}$ for $q$ and $\omega$ have been omitted for simplicity. From the inverse transformations,

$$\begin{aligned}\zeta &= \frac{1}{2\pi}\iint_{-\infty}^{\infty}\tilde{\zeta}e^{i(qy-\omega t)}\,\mathrm{d}\omega\,\mathrm{d}q\,,\\ \begin{pmatrix}u_x\\u_y\end{pmatrix} &= \frac{1}{2\pi}\iint_{-\infty}^{\infty}\begin{pmatrix}\tilde{u}_x\\\tilde{u}_y\end{pmatrix}e^{i(qy-\omega t)}\,\mathrm{d}\omega\,\mathrm{d}q\,,\end{aligned}$$

we infer

$$\begin{aligned}\partial_t\zeta = -i\omega\zeta\,, &\qquad \partial_y\zeta = iq\zeta\,,\\ \partial_t u_x = -i\omega u_x\,, &\qquad \partial_y u_x = iqu_x\,,\\ \partial_t u_y = -i\omega u_y\,, &\qquad \partial_y u_y = iqu_y\,,\end{aligned}$$

and rewrite the displacements as

$$\begin{aligned}\zeta(x,y,t) &= f_\zeta(x)e^{i(qy-\omega t)}\,,\\ u_x(x,y,t) &= f_x(x)e^{i(qy-\omega t)}\,,\\ u_y(x,y,t) &= f_y(x)e^{i(qy-\omega t)}\,,\end{aligned}$$

where functions $f_{\zeta,x,y}(x)$ are defined for $x\in[0,W]$ and describe the transverse ($x$-) dependence of the deformations. This ansatz[4] greatly simplifies (5.1) and (5.2), which we rewrite as

$$\begin{aligned}&-\rho\omega^2 f_\zeta(x) = -\kappa\left(\partial_x^2-q^2\right)^2 f_\zeta(x)\,,\\ \Rightarrow\quad &-\rho\omega^2 f_\zeta(x)+\kappa\left(f_\zeta''''(x)-2q^2f_\zeta''(x)+q^4f_\zeta(x)\right)=0\,,\\ \Rightarrow\quad &f_\zeta''''(x)-2q^2f_\zeta''(x)+\left(q^4-\frac{\omega^2\rho}{\kappa}\right)f_\zeta(x)=0\,,\end{aligned}\tag{5.5}$$

and

$$\begin{aligned}-\rho\omega^2 f_x(x) &= (B+\mu)f_x''(x)-\mu q^2 f_x(x)+iBqf_y'(x)\,,\\ -\rho\omega^2 f_y(x) &= -(B+\mu)q^2 f_y(x)+\mu f_y''(x)+iBqf_x'(x)\,.\end{aligned}\tag{5.6}$$

These are ordinary differential equations (ODE), that only depend on one variable. The boundary conditions (5.3) and (5.4) simplify to

$$-q^2 f_\zeta'(x)=0\;\Rightarrow\; f_\zeta'(x)=0\,,\qquad x=0,W\,,\tag{5.7}$$

$$f_\zeta''(x)-\sigma q^2 f_\zeta(x)=0\,,\qquad x=0,W\,,\tag{5.8}$$

for out-of-plane modes and

$$f_x'(x)+i\sigma q f_y(x)=0\,,\qquad x=0,W\,,\tag{5.9}$$

$$f_y'(x)+iqf_x(x)=0\,,\qquad x=0,W\tag{5.10}$$

for in-plane modes. In order to get real displacements one may consider only the real- or imaginary part of $u_{\zeta,x,y}(x,y,t)$.

We have transformed the PDE to simpler ODE, for which provide explicit solutions below.

[4] In order to get real displacements one may consider only the real- or imaginary part of $u_{\zeta,x,y}(x,y,t)$ at the end of the calculation. In combination with phonon creation and annihilation operators, however, quantities $u_{\zeta,x,y}(x,y,t)$ only appear in off-diagonal matrix elements such that they may be complex (equation (6.12)).

### 5.3.1. Out-of-plane solutions

To solve the fourth order ODE for $f_\zeta$ we transform (5.5) to a first order ODE for a vector:

$$\begin{aligned} g_\zeta(x) &:= \begin{pmatrix} f_\zeta(x) \\ f'_\zeta(x) \\ f''_\zeta(x) \\ f'''_\zeta(x) \end{pmatrix}, \\ \Rightarrow\ g'_\zeta(x) &= \begin{pmatrix} f'_\zeta(x) \\ f''_\zeta(x) \\ f'''_\zeta(x) \\ f''''_\zeta(x) \end{pmatrix} = \underbrace{\begin{pmatrix} 0 & 1 & 0 & 0 \\ 0 & 0 & 1 & 0 \\ 0 & 0 & 0 & 1 \\ \frac{\omega^2\rho}{\kappa} - q^4 & 0 & 2q^2 & 0 \end{pmatrix}}_{=:A} \begin{pmatrix} f_\zeta(x) \\ f'_\zeta(x) \\ f''_\zeta(x) \\ f'''_\zeta(x) \end{pmatrix} = Ag_\zeta(x)\,. \end{aligned}$$

Applying theorem 1 of appendix B leads to the characteristic polynomial

$$\begin{aligned} \chi_A(\lambda) &= \det(\lambda\mathbb{I}_4 - A) = \det \begin{pmatrix} \lambda & -1 & 0 & 0 \\ 0 & \lambda & -1 & 0 \\ 0 & 0 & \lambda & -1 \\ -\frac{\omega^2\rho}{\kappa} + q^4 & 0 & -2q^2 & \lambda \end{pmatrix} \\ &= \lambda \det \begin{pmatrix} \lambda & -1 & 0 \\ 0 & \lambda & -1 \\ 0 & -2q^2 & \lambda \end{pmatrix} - (-1) \det \begin{pmatrix} 0 & -1 & 0 \\ 0 & \lambda & -1 \\ -\frac{\omega^2\rho}{\kappa} + q^4 & -2q^2 & \lambda \end{pmatrix} \\ &= \lambda\left(\left(\lambda^3\right) - \left(2q^2\lambda\right)\right) + \left(\left(q^4 - \frac{\omega^2\rho}{\kappa}\right) - (0)\right) = \lambda^4 - 2q^2\lambda^2 + q^4 - \frac{\omega^2\rho}{\kappa}\,. \end{aligned}$$

The roots of this expression are found via the common formula:

$$\begin{aligned} \lambda_\pm^2 &= \frac{2q^2 \pm \sqrt{4q^4 - 4\left(q^4 - \frac{\omega^2\rho}{\kappa}\right)}}{2} = q^2 \pm \sqrt{\frac{\omega^2\rho}{\kappa}} \\ \Rightarrow \quad \lambda_1 &= \sqrt{q^2 + \sqrt{\frac{\omega^2\rho}{\kappa}}}, \quad \lambda_2 = -\sqrt{q^2 + \sqrt{\frac{\omega^2\rho}{\kappa}}}, \\ \lambda_3 &= \sqrt{q^2 - \sqrt{\frac{\omega^2\rho}{\kappa}}}, \quad \lambda_4 = -\sqrt{q^2 - \sqrt{\frac{\omega^2\rho}{\kappa}}}\,. \end{aligned}$$

The radicand of $\lambda_{3,4}$ vanishes for $q = \pm(\omega^2\rho/\kappa)^{\frac{1}{4}}$, leading to a double root of $\chi_A$. This special case will be treated later. With single roots only the fundamental system is $\{e^{\lambda_1 x}, e^{\lambda_2 x}, e^{\lambda_3 x}, e^{\lambda_4 x}\}$, from which we construct the general solution

$$f_\zeta(x) = c_1 e^{\lambda_1 x} + c_2 e^{\lambda_2 x} + c_3 e^{\lambda_3 x} + c_4 e^{\lambda_4 x}\,.$$

A discrete choice of the coefficients $c_i$ is obtained by applying the boundary conditions to this general solution:

$$\begin{aligned}
(5.7),\ x=0 \quad &\Rightarrow \quad c_1\lambda_1 + c_2\lambda_2 + c_3\lambda_3 + c_4\lambda_4 = 0\,,\\
(5.7),\ x=W \quad &\Rightarrow \quad c_1\lambda_1 e^{\lambda_1 W} + c_2\lambda_2 e^{\lambda_2 W} + c_3\lambda_3 e^{\lambda_3 W} + c_4\lambda_4 e^{\lambda_4 W} = 0\,,\\
(5.8),\ x=0 \quad &\Rightarrow \quad c_1(\lambda_1^2-\sigma q^2) + c_2(\lambda_2^2-\sigma q^2) + c_3(\lambda_3^2-\sigma q^2) + c_4(\lambda_4^2-\sigma q^2) = 0\,,\\
(5.8),\ x=W \quad &\Rightarrow \quad c_1(\lambda_1^2-\sigma q^2)e^{\lambda_1 W} + c_2(\lambda_2^2-\sigma q^2)e^{\lambda_2 W}\\
&\qquad\quad +c_3(\lambda_3^2-\sigma q^2)e^{\lambda_3 W} + c_4(\lambda_4^2-\sigma q^2)e^{\lambda_4 W} = 0\,,
\end{aligned}$$

To obtain the coefficients, we write this system of equations in matrix form,

$$\underbrace{\begin{pmatrix} \lambda_1 & \lambda_2 & \lambda_3 & \lambda_4 \\ \lambda_1 e^{\lambda_1 W} & \lambda_2 e^{\lambda_2 W} & \lambda_3 e^{\lambda_3 W} & \lambda_4 e^{\lambda_4 W} \\ (\lambda_1^2-\sigma q^2) & (\lambda_2^2-\sigma q^2) & (\lambda_3^2-\sigma q^2) & (\lambda_4^2-\sigma q^2) \\ (\lambda_1^2-\sigma q^2)e^{\lambda_1 W} & (\lambda_2^2-\sigma q^2)e^{\lambda_2 W} & (\lambda_3^2-\sigma q^2)e^{\lambda_3 W} & (\lambda_4^2-\sigma q^2)e^{\lambda_4 W} \end{pmatrix}}_{=B(q,\omega)} \begin{pmatrix} c_1 \\ c_2 \\ c_3 \\ c_4 \end{pmatrix} = \begin{pmatrix} 0 \\ 0 \\ 0 \\ 0 \end{pmatrix}, \tag{5.11}$$

and demand

$$\det B(q,\omega) = 0\,. \tag{5.12}$$

This is an implicit correlation of parameters $q$ and $\omega$, which have been free so far: the dispersion relation. Roots $(q_0, \omega_0)$ of (5.12) are found numerically by MATHEMATICA via independent and step-wise variation of parameters $q$ and $\omega$. For any $q_0$ there are discrete values $\omega_0$, thus constituting the different branches of the dispersion, see figure 5.2 (a).

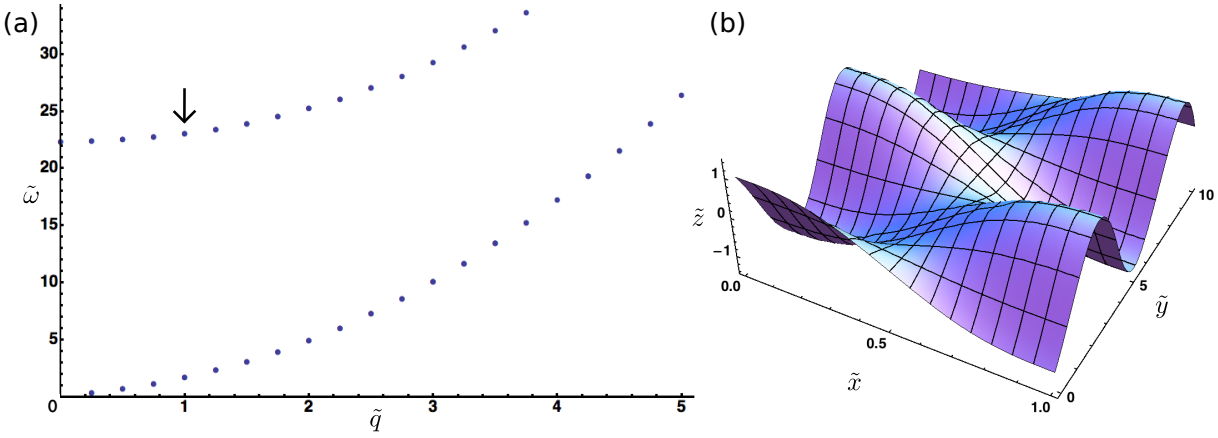


Figure 5.2.: (a) We plot the numerically found solutions of (5.12) into a $q$-$\omega$-graph, the dispersion. The arrow indicates the parameters for figure (b), where we plot the real part of the $\zeta(x, y, t = 0)$. This corresponds to the classical deformation of the ribbon. For the numerics, physical quantities are transformed to dimensionless quantities (indicated with " ˜ ") according to (5.17).

For a given root $(q_0, \omega_0)$ the matrix $B(q_0, \omega_0)$ does not have full rank. Its kernel, which is found numerically as well, contains coefficients $c_i$ that satisfy the boundary conditions

(5.11). These coefficients implicitly depend on parameters $q_0$ and $\omega_0$ and are fixed but up to a common constant. While this constant is free classically it is fixed for phonons by a normalization condition (section 6.1). Figure 5.2 (b) shows an unnormalized[5] solution that corresponds to parameters highlighted in figure 5.2 (a). A discussion of these results will follow in section 5.4.1.

We now turn to the special case $q = \pm(\omega^2\rho/\kappa)^{\frac{1}{4}}$, for which a double root of $\chi_A$ occurs. Strictly following theorem 1 we find the fundamental system $\{e^{\lambda_1 x}, e^{\lambda_2 x}, 1, x\}$ from which we construct the solution

$$f_\zeta(x) = c_1 e^{\lambda_1 x} + c_2 e^{\lambda_2 x} + c_3 + c_4 x\,. \tag{5.13}$$

The boundary conditions become

$$\underbrace{\begin{pmatrix} \lambda_1 & \lambda_2 & 0 & 1 \\ \lambda_1 e^{\lambda_1 W} & \lambda_2 e^{\lambda_2 W} & 0 & 1 \\ (\lambda_1^2 - \sigma q^2) & (\lambda_2^2 - \sigma q^2) & -\sigma q^2 & 0 \\ (\lambda_1^2 - \sigma q^2) e^{\lambda_1 W} & (\lambda_2^2 - \sigma q^2) e^{\lambda_2 W} & -\sigma q^2 & 0 \end{pmatrix}}_{=B(\omega)} \begin{pmatrix} c_1 \\ c_2 \\ c_3 \\ c_4 \end{pmatrix} = \begin{pmatrix} 0 \\ 0 \\ 0 \\ 0 \end{pmatrix},$$

where all $q$-dependencies in $B(q,\omega) = B(\omega)$ can be eliminated by substituting $q = \pm(\omega^2\rho/\kappa)^{\frac{1}{4}}$. The determinant,

$$\begin{aligned} \det B(\omega) = &-4\sigma \left(\omega\sqrt{\frac{\rho}{\kappa}}\right)^{5/2} \\ &\times \left(\sqrt{2}(-2+\sigma)\left(1 - \cosh\left(\sqrt{2\omega\sqrt{\frac{\rho}{\kappa}}}\right)\right) + \sigma\sqrt{\omega\sqrt{\frac{\rho}{\kappa}}}\sinh\left(\sqrt{2\omega\sqrt{\frac{\rho}{\kappa}}}\right)\right), \end{aligned}$$

has only one root at $\omega = 0$. This only root does not correspond to a vibration of the ribbon ($\omega = 0$) such that we can neglect the special case of a double root[6].

[5] In fact, the numerically found vector $(c_1, c_2, c_3, c_4)$ is normalized to unity, which does *not* correspond to the normalization necessary for quantization.

[6] Another argument is the following: While $q = \pm(\omega^2\rho/\kappa)^{\frac{1}{4}}$ allows for a continuous dispersion (solutions for any $q$) the boundary conditions ultimately prevent that. Hence, these solutions cannot form wave packages necessary to carry the Zeeman energy *away*.

### 5.3.2. In-plane modes

As for the out-of-plane vibrations above we start by transforming (5.2) to a first order ODE for a vector:

$$g_{xy}(x) := \begin{pmatrix} f_x(x) \\ f_x'(x) \\ f_y(x) \\ f_y'(x) \end{pmatrix}, \tag{5.14}$$

$$\Rightarrow g_{xy}'(x) = \begin{pmatrix} f_x'(x) \\ f_x''(x) \\ f_y'(x) \\ f_y''(x) \end{pmatrix} = \underbrace{\begin{pmatrix} 0 & 1 & 0 & 0 \\ \frac{\mu q^2-\rho\omega^2}{B+\mu} & 0 & 0 & \frac{-iBq}{B+\mu} \\ 0 & 0 & 0 & 1 \\ 0 & \frac{-iBq}{B+\mu} & \frac{(B+\mu)q^2-\rho\omega^2}{\mu} & 0 \end{pmatrix}}_{=:A} \begin{pmatrix} f_x(x) \\ f_x'(x) \\ f_y(x) \\ f_y'(x) \end{pmatrix} = Ag_{xy}(x)\,.$$

Here, we are interested in the first and the third component of $g_{xy}(x)$ as opposed to $g_\zeta(x)$ above, where we only need the first component. With theorem 2 of appendix B we keep track of all components. For the characteristic polynomial we find

$$\chi_A(\lambda) = \lambda^4 + \lambda^2\left(-2q^2 + \frac{\rho\omega^2}{B+\mu} + \frac{\rho\omega^2}{\mu}\right) + q^4 - \frac{q^2\rho\omega^2}{B+\mu} - \frac{q^2\rho\omega^2}{\mu} + \frac{\rho^2\omega^4}{(B+\mu)\mu}\,,$$

and its roots are

$$\lambda_1 = \sqrt{q^2 - \frac{\rho\omega^2}{B+\mu}}\,, \quad \lambda_2 = -\sqrt{q^2 - \frac{\rho\omega^2}{B+\mu}}\,, \quad \lambda_3 = \sqrt{q^2 - \frac{\rho\omega^2}{\mu}}\,, \quad \lambda_4 = -\sqrt{q^2 - \frac{\rho\omega^2}{\mu}}\,.$$

There are two special cases, $q = \pm\sqrt{\rho/\mu}\omega$ and $q = \pm\sqrt{\rho/(B+\mu)}\omega$ for which double roots occur. Again, we treat the more general case with single roots only first.

Then, the invertible matrix $S$ that transforms $A$ to its Jordan canonical form,

$$S^{-1}AS = \begin{pmatrix} \lambda_1 & 0 & 0 & 0 \\ 0 & \lambda_2 & 0 & 0 \\ 0 & 0 & \lambda_3 & 0 \\ 0 & 0 & 0 & \lambda_4 \end{pmatrix},$$

is given by

$$S = \begin{pmatrix} \frac{-i}{q} & \frac{-i}{q} & \frac{-iq}{\lambda_3^2} & \frac{-iq}{\lambda_4^2} \\ \frac{-i\lambda_1}{q} & \frac{-i\lambda_2}{q} & \frac{-iq}{\lambda_3} & \frac{-iq}{\lambda_4} \\ \frac{1}{\lambda_1} & \frac{1}{\lambda_2} & \frac{1}{\lambda_3} & \frac{1}{\lambda_4} \\ 1 & 1 & 1 & 1 \end{pmatrix}.$$

According to theorem 2 the fundamental system is

$$\left\{ \begin{pmatrix} \frac{-i}{q} \\ \frac{-i\lambda_1}{q} \\ \frac{1}{\lambda_1} \\ 1 \end{pmatrix} e^{\lambda_1 x}, \begin{pmatrix} \frac{-i}{q} \\ \frac{-i\lambda_2}{q} \\ \frac{1}{\lambda_2} \\ 1 \end{pmatrix} e^{\lambda_2 x}, \begin{pmatrix} \frac{-iq}{\lambda_3^2} \\ \frac{-iq}{\lambda_3} \\ \frac{1}{\lambda_3} \\ 1 \end{pmatrix} e^{\lambda_3 x}, \begin{pmatrix} \frac{-iq}{\lambda_4^2} \\ \frac{-iq}{\lambda_4} \\ \frac{1}{\lambda_4} \\ 1 \end{pmatrix} e^{\lambda_4 x} \right\}, \tag{5.15}$$

of which the first and third components constitute $f_x(x)$ and $f_y(x)$ (see (5.14)). For simplicity we divide each vector in (5.15) by its first components such that we get

$$\begin{aligned} f_x(x) &= c_1 e^{\lambda_1 x} + c_2 e^{\lambda_2 x} + c_3 e^{\lambda_3 x} + c_4 e^{\lambda_4 x}\,, \\ f_y(x) &= c_1 \frac{iq}{\lambda_1} e^{\lambda_1 x} + c_2 \frac{iq}{\lambda_2} e^{\lambda_2 x} + c_3 \frac{i\lambda_3}{q} e^{\lambda_3 x} + c_4 \frac{i\lambda_4}{q} e^{\lambda_4 x}\,. \end{aligned} \tag{5.16}$$

As for the out-of-plane modes, the coefficients $c_i$ are determined by the boundary conditions,

$$\begin{aligned} (5.9),\, x=0 \quad &\Rightarrow \quad c_1\left(\lambda_1 - \frac{\sigma q^2}{\lambda_1}\right) + c_2\left(\lambda_2 - \frac{\sigma q^2}{\lambda_2}\right) \\ &\quad + c_3\left(\lambda_3 - \sigma\lambda_3\right) + c_4\left(\lambda_4 - \sigma\lambda_4\right) = 0\,, \\ (5.9),\, x=W \quad &\Rightarrow \quad c_1\left(\lambda_1 - \frac{\sigma q^2}{\lambda_1}\right) e^{\lambda_1 W} + c_2\left(\lambda_2 - \frac{\sigma q^2}{\lambda_2}\right) e^{\lambda_2 W} \\ &\quad + c_3\left(\lambda_3 - \sigma\lambda_3\right) e^{\lambda_3 W} + c_4\left(\lambda_4 - \sigma\lambda_4\right) e^{\lambda_4 W} = 0\,, \\ (5.10),\, x=0 \quad &\Rightarrow \quad c_1(iq+iq) + c_2(iq+iq) \\ &\quad + c_3\left(\frac{i\lambda_3^2}{q} + iq\right) + c_4\left(\frac{i\lambda_4^2}{q} + iq\right) = 0\,, \\ (5.10),\, x=W \quad &\Rightarrow \quad c_1(iq+iq)e^{\lambda_1 W} + c_2(iq+iq)e^{\lambda_2 W} \\ &\quad + c_3\left(\frac{i\lambda_3^2}{q} + iq\right) e^{\lambda_3 W} + c_4\left(\frac{i\lambda_4^2}{q} + iq\right) e^{\lambda_4 W} = 0\,. \end{aligned}$$

We write these conditions in matrix form: $B(q,\omega)\cdot(c_1,c_2,c_3,c_4) = (0,0,0,0)$, where the matrix $B(q,\omega)$ is given by

$$\begin{pmatrix} \left(\lambda_1 - \frac{\sigma q^2}{\lambda_1}\right) & \left(\lambda_2 - \frac{\sigma q^2}{\lambda_2}\right) & \left(\lambda_3 - \sigma\lambda_3\right) & \left(\lambda_4 - \sigma\lambda_4\right) \\ \left(\lambda_1 - \frac{\sigma q^2}{\lambda_1}\right) e^{\lambda_1 W} & \left(\lambda_2 - \frac{\sigma q^2}{\lambda_2}\right) e^{\lambda_2 W} & \left(\lambda_3 - \sigma\lambda_3\right) e^{\lambda_3 W} & \left(\lambda_4 - \sigma\lambda_4\right) e^{\lambda_4 W} \\ (iq+iq) & (iq+iq) & \left(\frac{i\lambda_3^2}{q} + iq\right) & \left(\frac{i\lambda_4^2}{q} + iq\right) \\ (iq+iq)e^{\lambda_1 W} & (iq+iq)e^{\lambda_2 W} & \left(\frac{i\lambda_3^2}{q} + iq\right) e^{\lambda_3 W} & \left(\frac{i\lambda_4^2}{q} + iq\right) e^{\lambda_4 W} \end{pmatrix}.$$

We continue with the same procedure as for the out-of-plane vibrations. Roots $(q_0,\omega_0)$ of $\det B(q,\omega)$ (the dispersion) are plotted in figure 5.3 (a) and a typical in-plane vibration is shown if figure 5.3 (b). Again, the coefficients $c_i$ are determined but up to common constant.

For the special case with $q = \pm\sqrt{\rho/\mu}\,\omega$, the Matrix $S$ that transforms $A$ to its Jordan canonical form,

$$S^{-1}AS = \begin{pmatrix} 0 & 1 & 0 & 0 \\ 0 & 0 & 0 & 0 \\ 0 & 0 & \lambda_2 & 0 \\ 0 & 0 & 0 & \lambda_1 \end{pmatrix},$$

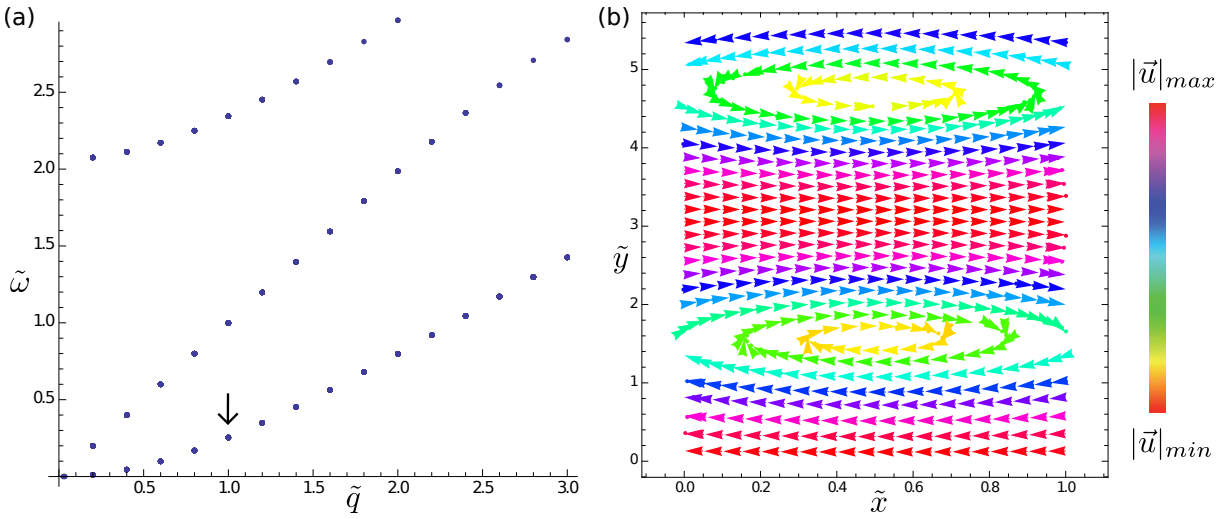


Figure 5.3.: (a) Plot of the dispersion. The arrow indicates the parameters for figure (b), where we plot the real part of the $\vec{u}(x, y, t = 0)$. This corresponds to the classical deformation of the ribbon. Color indicates the magnitude of the displacement. For the numerics, physical quantities are transformed to dimensionless quantities (indicated with " ˜ ") according to (5.20).

is given by

$$S = \begin{pmatrix} 1 & 0 & \frac{-i}{q} & \frac{-i}{q} \\ 0 & 1 & \frac{-i\lambda_2}{q} & \frac{-i\lambda_1}{q} \\ 0 & \frac{i}{q} & \frac{1}{\lambda_2} & \frac{1}{\lambda_1} \\ 0 & 0 & 1 & 1 \end{pmatrix} .$$

From the first and third component of the fundamental system

$$\left\{ \begin{pmatrix} 1 \\ 0 \\ 0 \\ 0 \end{pmatrix} , \left( \begin{pmatrix} 0 \\ 1 \\ \frac{i}{q} \\ 0 \end{pmatrix} + \begin{pmatrix} 1 \\ 0 \\ 0 \\ 0 \end{pmatrix} x \right) , \begin{pmatrix} \frac{-i}{q} \\ \frac{-i\lambda_2}{q} \\ \frac{1}{\lambda_2} \\ 1 \end{pmatrix} e^{\lambda_2 x} , \begin{pmatrix} \frac{-i}{q} \\ \frac{-i\lambda_1}{q} \\ \frac{1}{\lambda_1} \\ 1 \end{pmatrix} e^{\lambda_1 x} \right\}$$

we infer

$$\begin{aligned} f_x(x) &= c_1 + c_2 x + c_3 \frac{-i}{q} e^{\lambda_2 x} + c_4 \frac{-i}{q} e^{\lambda_1 x} , \\ f_y(x) &= c_2 \frac{i}{q} + c_3 \frac{1}{\lambda_2} e^{\lambda_2 x} + c_4 \frac{1}{\lambda_1} e^{\lambda_1 x} . \end{aligned}$$

The matrix containing the boundary conditions, $B(\omega)$, is now independent of $q$. Its determinant has two zeros but the boundary conditions can be satisfied only for discrete $q$ values such that there is no continuous dispersion. Consequently, these solutions cannot form wave packages that carry the Zeeman energy away such that we can neglect this special case. The same holds for the other special case, $q = \pm\sqrt{\rho/(B+\mu)}\omega$, that leads to a purely imaginary determinant with several discrete roots.

## 5.4. Properties of ribbon modes

In this section, we discuss the dispersion relations and vibrational modes obtained from the above solution. There is no experimental data on GNR but we can compare our results to carbon nanotubes and bulk graphene. We turn to the out-of-plane modes first and the in-plane modes are treated afterwards.

### 5.4.1. Out-of-plane modes

In order to generalize our theory and to ease calculations we transform to dimensionless quantities:

$$x \to \tilde{x} = \frac{x}{W}\,, \quad \lambda_i \to \tilde{\lambda}_i = \lambda_i W \quad (i \in \{1,2,3,4\})\,, \quad q \to \tilde{q} = qW\,, \qquad (5.17)$$
$$\omega \to \tilde{\omega} = \omega\sqrt{\frac{\rho}{\kappa}}W^2\,, \quad \kappa, \rho \to \tilde{\kappa}, \tilde{\rho} = 1$$

As a consequence, the width does not enter the calculations and we obtain scalable results. Concrete numbers for any ribbon width $W$ are recovered by undoing these substitutions:

$$\begin{aligned}
\omega &= \tilde{\omega}\sqrt{\frac{\kappa}{\rho}}\frac{1}{W^2}\,, \\
\lambda_1 &= \frac{\tilde{\lambda}_1}{W} = \frac{\sqrt{\tilde{q}^2 + \sqrt{\tilde{\omega}^2\frac{\tilde{\rho}}{\tilde{\kappa}}}}}{W} = \sqrt{\frac{\tilde{q}^2}{W^2} + \sqrt{\frac{\tilde{\omega}^2}{W^4}}} = \sqrt{q^2 + \sqrt{\frac{\omega^2\rho}{\kappa}}}\,. \quad \checkmark
\end{aligned}$$

The frequency, the energy and the magnetic field that relate to $\tilde{\omega}$ are

$$\begin{aligned}
\omega &= \tilde{\omega}\sqrt{\frac{\kappa}{\rho}}\frac{1}{W^2} = 6.80\times10^{11}\frac{\tilde{\omega}}{W[\,\mathrm{nm}]^2}\,\frac{1}{\mathrm{s}} = 2\pi\times 108\frac{\tilde{\omega}}{W[\,\mathrm{nm}]^2}\,\mathrm{GHz}\,, \\
E &= \hbar\omega = 4.48\times10^{-4}\frac{\tilde{\omega}}{W[\,\mathrm{nm}]^2}\,\mathrm{eV}\,, \\
B &= \frac{\hbar\omega}{g\mu_B} = 3.87\frac{\tilde{\omega}}{W[\,\mathrm{nm}]^2}\,\mathrm{T}\,, \qquad (5.18)
\end{aligned}$$

where $g = 2$ is the $g$-factor in graphene and $\mu_B$ is the Bohr magneton, [Zhang (2006)].

Both graphene lattice vectors have length $\sqrt{3}a$ (see figure 2.1) such that the Brillouin zone extends to $\pi/(\sqrt{3}a)$. From $q \le \pi/(\sqrt{3}a)$ we infer

$$\begin{aligned}
&\tilde{q} \le \frac{\pi}{\sqrt{3}a}W = \frac{\pi}{\sqrt{3}\times 1.42\,\text{Å}}W[\,\mathrm{nm}]\times10^{-9}\,\mathrm{m} = \frac{10\pi}{\sqrt{3}\times1.42}W[\,\mathrm{nm}] = 12.8W[\,\mathrm{nm}]\,, \\
\Rightarrow\quad &\tilde{q}_{30} \le 12.8\times30 = 384 \quad (\text{for } W = 30\,\mathrm{nm}). \qquad (5.19)
\end{aligned}$$

In figure 5.4 we plot the dispersion dot for dot, similar to figure 5.2 but with much smaller steps. Four different plots are shown with $\tilde{q} \in [0;50]$ on the largest scale. The continuum model is expected to yield good results at the center of the Brillouin zone where

wavelengths are large compared to the unit cell such that the atomic structure becomes negligible. Whether $\tilde{q} = 50$ corresponds to the zone center depends on the ribbon width, (5.19). For $W = 30\,\mathrm{nm}$ we do not attribute this value to the zone center. Obviously, there are distinct branches which correspond to excitations along the transverse ribbon direction (shown in figure 5.5). The lowest branch has a finite steepness at the origin. The linear behavior is confirmed by expanding $\det B(\alpha\tilde{q}, \alpha\tilde{\omega})$ into a series of $\alpha$. For infinitesimal deviations from the zone center only the lowest order is relevant. It has analytical roots for $\tilde{\omega} = 1.39\,\tilde{q}$. We infer that the finite width of the GNR leads to a cut-off mechanism at the zone center. The associated sound velocity is

$$v_\zeta(q=0) = \left.\frac{\mathrm{d}\omega}{\mathrm{d}q}\right|_{q=0} = \sqrt{\frac{\kappa}{\rho}}\frac{1}{W}\left.\frac{\mathrm{d}\tilde{\omega}}{\mathrm{d}\tilde{q}}\right|_{\tilde{q}=0} = \frac{945}{W[\,\mathrm{nm}]}\,\frac{\mathrm{m}}{\mathrm{s}}\,,$$

$$\Rightarrow \qquad v_{\zeta,30} = \frac{945}{30}\,\frac{\mathrm{m}}{\mathrm{s}} = 31.5\,\frac{\mathrm{m}}{\mathrm{s}}\,.$$

It increases inversely with ribbon width such that zero sound velocity is recovered for sufficiently large $W$, in agreement with previous results for bulk graphene. Away from the zone center all data points can be fitted with parabolas which matches the idea that the ribbon mimics bulk for wavelengths small compared to the ribbon width.

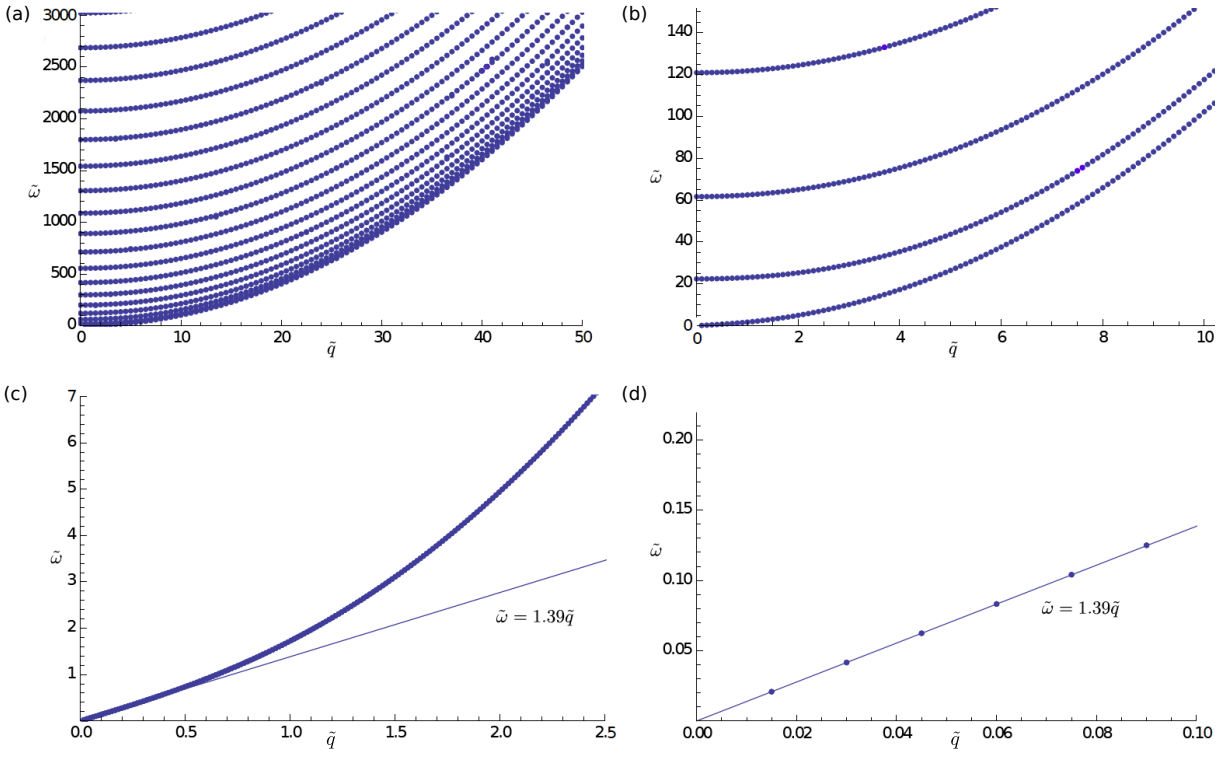


Figure 5.4.: (a)-(d): The dispersion of the out-of-plane modes on four different scales. Figures (c) and (d) highlight the linear dispersion of the lowest branch at the zone center, which we confirm analytically (indicated by the line).

For a ribbon of length $L$, possible wavenumbers are $q = \pm 2\pi/L, \pm 4\pi L, \ldots, \pm 2n\pi/L$ ($n \in \mathbb{N}$). That is, the density of states in $q$-space is $D(q) = \mathrm{d}N/\mathrm{d}q = 2/(2\pi/L) = L/\pi$,

where $N$ is the absolute number of possible phonon states. With $D(\omega)\mathrm{d}\omega = \mathrm{d}N = D(q)\mathrm{d}q$ we derive the density in $\omega$-space,

$$D(\omega) = D(q)\frac{\mathrm{d}q}{\mathrm{d}\omega}\bigg|_{\omega} = \frac{L}{\pi\,\mathrm{d}\omega/\mathrm{d}q|_{\omega}} = \sqrt{\frac{\rho}{\kappa}}\frac{LW}{\pi\,\mathrm{d}\tilde{\omega}/\mathrm{d}\tilde{q}|_{\tilde{\omega}}}\,.$$

By virtue of polynomial fits and the above formula we obtain the density of states for each branch in the dispersion. In figure 5.6, we plot the sum of all branches up to $\tilde{\omega} = 125$, corresponding to $B = 0.5\,\mathrm{T}$ for $W = 30\,\mathrm{nm}$, (5.18). The flat dispersion of higher transverse modes leads to a divergent density of states where said modes become accessible. In contrast, the non-zero sound velocity of the lowest branch leads to a finite density of states at zero frequency, namely $D(\omega = 0) = 10.1 \times 10^{-9}s$ (for $L = 1\,\mu\mathrm{m}$, $W = 30\,\mathrm{nm}$), corresponding to $D(E = 0) = 15.3/\,\mu\mathrm{eV}$.

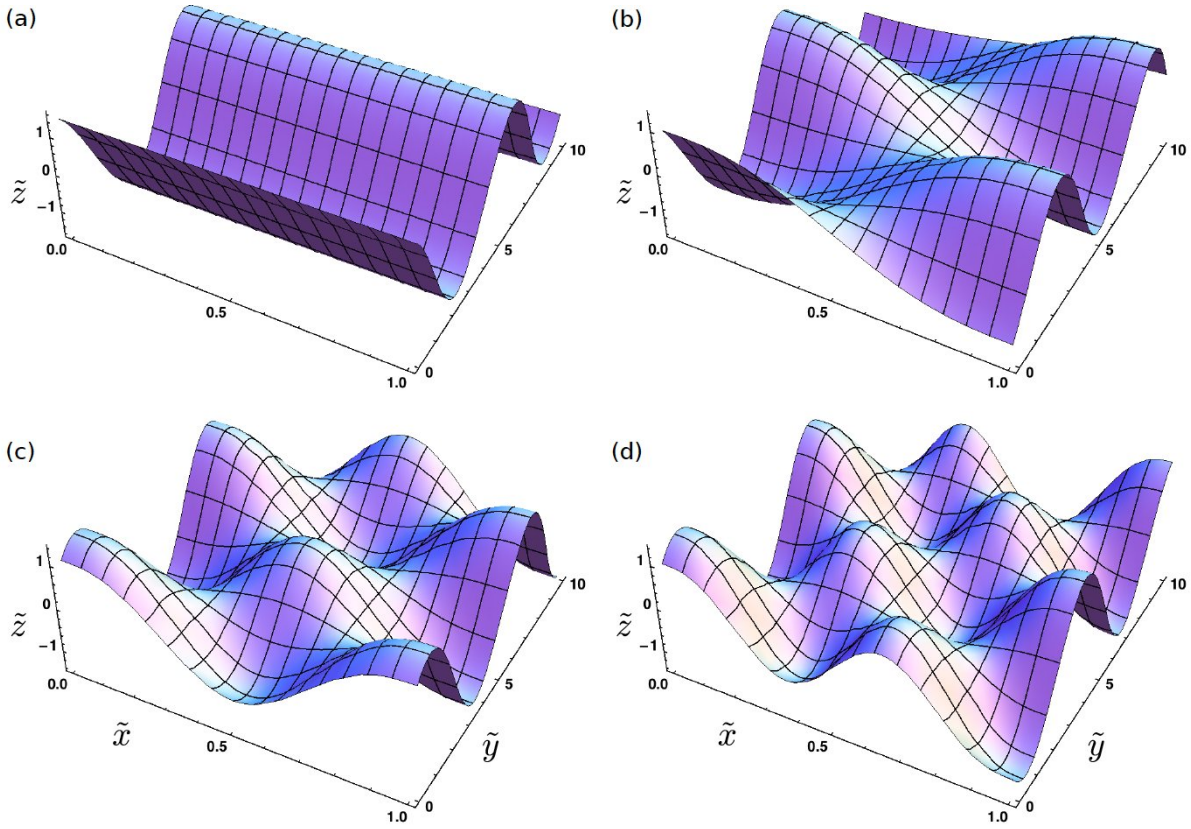


Figure 5.5.: (a)-(d): These plots correspond to the four lowest transverse excitations (as in figure 5.4 (b)) at $\tilde{q} = 1$.

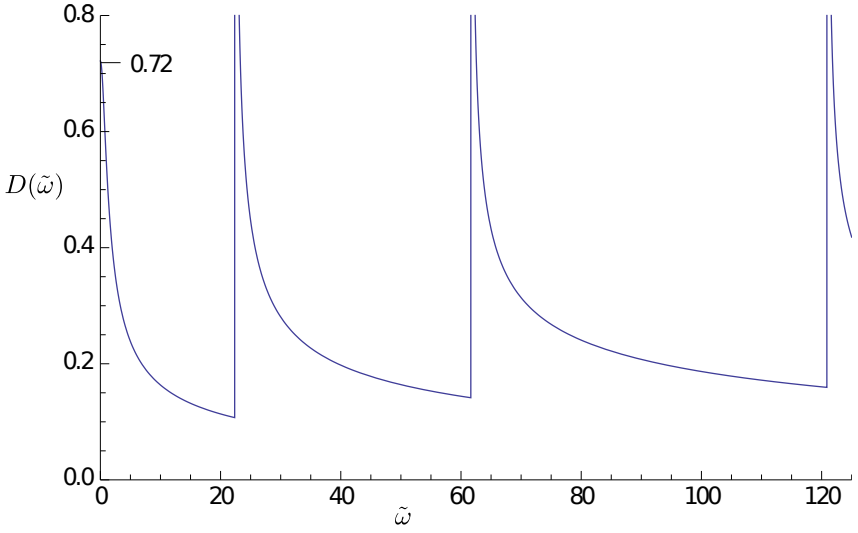


Figure 5.6.: The finite sound velocity of the out-of-plane mode at zero energy leads to a non-divergent density of states. Higher transverse excitations begin flat, however, thus causing the density of states to diverge at these energies.

### 5.4.2. In-plane vibrations

As for the out-of-plane modes, we generalize our calculations by transforming to dimensionless quantities:

$$x \to \tilde{x} = \frac{x}{W}\,, \quad \lambda_i \to \tilde{\lambda}_i = \lambda_i W \quad (i \in \{1,2,3,4\})\,, \quad q \to \tilde{q} = qW\,, \tag{5.20}$$
$$\omega \to \tilde{\omega} = \omega\sqrt{\frac{\rho}{\mathcal{E}h}}W\,, \quad \rho \to \tilde{\rho} = 1\,, \quad \mu \to \tilde{\mu} = \frac{\mu}{\mathcal{E}h}\,, \quad B \to \tilde{B} = \frac{B}{\mathcal{E}h}\,.$$

The substitutions can be undone via

$$\omega = \tilde{\omega}\sqrt{\frac{\mathcal{E}h}{\rho}}\frac{1}{W}\,, \tag{5.21}$$
$$\lambda_1 = \frac{\tilde{\lambda}_1}{W} = \frac{\sqrt{\tilde{q}^2 - \frac{\tilde{\rho}\tilde{\omega}^2}{\tilde{B}+\tilde{\mu}}}}{W} = \sqrt{\frac{\tilde{q}^2}{W^2} - \frac{\tilde{\omega}^2\mathcal{E}h}{(B+\mu)W^2}} = \sqrt{q^2 - \frac{\rho\omega^2}{B+\mu}}\,. \quad \checkmark$$

The frequency, the energy and the magnetic field corresponding to $\tilde{\omega}$ are calculated via

$$\omega = \tilde{\omega}\sqrt{\frac{\mathcal{E}h}{\rho}}\frac{1}{W} = 2.99\times10^{13}\frac{\tilde{\omega}}{W[\,\mathrm{nm}]}\,\frac{1}{\mathrm{s}} = 2\pi\times4.76\frac{\tilde{\omega}}{W[\,\mathrm{nm}]}\,\mathrm{THz}\,,$$
$$E = \hbar\omega = 1.97\times10^{-2}\frac{\tilde{\omega}}{W[\,\mathrm{nm}]}\,\mathrm{eV}\,,$$
$$B = \frac{\hbar\omega}{g\mu_B} = 1.70\times10^{2}\frac{\tilde{\omega}}{W[\,\mathrm{nm}]}\,\mathrm{T}\,. \tag{5.22}$$

Equation (5.19) and following remarks hold here, as well. Figure 5.7 shows the dispersion of in-plane modes on different scales. There are infinitely many branches originating from

different values $\tilde{\omega}$. For large $\tilde{q}$, all of them converge against a common linear line (green line in figure 5.7 (a)). Our interpretation is that $\tilde{\omega}(\tilde{q} = 0)$ is associated with an excitation that becomes negligible for large $\tilde{q}$, thus explaining the asymptotic behavior. An exception are the two lowest branches which originate from $\tilde{\omega} = 0$ and form a line slightly below said asymptote.

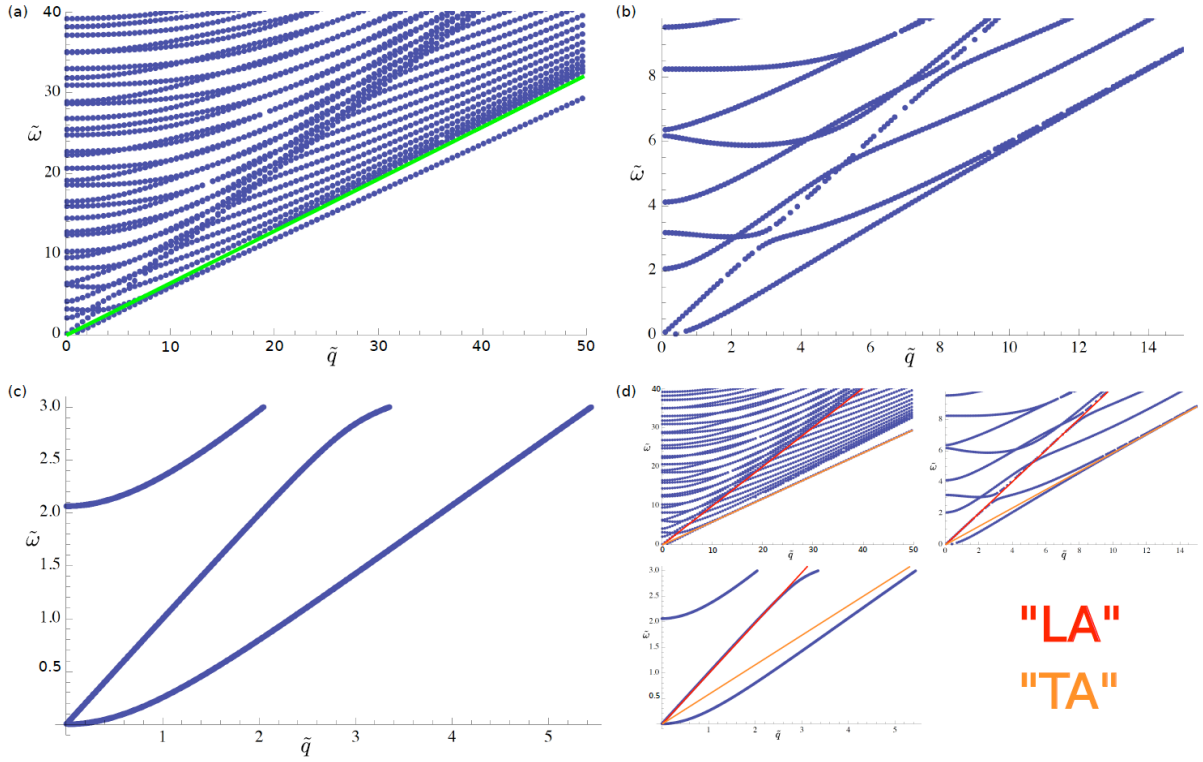


Figure 5.7.: (a)-(c): The dispersion of the out-of-plane modes on three different scales. For large wavenumbers, all but the two lowest modes converge against the green line indicated in (a). We also identify lines in the dispersion (indicated in (d)), where the modes are of predominantly transverse / longitudinal character ("TA" / "LA").

Another feature are the two lines indicated in figure 5.7 (d). For $\tilde{q} > 10$, the shallower line is constituted by the two lowest branches. One of those branches supports the steeper line up to $\tilde{q} \approx 3$, from where it transitions to the shallower line. The steeper line is supported piecewise by different branches. For example from $\tilde{q} \approx 3$, where said transition occurs, up to $\tilde{q} \approx 8$ it is constituted by the branch originating from $\tilde{\omega} \approx 3.1$ and so on. From the vector fields in figure 5.8 it appears that mainly transverse displacements occur on the shallower line such that we associate it with the transverse acoustical mode in bulk ("TA"). Modes that contribute to the steeper line feature mainly longitudinal displacements in the supporting interval. Accordingly, we relate the steeper line with the longitudinal acoustical bulk mode ("LA"). Pure longitudinal or transverse modes do not occur, however, since the ribbon boundaries always lead to a coupling.

To check our interpretation, we calculate the sound velocities $v = \mathrm{d}\omega/\mathrm{d}q$ corresponding to the "LA" and "TA" lines and compare them with literature values for bulk graphene

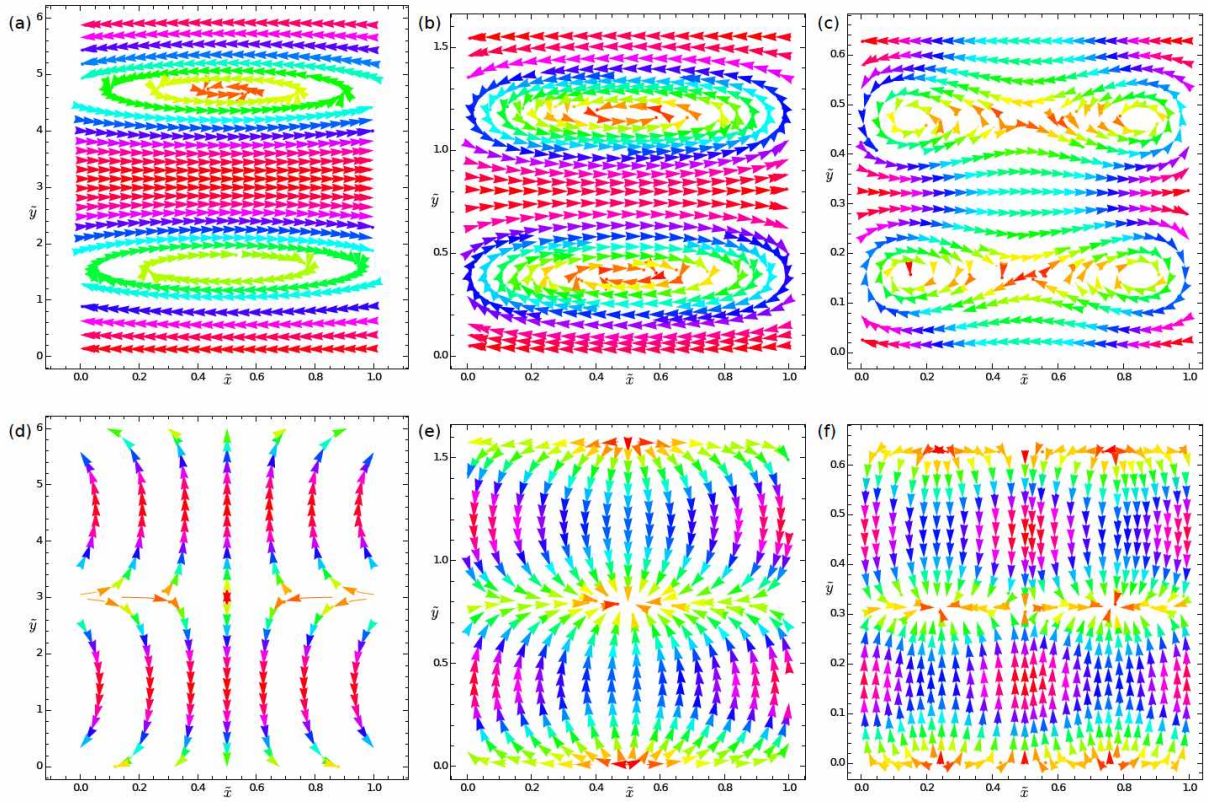


Figure 5.8.: We plot vibrations with predominant transverse / longitudinal character for different wavenumbers. Figures (a) - (c) correspond to transverse modes and (d) - (f) to longitudianl modes. The wavenumbers are $\tilde{q} = 1$ for (a) and (d), $\tilde{q} = 4$ for (b) and (e) and $\tilde{q} = 9$ for (c) and (f). As in figure 5.3, color indicates the magnitude of the displacement.

and carbon nanotubes, see table 5.2. Although these systems are different, we expect matchable results due to the same underlying atomistic structure. Since both $\omega$ and $q$ go inversely with $W$, the in-plane sound velocities are independent of the ribbon width. We also point out that $\omega$ and hence $v$ is proportional to $\sqrt{\mathcal{E}h}$, see (5.21). In section 5.1 we have already mentioned that these elastic constants have not been settled, yet. Therefore we calculate both sound velocities for $\mathcal{E}h = 3.4\,\mathrm{TPa\,Å}$ (the choice we made in 5.1) and for $\mathcal{E}h = 1.7\,\mathrm{TPa\,Å}$ (as can be inferred from [Frank (2007)]).

In analogy to the out-of-plane modes, the density of states is obtained via

$$D(\omega) = D(q)\frac{\mathrm{d}q}{\mathrm{d}\omega}\bigg|_{\omega} = \frac{L}{\pi\,\mathrm{d}\omega/\mathrm{d}q|_{\omega}} = \sqrt{\frac{\rho}{\mathcal{E}h}}\frac{L}{\pi\,\mathrm{d}\tilde{\omega}/\mathrm{d}\tilde{q}|_{\tilde{\omega}}} \tag{5.23}$$

and polynomial fits to the branches in the dispersion. In figure 5.9, we plot $D(\tilde{\omega})$ up to $\tilde{\omega} = 3.0$, corresponding to a magnetic field of 17 T for $W = 30\,\mathrm{nm}$, (5.22). A magnetic field as we used it for the out-of-plane modes ($B = 0.5\,\mathrm{T}$) relates to a much smaller $\tilde{\omega} \approx 0.1$. The flat dispersion of the lowest branch leads to a divergent density of states at zero energy, figure 5.9.

| | | | |
|---|---|---|---|
| $v_{TA} = 19.1\,\mathrm{km/s}$ | $v_{LA} = 29.6\,\mathrm{km/s}$ | $v_{LA}/v_{TA} = 1.55$ | $\mathcal{E}h = 3.4\,\mathrm{TPa\,Å}$ |
| $v_{TA} = 13.5\,\mathrm{km/s}$ | $v_{LA} = 20.9\,\mathrm{km/s}$ | $v_{LA}/v_{TA} = 1.55$ | $\mathcal{E}h = 1.7\,\mathrm{TPa\,Å}$ |
| $v_{TA} = 12.2\,\mathrm{km/s}$ | $v_{LA} = 19.5\,\mathrm{km/s}$ | $v_{LA}/v_{TA} = 1.60$ | [Falkovsky (2008)] |
| $v_{TA} = 14\,\mathrm{km/s}$ | $v_{LA} = 24\,\mathrm{km/s}$ | $v_{LA}/v_{TA} = 1.7$ | [Sánchez-Portal (1999)] |

Table 5.2.: We compare the sound velocities indicated in figure 5.7 (d) with previous values for bulk graphene ([Falkovsky (2008)], symmetry arguments) and carbon nanotubes ([Sánchez-Portal (1999)], density functional theory). For $\mathcal{E}h = 3.4\,\mathrm{TPa\,Å}$, our results lie above these values but are of the same order. For $\mathcal{E}h = 1.7\,\mathrm{TPa\,Å}$, previous values match well with our results. The ratio $v_{LA}/v_{TA}$ is independent of $\mathcal{E}h$ and agrees with cited values.

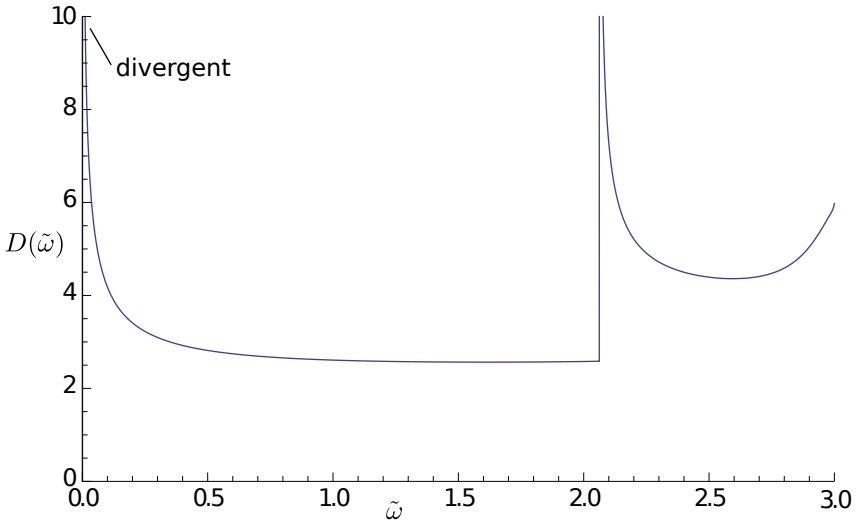


Figure 5.9.: The density of states of the in-plane modes diverges at zero energy, in contrast to the out-of-plane modes. Further divergences occur at energies where the dispersion is flat (figure 5.7).

# 6. Electron-phonon coupling

There are several mechanisms that lead to electron-phonon coupling, including piezoelectric electron-phonon interaction, bond length change and the deformation potential [Yu & Cardona, Suzuura (2002)]. While the first mechanism does play a role for GaAs QD [Khaetskii (2001)], it does not occur in graphene where the unbiased unit cell does not allow for piezo effects. The other two mechanism are expected to contribute to spin relaxation via the admixture mechanism. For simplicity, we focus on the deformation potential to which only in-plane modes contribute in lowest order.

First, we normalize the classical in-plane vibrations of the previous chapter. From these orthonormal modes we establish the field theory for ribbon phonons with phonon creation and annihilation operators. We also derive the deformation potential and express it in terms of said phonon operators to obtain an electron-phonon coupling hamiltonian.

## 6.1. Mode orthonormality

We specify ribbon modes via $(\alpha, q)$, where $\alpha$ labels dispersion branches and $q$ the wavenumber. As mentioned in section 5.3, the coefficients $c_i^{(\alpha,q)}$ are determined up to a common constant. Classically, this constant can have any value. MATHEMATICA provides definite output by normalizing the vector $(c_1, c_2, c_3, c_4)^{(\alpha,q)}$ to unity. From this output we calculate the real quantity

$$N^{(\alpha,q)} := \sqrt{\frac{1}{W}\int_0^W \left( f_x^{(\alpha,q)}(x) \left( f_x^{(\alpha,q)}(x) \right)^* + f_y^{(\alpha,q)}(x) \left( f_y^{(\alpha,q)}(x) \right)^* \right) \mathrm{d}x} \,. \tag{6.1}$$

With this definition, functions $f_{x,y}^{(\alpha,q)}(x)/N^{(\alpha,q)}$ satisfy the orthonormality relation that we require for a phonon field theory,

$$\frac{1}{W}\int_0^W \left( \frac{f_x^{(\alpha,q)}(x)}{N^{(\alpha,q)}} \left( \frac{f_x^{(\beta,q)}(x)}{N^{(\beta,q)}} \right)^* + \frac{f_y^{(\alpha,q)}(x)}{N^{(\alpha,q)}} \left( \frac{f_y^{(\beta,q)}(x)}{N^{(\beta,q)}} \right)^* \right) \mathrm{d}x = \delta_{\alpha,\beta} \,. \tag{6.2}$$

While the normalization is obvious from the definition of $N^{(\alpha,q)}$, orthogonality is an inherent property of ODE (5.6) that even holds for both solitary summands but is not further discussed here. We also point out the behavior under complex conjugation,

$$\left( f_{x,y}^{(\alpha,q)}(x) \right)^* = f_{x,y}^{(\alpha,-q)}(x) \,. \tag{6.3}$$

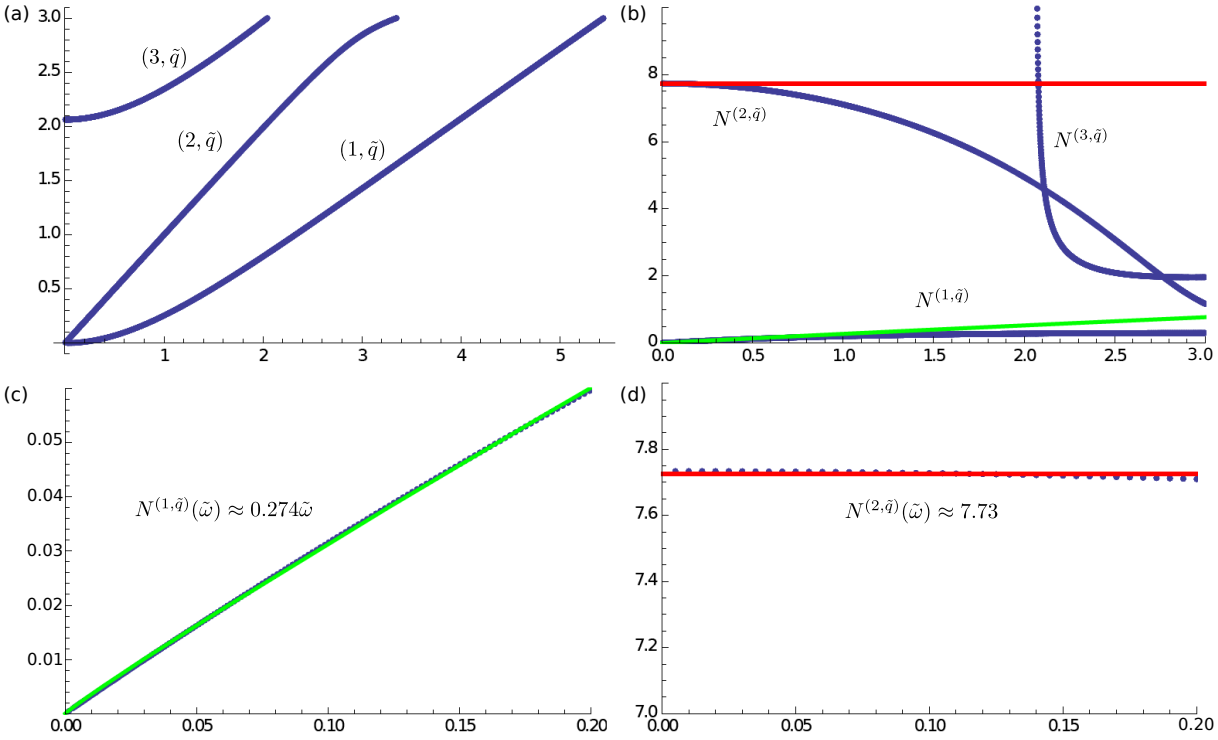


Figure 6.1.: (a) Only the two lowest phonon branches are available for conventional magnetic fields ($B \propto \tilde{\omega}$, $B = 1T \Rightarrow \tilde{\omega} = 0.18$ for $W = 30\,\mathrm{nm}$). (b) The numerically found normalizations (6.1) for the branches in (a). Fits of $N^{(1,\tilde{q})}(\tilde{\omega})$ and $N^{(2,\tilde{q})}(\tilde{\omega})$ for $\tilde{\omega} \in [0; 0.2]$ are shown in (c) and (d).

According to (5.22), a possible $\tilde{\omega}$-dependence of $N^{(\alpha,\tilde{q})}$ translates into a $B$-dependence that might influence the spin relaxation rate. Figure 6.1 shows $N^{(\alpha,\tilde{q})}(\tilde{\omega})$ for the three lowest branches up to[1] $\tilde{\omega} = 3$. Only the two lowest branches will be relevant as $\tilde{\omega} \approx 0.2$ for $W = 30\,\mathrm{nm}$ and $B \approx 1\,\mathrm{T}$. We fit both branches in the interval $\tilde{\omega} \in [0; 0.2]$, $N^{(1,\tilde{q})}(\tilde{\omega})$ with the power law $a\tilde{\omega}^b$ and $N^{(2,\tilde{q})}(\tilde{\omega})$ with a constant:

$$\begin{aligned} N^{(1,\tilde{q})}(\tilde{\omega}) &\approx 0.274\,\tilde{\omega}\,, \\ N^{(2,\tilde{q})}(\tilde{\omega}) &\approx 7.73\,. \end{aligned} \tag{6.4}$$

To check these results with a discrete example we consider $\tilde{\omega} = 0.18$ ($B = 1\,\mathrm{T}$ for $W = 30\,\mathrm{nm}$). The modes for this parameter are ($\alpha = 1, \tilde{q} = 0.83$) and ($\alpha = 2, \tilde{q} = 0.18$). By

[1] Where $\tilde{\omega} = \tilde{\omega}(\tilde{q})$ is a monotone function of $\tilde{q}$ we can plot $N^{(\alpha,\tilde{q})}$ with respect to its $\tilde{\omega}$-dependence: $N^{(\alpha,\tilde{q})} = N^{(\alpha,\tilde{q}(\tilde{\omega}))} = N^{(\alpha,\tilde{q})}(\tilde{\omega})$. All three branches shown in figure 6.1 are monotone in this interval.

normalizing both modes with the above fits, the integrals (6.2) become

$$\begin{aligned}
\int_0^{\tilde{W}=1} \left( \frac{f_x^{(1,0.83)}(\tilde{x})}{N^{(1,0.83)}} \left( \frac{f_x^{(1,0.83)}(\tilde{x})}{N^{(1,0.83)}} \right)^* + \frac{f_y^{(1,0.83)}(\tilde{x})}{N^{(1,0.83)}} \left( \frac{f_y^{(1,0.83)}(\tilde{x})}{N^{(1,0.83)}} \right)^* \right) \mathrm{d}\tilde{x} &= 0.995 \approx 1\,, \quad \checkmark \\
\int_0^{\tilde{W}=1} \left( \frac{f_x^{(2,0.18)}(\tilde{x})}{N^{(2,0.18)}} \left( \frac{f_x^{(2,0.18)}(\tilde{x})}{N^{(2,0.18)}} \right)^* + \frac{f_y^{(2,0.18)}(\tilde{x})}{N^{(2,0.18)}} \left( \frac{f_y^{(2,0.18)}(\tilde{x})}{N^{(2,0.18)}} \right)^* \right) \mathrm{d}\tilde{x} &= 0.997 \approx 1\,. \quad \checkmark \\
\int_0^{\tilde{W}=1} \left( \frac{f_x^{(1,0.83)}(\tilde{x})}{N^{(1,0.83)}} \left( \frac{f_x^{(2,0.18)}(\tilde{x})}{N^{(2,0.18)}} \right)^* + \frac{f_y^{(1,0.83)}(\tilde{x})}{N^{(1,0.83)}} \left( \frac{f_y^{(2,0.18)}(\tilde{x})}{N^{(2,0.18)}} \right)^* \right) \mathrm{d}\tilde{x} &= 0\,. \quad \checkmark
\end{aligned}$$

For simplicity, we absorb the normalization in the functions from now on:

$$f_{x,y;N}^{(\alpha,q)}(x) := f_{x,y}^{(\alpha,q)}(x)/N^{(\alpha,q)} \to f_{x,y}^{(\alpha,q)}(x)\,. \tag{6.5}$$

## 6.2. Phonon field theory

Here, we present how to quantize the classical in-plane modes of chapter 5. We follow the field theory as described in standard textbooks [Rössler, Nolting 7]. Where absolutely necessary we disambiguate operators from scalars via " ˆ ", e. g. in $r_{\alpha,q} \to \hat{r}_{\alpha,q}$, but in general the character of a quantity will be clear from its context and we use no special notation for operators.

### 6.2.1. Normal coordinates

From the explicit representation of mode $(\alpha, q)$,

$$(u_x^{(\alpha,q)}, u_y^{(\alpha,q)})(x,y,t) = \left( f_x^{(\alpha,q)}(x)\vec{e}_x + f_y^{(\alpha,q)}(x)\vec{e}_y \right) e^{i(qy-\omega t)}\,,$$

we construct the general in-plane ribbon vibration $\vec{S} = (S_x, S_y)$ as a linear combination of all possible in-plane modes:

$$\begin{aligned}
\vec{S}(x,y,t) &= \sum_{\alpha,q} \tilde{r}_{\alpha,q} \left( f_x^{(\alpha,q)}(x)\vec{e}_x + f_y^{(\alpha,q)}(x)\vec{e}_y \right) e^{i(qy-\omega t)} \\
&= \sum_{\alpha,q} r_{\alpha,q}(t) \left( f_x^{(\alpha,q)}(x)\vec{e}_x + f_y^{(\alpha,q)}(x)\vec{e}_y \right) e^{iqy}\,.
\end{aligned} \tag{6.6}$$

In the second step, the time-dependence is absorbed in the amplitude, $r_{\alpha,q} = \tilde{r}_{\alpha,q} e^{-i\omega t}$, such that it satisfies the equation of motion of the simple harmonic oscillator,

$$\ddot{r}_{\alpha,q}(t) + \omega_{\alpha,q}^2 r_{\alpha,q}(t) = 0\,. \tag{6.7}$$

We multiply (6.6) by $e^{-iq'y}/L$ and integrate the $y$-coordinate,

$$\begin{aligned}\int_{-L/2}^{L/2} \frac{\vec{S}(x,y,t)e^{-iq'y}}{L}\,\mathrm{d}y &= \sum_{\alpha,q} r_{\alpha,q}(t)\left(f_x^{(\alpha,q)}(x)\vec{e}_x + f_y^{(\alpha,q)}(x)\vec{e}_y\right)\underbrace{\int_{-L/2}^{L/2}\frac{e^{i(q-q')y}}{L}\,\mathrm{d}y}_{=\delta_{q,q'}} \\ &= \sum_{\alpha} r_{\alpha,q'}(t)\left(f_x^{(\alpha,q')}(x)\vec{e}_x + f_y^{(\alpha,q')}(x)\vec{e}_y\right).\end{aligned}$$

After multiplication with $(f_x^{(\beta,q')}(x)\vec{e}_x + f_y^{(\beta,q')}(x)\vec{e}_y)^*$, we integrate the $x$-coordinate. With (6.2), (6.3) and (6.5) we find

$$\begin{aligned}&\int_0^W \int_{-L/2}^{L/2} \frac{(S_x(x,y,t)f_x^{(\beta,-q')}(x) + S_y(x,y,t)f_y^{(\beta,-q')}(x))e^{-iq'y}}{L}\,\mathrm{d}y\,\mathrm{d}x \\ &\quad= \sum_{\alpha} r_{\alpha,q'}(t)\underbrace{\int_0^W \left(f_x^{(\alpha,q')}(x)\left(f_x^{(\beta,q')}(x)\right)^* + f_y^{(\alpha,q')}(x)\left(f_y^{(\beta,q')}(x)\right)^*\right)\mathrm{d}x}_{=W\delta_{\alpha,\beta}} \\ &\quad= W r_{\beta,q'}(t).\end{aligned}$$

Now, the explicit form of the *normal coordinate* can be resolved:

$$\begin{aligned}r_{\alpha,q}(t) &= \int_0^W \int_{-L/2}^{L/2} \frac{(S_x(x,y,t)f_x^{(\alpha,-q)}(x) + S_y(x,y,t)f_y^{(\alpha,-q)}(x))e^{-iqy}}{LW}\,\mathrm{d}y\,\mathrm{d}x \\ &= \int_0^W \int_{-L/2}^{L/2} \frac{\vec{S}(x,y,t)\cdot\left(\vec{u}^{(\alpha,q)}(x,y,0)\right)^*}{LW}\,\mathrm{d}y\,\mathrm{d}x.\end{aligned}$$

The kinetic energy of the ribbon is given by the integral of its velocities and can be expressed in terms of normal coordinates:

$$\begin{aligned}\mathcal{T} &= \frac{\rho}{2}\int_0^W \int_{-L/2}^{L/2} \left|\dot{\vec{S}}(x,y,t)\right|^2 \mathrm{d}x\,\mathrm{d}y = \\ &= \frac{\rho}{2}\int_0^W \int_{-L/2}^{L/2} \sum_{\substack{\alpha,\,q\\ \beta,\,q'}} \dot{r}_{\alpha,q}\dot{r}^*_{\beta,q'} \underbrace{\left(f_x^{(\alpha,q)}\left(f_x^{(\beta,q')}\right)^* + f_y^{(\alpha,q)}\left(f_y^{(\beta,-q')}\right)^*\right)e^{i(q-q')y}}_{\Rightarrow LW\delta_{\alpha,\beta}\delta_{q,q'}}\mathrm{d}y\,\mathrm{d}x \\ &= \frac{\rho LW}{2}\sum_{\alpha,q}\left|\dot{r}_{\alpha,q}(t)\right|^2.\end{aligned}$$

An analog form for the potential energy[2] $\mathcal{V}$ leads to the lagrangian

$$\mathcal{L} = \mathcal{T} - \mathcal{V} = \frac{\rho LW}{2}\sum_{\alpha,q}\left(\dot{r}_{\alpha,q}(t)\dot{r}^*_{\alpha,q}(t) - \omega^2_{\alpha,q}r_{\alpha,q}(t)r^*_{\alpha,q}(t)\right).$$

[2]The potential energy is obtained straightforward via atomic force constants (connecting "springs"). Although perfectly justified for a graphene ribbon, this ansatz is different from the continuum model and consequently we do not show it here. The interested reader may refer to standard textbooks.

We infer the canonical momentum

$$p_{\alpha,q}(t) = \frac{\partial \mathcal{L}}{\partial \dot{r}_{\alpha,q}(t)} = \rho LW\, \dot{r}^*_{\alpha,q}(t)$$

and the hamiltonian of the simple harmonic oscillator,

$$\begin{aligned}
\mathcal{H} &= \sum_{\alpha,q} p_{\alpha,q}(t)\dot{r}_{\alpha,q}(t) - \mathcal{L} \\
&= \sum_{\alpha,q} \left( \frac{p_{\alpha,q}(t)p^*_{\alpha,q}(t)}{\rho LW} - \left( \frac{p_{\alpha,q}(t)p^*_{\alpha,q}(t)}{2\rho\, LW} - \frac{\rho\, LW\, \omega^2_{\alpha,q} r_{\alpha,q}(t) r^*_{\alpha,q}(t)}{2} \right) \right) \\
&= \sum_{\alpha,q} \left( \frac{|p_{\alpha,q}(t)|^2}{2\,\rho LW} + \omega^2_{\alpha,q} \frac{\rho LW\, |r_{\alpha,q}(t)|^2}{2} \right) , \qquad (6.8)
\end{aligned}$$

in accordance with (6.7).

## 6.2.2. Second quantization

We obtain a quantized system by promoting the normal coordinates and their canonical momenta to operators,

$$r_{\alpha,q}(t) \to \hat{r}_{\alpha,q}(t)\,, \quad p_{\alpha,q}(t) \to \hat{p}_{\alpha,q}(t)\,,$$

and imposing the commutators (we drop the " ˆ " from the operators)

$$\begin{aligned}
&[r_{\alpha,q}(t), r_{\beta,q'}(t)] = 0\,, \\
&[p_{\alpha,q}(t), p_{\beta,q'}(t)] = 0\,, \\
&[r_{\alpha,q}(t), p_{\beta,q'}(t)] = i\hbar\delta_{\alpha,\beta}\delta_{q,q'}\,.
\end{aligned} \qquad (6.9)$$

It is common to introduce phonon creation and annihilation operators,

$b^\dagger_{\alpha,q}(t)$ : creates a phonon of mode $\alpha$ with wavenumber $q$,
$b_{\alpha,q}(t)$ : annihilates a phonon of mode $\alpha$ with wavenumber $q$,

that satisfy

$$\begin{aligned}
&[b_{\alpha,q}(t), b_{\beta,q'}(t)] = 0\,, \\
&\left[b^\dagger_{\alpha,q}(t), b^\dagger_{\beta,q'}(t)\right] = 0\,, \\
&\left[b_{\alpha,q}(t), b^\dagger_{\beta,q'}(t)\right] = \delta_{\alpha,\beta}\delta_{q,q'}\,.
\end{aligned}$$

The allocations

$$\begin{aligned}
r_{\alpha,q}(t) &= \sqrt{\frac{\hbar}{2\,\rho LW\,\omega_{\alpha,q}}} \left( b_{\alpha,q}(t) + b^\dagger_{\alpha,-q}(t) \right) , \qquad (6.10) \\
p_{\alpha,q}(t) &= i\sqrt{\frac{\hbar\,\rho LW\,\omega_{\alpha,q}}{2}} \left( b^\dagger_{\alpha,q}(t) - b_{\alpha,-q(t)} \right)
\end{aligned}$$

comply with (6.9), we explicitly demonstrate the third relation:

$$\begin{aligned}
[r_{\alpha,q}(t), p_{\beta,q'}(t)] &= \sqrt{\frac{\hbar}{2\,\rho LW\,\omega_{\alpha,q}}} i \sqrt{\frac{\hbar\,\rho LW\,\omega_{\beta,q'}}{2}} \left[ b_{\alpha,q}(t) + b^\dagger_{\alpha,-q}(t), b^\dagger_{\beta,q'}(t) - b_{\beta,-q'}(t) \right] \\
&= \frac{i\hbar}{2} \sqrt{\frac{\omega_{\beta,q'}}{\omega_{\alpha,q}}} \Big( [b_{\alpha,q}(t), b^\dagger_{\beta,q'}(t)] - [b_{\alpha,q}(t), b_{\beta,-q'}(t)] \\
&\qquad + [b^\dagger_{\alpha,-q}(t), b^\dagger_{\beta,q'}(t)] - [b^\dagger_{\alpha,-q}(t), b_{\beta,-q'}(t)] \Big) \\
&= \frac{i\hbar}{2} \sqrt{\frac{\omega_{\beta,q'}}{\omega_{\alpha,q}}} \left( \delta_{\alpha,\beta}\delta_{q,q'} - 0 + 0 - (-\delta_{\alpha,\beta}\delta_{q,q'}) \right) = i\hbar\delta_{\alpha,\beta}\delta_{q,q'} \,. \quad \checkmark
\end{aligned}$$

With $r_{\alpha,q} \to \hat{r}_{\alpha,q}$, $r^*_{\alpha,q} \to \hat{r}^\dagger_{\alpha,q}$ and $p_{\alpha,q} \to \hat{p}_{\alpha,q}$, $p^*_{\alpha,q} \to \hat{p}^\dagger_{\alpha,q}$, hamiltonian (6.8) becomes a diagonal operator in occupation number representation:

$$\begin{aligned}
\mathcal{H} &= \sum_{\alpha,q} \frac{1}{2} \left( \frac{p^\dagger_{\alpha,q} p_{\alpha,q}}{2\,\rho LW} + \omega^2_{\alpha,q} \frac{\rho LW r^\dagger_{\alpha,q} r_{\alpha,q}}{2} \right) \\
&= \sum_{\alpha,q} \frac{1}{2} \left( \frac{\hbar\omega_{\alpha,q}}{2} (b_{\alpha,q} - b^\dagger_{\alpha,-q})(b^\dagger_{\alpha,q} - b_{\alpha,-q}) + \frac{\hbar\omega_{\alpha,q}}{2} (b^\dagger_{\alpha,q} + b_{\alpha,-q})(b_{\alpha,q} + b^\dagger_{\alpha,-q}) \right) \\
&\overset{(*)}{=} \sum_{\alpha,q} \frac{\hbar\omega_{\alpha,q}}{4} \Big( b_{\alpha,q} b^\dagger_{\alpha,q} - b_{\alpha,q} b_{\alpha,-q} - b^\dagger_{\alpha,q} b^\dagger_{\alpha,-q} + b^\dagger_{\alpha,q} b_{\alpha,q} \\
&\qquad + b^\dagger_{\alpha,q} b_{\alpha,q} + b^\dagger_{\alpha,q} b^\dagger_{\alpha,-q} + b_{\alpha,q} b_{\alpha,-q} + b_{\alpha,q} b^\dagger_{\alpha,q} \Big) \\
&= \sum_{\alpha,q} \frac{\hbar\omega_{\alpha,q}}{2} \left( b_{\alpha,q} b^\dagger_{\alpha,q} + b^\dagger_{\alpha,q} b_{\alpha,q} \right) = \sum_{\alpha,q} \frac{\hbar\omega_{\alpha,q}}{2} \left( 1 + 2\hat{n}_{\alpha,q} \right) = \sum_{\alpha,q} \hbar\omega_{\alpha,q} \left( \hat{n}_{\alpha,q} + \frac{1}{2} \right) \,.
\end{aligned}$$

In step $(*)$ we have used $\omega_{\alpha,q} = \omega_{\alpha,-q}$ in order to exchange terms $\omega_{\alpha,q}(\ldots - b^\dagger_{\alpha,-q} b^\dagger_{\alpha,q} \ldots) \leftrightarrow \omega_{\alpha,-q}(\ldots - b^\dagger_{\alpha,q} b^{\dagger}{}_{\alpha,-q})$ in the summation. We conclude that (6.10) is indeed the correct quantization of the normal coordinate such that the in-plane vibrations (6.6) become quantized in terms of this operator,

$$\vec{S}(x,y,t) = \sum_{\alpha,q} \sqrt{\frac{\hbar}{2\,\rho LW\,\omega_{\alpha,q}}} \left( b_{\alpha,q}(t) + b^\dagger_{\alpha,-q}(t) \right) \left( f^{(\alpha,q)}_x(x) \vec{e}_x + f^{(\alpha,q)}_y(x) \vec{e}_y \right) e^{iqy} \,. \quad (6.11)$$

The operator $\vec{S}$ represents an observable and as such it must be hermitian. With

$$\begin{aligned}
\omega_{\alpha,q} &= \omega_{\alpha,-q} \,, \\
b_{\alpha,q}(t) + b^\dagger_{\alpha,-q}(t) &= \left( b_{\alpha,-q}(t) + b^\dagger_{\alpha,q}(t) \right)^\dagger \,, \\
f^{(\alpha,q)}_{x,y}(x) &= \left( f^{(\alpha,-q)}_{x,y}(x) \right)^*
\end{aligned}$$

all summands of (6.11) with $q < 0$ can be expressed via their $-q > 0$ counterpart[3]. In this representation,

$$\begin{aligned}\vec{S}(x,y,t) = &\sum_{\substack{\alpha,\,q\\ q>0}} \sqrt{\frac{\hbar}{2\,\rho LW\,\omega_{\alpha,q}}} \\ &\times \Big( \Big( b_{\alpha,q}(t) + b^\dagger_{\alpha,-q}(t) \Big) \; \big( f_x^{(\alpha,q)}(x)\vec{e}_x + f_y^{(\alpha,q)}(x)\vec{e}_y \big)\, e^{iqy} \\ &\quad + \Big( b_{\alpha,q}(t) + b^\dagger_{\alpha,-q}(t) \Big)^\dagger \big( f_x^{(\alpha,q)}(x)\vec{e}_x + f_y^{(\alpha,q)}(x)\vec{e}_y \big)^*\, e^{-iqy} \Big) \\ = &\sum_{\substack{\alpha,\,q\\ q>0}} \sqrt{\frac{\hbar}{2\,\rho LW\,\omega_{\alpha,q}}} \Big( b_{\alpha,q}(t) + b^\dagger_{\alpha,-q}(t) \Big) \big( f_x^{(\alpha,q)}(x)\vec{e}_x + f_y^{(\alpha,q)}(x)\vec{e}_y \big)\, e^{iqy} + h.c.\,,\end{aligned} \tag{6.12}$$

hermiticity becomes explicit. ✓

## 6.3. Deformation potential

Acoustic phonons compress and dilate the medium through which they travel. For small phonon amplitudes the relative compression/dilation is given by the trace of the strain tensor, $u_{ii}$, (A.6). This mechanism locally changes the charge density and thus the electric potential experienced by charge carriers. Due to its origin, this potential energy shift is referred to as the deformation potential. Figure 6.2 sketches the microscopic mechanism.

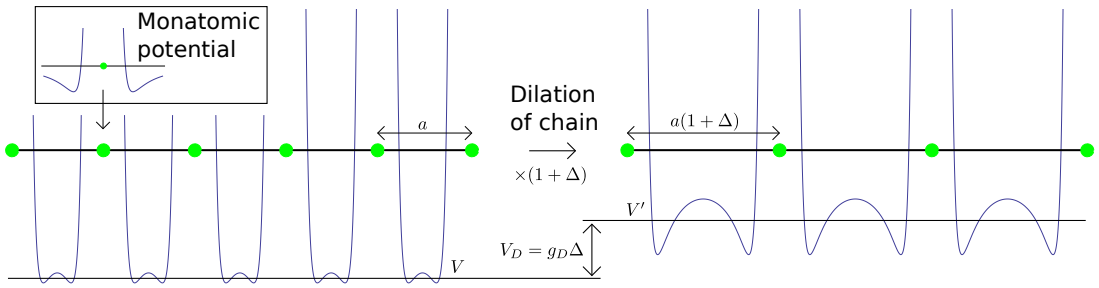


Figure 6.2.: The attractive potential of the nucleus is shielded by the surrounding electrons, yet a net attractive potential remains at a sufficiently large distance (inset). A dilation of the atomic chain (atomic distance $a$) from its equilibrium configuration effectively shifts this potential upwards. While atoms appear neutral from infinity, a nearby electron does feel a finite repulsive potential due to the negative charge of the atom's electron shell. Dilation or contraction of the atomic chain effectively changes this potential.

For a two-dimensional material, the area element $\mathrm{d}A_0$ is locally compressed / dilated to $\mathrm{d}A(x,y,t) = \mathrm{d}A_0(1 + \Delta(x,y,t))$, where $\Delta(x,y,t) := u_{xx}(x,y,t) + u_{yy}(x,y,t)$ is the trace

[3] A mode with $q = 0$ does not occur as its wavelength would be infinity.

of the strain tensor. Out-of-plane deformations $u_{zz}(x,y,t)$ do not contribute in lowest order. Consequently, the equilibrium charge density $n_0 = \mathrm{d}N/\mathrm{d}A_0$ is locally shifted to

$$n(x,y,t) = \frac{\mathrm{d}N}{\mathrm{d}A(x,y,t)} = \frac{\mathrm{d}N}{\mathrm{d}A_0(1+\Delta(x,y,t))} \approx n_0(1-\Delta(x,y,t))\,.$$

In effect, electrons experience a potential energy shift $V_D(x,y,t)$ proportional to the charge density shift $n_0 - n(x,y,t) = n_0\Delta(x,y,t)$:

$$\begin{aligned} V_D(x,y,t) &\propto n_0\Delta(x,y,t) \propto \Delta(x,y,t)\,, \\ \Rightarrow V_D(x,y,t) &= g_D\Delta(x,y,t)\,. \end{aligned}$$

Literature values for the coupling constant in graphene vary from 17 eV to 29 eV and we assume $g_D = 25\,\mathrm{eV}$, [Chen (2008), Bolotin (2008)].

A quantum mechanical expression for the deformation potential is obtained by expressing the strain tensor in terms of phonons. From (6.12), (A.1) and (A.5) we infer

$$\begin{aligned} & \vec{u}(x,y,t) \to \hat{\vec{S}}(x,y,t)\,, \\ \Rightarrow \quad & u_{xx}(x,y,t) + u_{yy}(x,y,t) \to \partial_x\hat{S}_x(x,y,t) + \partial_y\hat{S}_y(x,y,t)\,, \\ \Rightarrow \quad & V_D(x,y,t) \to \hat{H}_{EPC} := g_D\left(\partial_x\hat{S}_x(\hat{x},\hat{y},t) + \partial_y\hat{S}_y(\hat{x},\hat{y},t)\right)\,. \end{aligned}$$

The hamiltonian $H_{EPC}$ is the quantum mechanical representation of the deformation potential via which electrons feel the local deformation. That is, coordinates $x$, $y$ must be evaluated as electron coordinates, thus turning them into electron operators $\hat{x}$, $\hat{y}$. The electron-phonon coupling $H_{EPC}$ mediates electron energy to phonon states (relaxation via phonon creation) and vice versa. Due to the summation over in-plane modes $(\alpha, \pm q)$ on the right hand side, $H_{EPC}$ can be written as

$$H_{EPC} = \sum_{\substack{\alpha,\,q \\ q>0}} H_{EPC}^{(\alpha,\pm q)}\,, \tag{6.13}$$

where

$$H_{EPC}^{(\alpha,\pm q)} = g_D\sqrt{\frac{\hbar}{2\,\rho LW\,\omega_{\alpha,q}}}\left(b_{\alpha,q}(t) + b_{\alpha,-q}^{\dagger}(t)\right)\left(\partial_x f_x^{(\alpha,q)}(x) + iq f_y^{(\alpha,q)}(x)\right)e^{iqy} + h.c.$$

is the coupling to modes $(\alpha, \pm q)$. Hermiticity is conserved since the derivative of the *h.c.* term in (6.12) is indeed hermitian conjugate to the derivative of the explicit term in this equation[4].

[4] Complex conjugation and derivation commute as both operations are linear.

# 7. Spin relaxation

In this chapter, spin relaxation of a single electron in a GNR quantum dot via spin-orbit and electron-phonon coupling is discussed. First, we explain the admixture mechanism introduced by [Khaetskii (2001)], which couples electron spin to phonons. After the explicit study of all quantities, we finally calculate the relaxation rate via Fermi's Golden Rule.

## 7.1. Admixture mechanism

The electron-phonon interaction that we obtained from the deformation potential, $H_{EPC}$ (see (6.13)), does not couple to spin directly. Therefore, a spin-mixing mechanism (*admixture mechanism*) needs to be included to open a relaxation channel.

As a first step we consider product states $|n, s, N\rangle$ consisting of electron orbital state $|n\rangle$, electron spin state $|s\rangle$ and phonon Fock state $|N\rangle$. Since $H_{EPC}$ is spin-independent spin states can be treated separately:

$$\langle n, \downarrow, N_f | H_{EPC} | n, \uparrow, N_i \rangle = \langle n, N_f | H_{EPC} | n, N_i \rangle \underbrace{\langle \downarrow \mid \uparrow \rangle}_{=0} = 0 \quad (N_{i/f}\text{: initial/final}).$$

That is, spin cannot relax via $H_{EPC}$ alone. Electron-phonon interaction couples directly to the electron orbital but not to electron spin which is why product states $|n, s, N\rangle$ do not allow for spin relaxation. But phonons do couple to spin indirectly via a combination of electron-phonon *and* spin-orbit interaction.

Spin-orbit interaction can be treated as a perturbation of the electronic part of product states $|n, s, N\rangle$. The perturbation $H_{SO}$ (3.5) turns a product state with definite spin into a superposition of states with equal and opposite spin,

$$|n, \uparrow\rangle \to |n\uparrow\rangle = \sum_k c_{n\uparrow}^{(k)} |k, \uparrow\rangle + d_{n\uparrow}^{(k)} |k, \downarrow\rangle \,, \tag{7.1}$$

and accordingly for the opposite spin. The states $|n\uparrow\rangle, |n\downarrow\rangle$ represent corrected states that originate from unperturbed product states $|n, s\rangle$. The phonon Fock state remains unaffected such that we obtain electron-phonon product states of the form $|ns, N\rangle$. Instead of coupling phonons only to electron *orbital* states $|n\rangle$, $H_{EPC}$ now couples phonons to *combined* electronic states $|ns\rangle$. The contribution of both spins in the electronic states leads to non-zero matrix elements $\langle n\downarrow, N_f | H_{EPC} | n\uparrow, N_i \rangle$ (spin-flip). The resulting relaxation channel is depicted in figure 7.1.

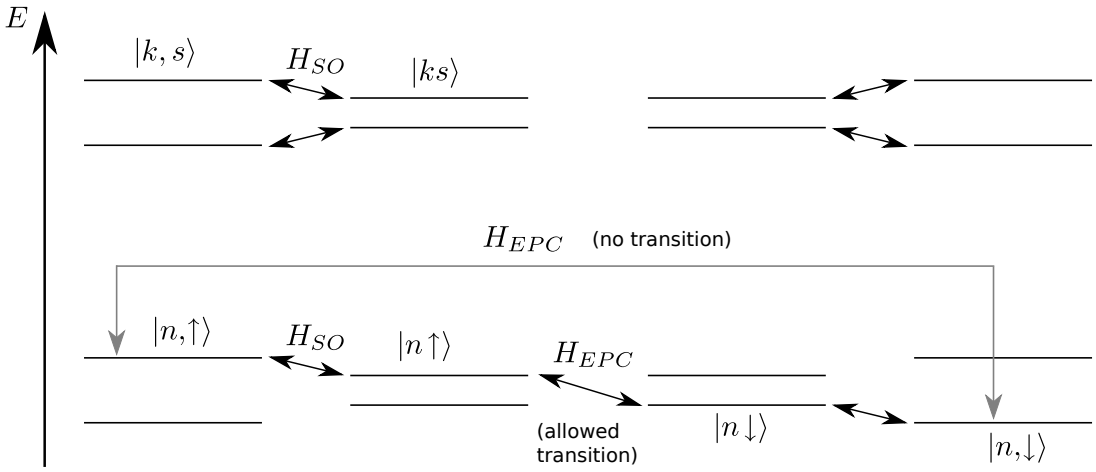


Figure 7.1.: Since $H_{EPC}$ is spin-independent it cannot couple $|\uparrow\rangle$ and $|\downarrow\rangle$ spin states directly. The spin-orbit interaction $H_{SO}$ mixes spin states and consequently opens an indirect relaxation channel.

We continue with the spin-orbit mixed states and then we evaluate the finite spin-flip matrix elements.

### 7.1.1. Spin-orbit mixed states

We treat (7.1) in first order perturbation theory, $|n\uparrow\rangle^{(1)} = |n,\uparrow\rangle + |n\uparrow\rangle^{(C_1)}$. The first order correction is given by

$$
\begin{aligned}
|n\uparrow\rangle^{(C_1)} &= \sum_{(k,s)\neq(n,\uparrow)} |k,s\rangle \frac{\langle k,s|H_{SO}|n,\uparrow\rangle}{E_{n,\uparrow} - E_{k,s}} \\
&= \sum_{(k,s)\neq(n,\uparrow)} |k,s\rangle \frac{\langle k,s|H_I|n,\uparrow\rangle + \langle k,s|H_R|n,\uparrow\rangle}{E_{n,\uparrow} - E_{k,s}} \\
&= \sum_{k\neq n} |k,\uparrow\rangle \frac{\langle k,\uparrow|H_I|n,\uparrow\rangle}{\left(E_n + \frac{g\mu_B B}{2}\right) - \left(E_k + \frac{g\mu_B B}{2}\right)} + \sum_k |k,\downarrow\rangle \frac{\langle k,\downarrow|H_R|n,\uparrow\rangle}{\left(E_n + \frac{g\mu_B B}{2}\right) - \left(E_k - \frac{g\mu_B B}{2}\right)} \\
&= \sum_{k\neq n} |k,\uparrow\rangle \underbrace{\frac{(H_I)^{\uparrow\uparrow}_{kn}}{E_n - E_k}}_{=c^{(k,1)}_{n\uparrow}} + \sum_k |k,\downarrow\rangle \underbrace{\frac{(H_R)^{\downarrow\uparrow}_{kn}}{E_n - E_k + g\mu_B B}}_{=d^{(k,1)}_{n\uparrow}} \\
&= \sum_{k\neq n} c^{(k,1)}_{n\uparrow} |k,\uparrow\rangle + \sum_k d^{(k,1)}_{n\uparrow} |k,\downarrow\rangle \,.
\end{aligned}
$$

For the second equality we have decomposed $H_{SO}$ into a part that conserves spin (intrinsic term $H_I$) and a spin flipping part (Rashba term $H_R$) and we have assumed a magnetic field perpendicular to the graphene plane[1]. The coefficient of $|n,\uparrow\rangle$ on the right hand side of (7.1) would be $c^{(n,1)}_{n\uparrow} = 1$ in this notation. According results hold for $|n\downarrow\rangle^{(1)}$, with

[1]Otherwise real spin ($s_z$) and Pseudo-spin ($\sigma_{z'}$) would be oriented differently ($\vec{e}_z \nparallel \vec{e}_{z'}$).

correction coefficients

$$c_{n\downarrow}^{(k,1)} = \frac{(H_I)_{kn}^{\downarrow\downarrow}}{E_n - E_k} \quad \text{and} \quad d_{n\downarrow}^{(k,1)} = \frac{(H_R)_{kn}^{\uparrow\downarrow}}{E_n - E_k - g\mu_B B}\,.$$

We note that, due to opposite spins, the matrix elements evaluate differently from above. Also, the Zeeman splitting has opposite sign and this is important because the system conserves time-reversal symmetry, which leads to Van Vleck cancellation [Van Vleck (1940)]. In the basis of these first order corrected states the spin flipping matrix elements of $H_{EPC}$ are (we omit the phonon states for a short notation; here, we focus on spin-orbit mixing of the electron state)

$$\begin{aligned}
\langle n\downarrow|^{(1)} H_{EPC} |n\uparrow\rangle^{(1)} &= \left(\langle n,\downarrow| + \sum_{k\neq n} c_{n\downarrow}^{(k,1)^*}\langle k,\downarrow| + \sum_k d_{n\downarrow}^{(k,1)^*}\langle k,\uparrow|\right) H_{EPC} \\
&\qquad \times \left(|n,\uparrow\rangle + \sum_{l\neq n} c_{n\uparrow}^{(l,1)}|l,\uparrow\rangle + \sum_l d_{n\uparrow}^{(l,1)}|l,\downarrow\rangle\right) \\
&= \sum_l \langle n|H_{EPC}|l\rangle d_{n\uparrow}^{(l,1)} + \sum_{\substack{k\neq n \\ l}} c_{n\downarrow}^{(k,1)^*}\langle k|H_{EPC}|l\rangle d_{n\uparrow}^{(l,1)} \\
&\quad + \sum_k d_{n\downarrow}^{(k,1)^*}\langle k|H_{EPC}|n\rangle + \sum_{\substack{k \\ l\neq n}} d_{n\downarrow}^{(k,1)^*}\langle k|H_{EPC}|l\rangle c_{n\uparrow}^{(l,1)} \\
&\approx \sum_k \left(\langle n|H_{EPC}|k\rangle d_{n\uparrow}^{(k,1)} + \langle k|H_{EPC}|n\rangle d_{n\downarrow}^{(k,1)^*}\right)\,. \qquad (7.2)
\end{aligned}$$

As expected, there is a finite overlap due to admixture of spins. We focus on lowest order and hence neglect terms with two corrections in the last step.

To evaluate this result, we determine the matrix elements of $H_R$ and of $H_{EPC}$ with the electrostatically confined electron states of chapter 4. As derived in this chapter, there are arbitrarily many transverse excitations $q_m$, (4.5), all of which contribute to (7.2). We assume the electron in the QD, whose spin is flipped, to have minimal energy, corresponding to the leftmost band in figure 7.2 (a). As the correction coefficients $d_{n\uparrow}^{(k,1)}$ go inversely with the energy splitting[2] $E_n - E_k$, contributions of higher transverse excitations will be much smaller, as illustrated by figure 7.2 (b). Therefore, we only take states with small energy splitting into account, that is bound[3] states of lowest transverse excitation with $q_{m=0}$.

For explicit calculations we use the states (4.11). Keeping $m = 0$ in mind, we free all quantities from their transverse excitation index and label them with the summation index of (7.2), e.g. $\alpha_{m=0} \to \alpha \to \alpha_k$. Then, the explicit form of the bound state

[2] For states of different transverse excitation the Zeeman term is much smaller than this splitting.

[3] For each transverse excitation there is a discrete spectrum of bound states and, beyond, a continuum of unbound states with energies in the conduction band of the barrier region, figure 4.2 (b).

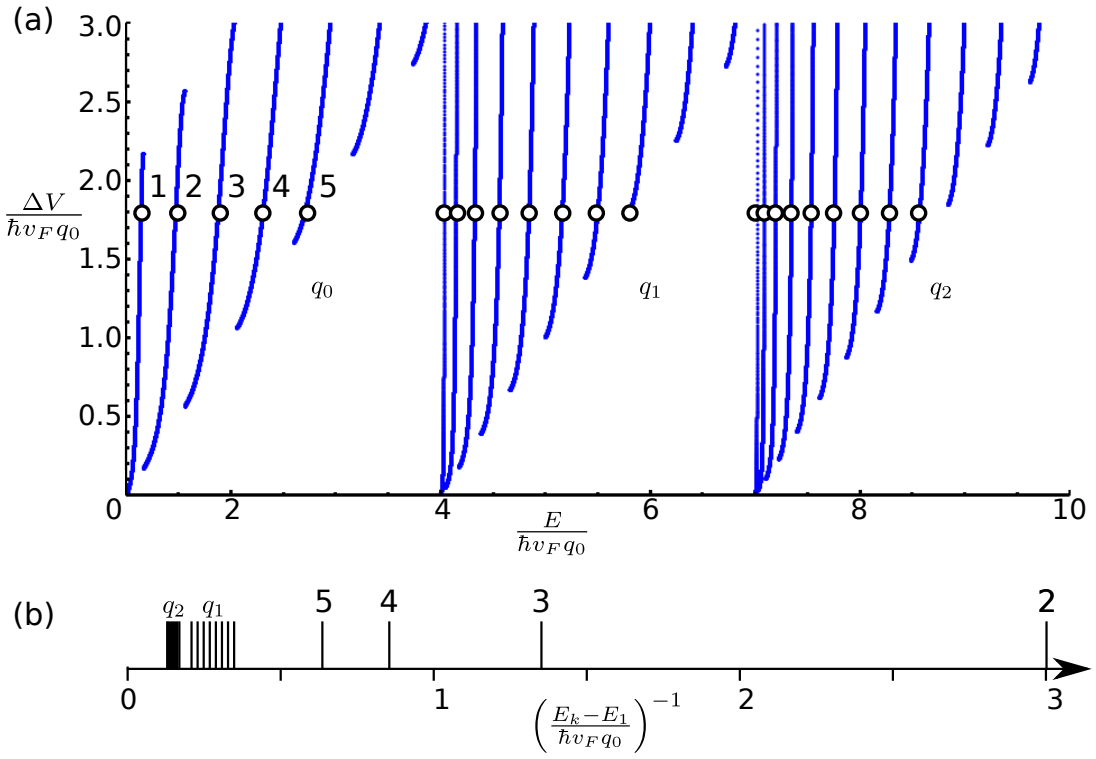


Figure 7.2.: (a) There are infinitely many transverse excitations. We plot the energy spectrum ($x$-coordinate) as a function of the potential difference $\Delta V$ between barrier and gate region ($y$-coordinate) for $q_0$, $q_1$ and $q_2$. Assuming $\Delta V = 1.8\hbar v_F q_0$, we enumerate the spectrum (equation (4.8)) from low to high energy $(1, 2, 3, ...)$. The $q_0$ part is similar to figure 4.3. (b) The correction coefficients are weighted with the inverse of the energy difference, which we plot for the energies indicated in (a). The $q_0$ series, denoted by numbers 2, 3, 4 and 5, clearly dominates such that we neglect higher transverse excitations. While in this graph the $q_1$ weights are still distinguishable from one another, the $q_2$ weights behave quasi-continuous, which also applies for higher series.

$|k\rangle = (\psi_A^{(K)}, \psi_B^{(K)}, -\psi_A^{(K')}, -\psi_B^{(K')})_k$ is written as follows:

$$y \leq 0 \Rightarrow \quad |k\rangle = \alpha_k \left( \begin{pmatrix} z_{k_B^{(k)}} \\ 1 \\ 0 \\ 0 \end{pmatrix} e^{iqx} + \begin{pmatrix} 0 \\ 0 \\ z_{k_B^{(k)}} \\ 1 \end{pmatrix} e^{-iqx} \right) e^{-ik_B^{(k)} y}, \tag{7.3}$$

$$0 \leq y \leq L \Rightarrow \quad |k\rangle = \beta_k \left( \begin{pmatrix} 1 \\ z_{k_G^{(k)}} \\ 0 \\ 0 \end{pmatrix} e^{iqx} + \begin{pmatrix} 0 \\ 0 \\ 1 \\ z_{k_G^{(k)}} \end{pmatrix} e^{-iqx} \right) e^{ik_G^{(k)} y}$$

$$+\gamma_k \left( \begin{pmatrix} z_{k_G^{(k)}} \\ 1 \\ 0 \\ 0 \end{pmatrix} e^{iqx} + \begin{pmatrix} 0 \\ 0 \\ z_{k_G^{(k)}} \\ 1 \end{pmatrix} e^{-iqx} \right) e^{-ik_G^{(k)} y},$$

$$L \leq y \Rightarrow \quad |k\rangle = \delta_k \left( \begin{pmatrix} 1 \\ z_{k_B^{(k)}} \\ 0 \\ 0 \end{pmatrix} e^{iqx} + \begin{pmatrix} 0 \\ 0 \\ 1 \\ z_{k_B^{(k)}} \end{pmatrix} e^{-iqx} \right) e^{ik_B^{(k)}(y-L)}.$$

The matrix element (7.2) involves quantities $d_{n\uparrow}^{(k,1)}$ and $\langle n|H_{EPC}|k\rangle$, which are discussed below. As we will calculate the relaxation time via Fermi's Golden Rule, (section 7.2.1), the *squared* matrix element $\left|\langle n\downarrow|^{(1)}H_{EPC}|n\uparrow\rangle^{(1)}\right|^2$ will be required.

### 7.1.2. Rashba matrix elements

For the correction coefficients $d_{n\uparrow}^{(k,1)}$ and $d_{n\downarrow}^{(k,1)^*}$ we need to calculate the matrix elements of the Rashba hamiltonian, which we have discussed in section 3.4. In agreement with table 3.5, explicit spin simplifies the matrix element $(H_R)_{kn}^{\downarrow\uparrow}$ to

$$\begin{aligned}
(H_R)_{kn}^{\downarrow\uparrow} &= \langle k,\downarrow|-\lambda_R(\sigma_x\tau_z s_y-\sigma_y s_x)|n,\uparrow\rangle = -\lambda_R\langle k|i\sigma_x\tau_z-\sigma_y|n\rangle \\
&= -\lambda_R\int_0^W\int_{-\infty}^{\infty}\begin{pmatrix}\psi_A^{(K)}\\ \psi_B^{(K)}\\ -\psi_A^{(K')}\\ -\psi_B^{(K')}\end{pmatrix}_k^{\dagger}\begin{pmatrix}0&2i&0&0\\0&0&0&0\\0&0&0&0\\0&0&-2i&0\end{pmatrix}\begin{pmatrix}\psi_A^{(K)}\\ \psi_B^{(K)}\\ -\psi_A^{(K')}\\ -\psi_B^{(K')}\end{pmatrix}_n \mathrm{d}x\,\mathrm{d}y \\
&= -2i\lambda_R\int_0^W\int_{-\infty}^{\infty}\left(\psi_{A,k}^{(K)^*}\psi_{B,n}^{(K)}-\psi_{B,k}^{(K')^*}\psi_{A,n}^{(K')}\right)\mathrm{d}x\,\mathrm{d}y\,. \qquad (7.4)
\end{aligned}$$

As the wavefunction is defined piecewise for the barrier and gate regions we need to split the $y$-integration into according parts. For $y\le 0$ we find with (7.3)

$$\begin{aligned}
&\int_0^W\int_{-\infty}^0\left(\psi_{A,k}^{(K)^*}\psi_{B,n}^{(K)}-\psi_{B,k}^{(K')^*}\psi_{A,n}^{(K')}\right)\mathrm{d}x\,\mathrm{d}y \\
&\quad= \int_0^W\int_{-\infty}^0\Big(\alpha_k^* z_{k_B^{(k)}}e^{-iqx+|k_B^{(k)}|y}\alpha_n e^{iqx+|k_B^{(n)}|y} \\
&\qquad\qquad -(-\alpha_k^*)e^{iqx+|k_B^{(k)}|y}(-\alpha_n)z_{k_B^{(n)}}e^{-iqx+|k_B^{(n)}|y}\Big)\mathrm{d}x\,\mathrm{d}y \\
&\quad= \alpha_k^*\alpha_n\int_0^W\int_{-\infty}^0(z_{k_B^{(k)}}-z_{k_B^{(n)}})e^{(|k_B^{(k)}|+|k_B^{(n)}|)y}\mathrm{d}x\,\mathrm{d}y \\
&\quad= \frac{\alpha_k^*\alpha_n W(z_{k_B^{(k)}}-z_{k_B^{(n)}})}{|k_B^{(k)}|+|k_B^{(n)}|}\left[e^{(|k_B^{(k)}|+|k_B^{(n)}|)y}\right]_{-\infty}^0 = \frac{\alpha_k^*\alpha_n W(z_{k_B^{(k)}}-z_{k_B^{(n)}})}{|k_B^{(k)}|+|k_B^{(n)}|}\,, \qquad (7.5)
\end{aligned}$$

where we have used $k_B = i|k_B|$ and $z_{k_B}\in\mathbb{R}$ (see (4.10) and (4.7)). Accordingly, for the other barrier region ($L\le y$) the result is

$$\int_0^W\int_L^{\infty}\left(\psi_{A,k}^{(K)^*}\psi_{B,n}^{(K)}-\psi_{B,k}^{(K')^*}\psi_{A,n}^{(K')}\right)\mathrm{d}x\,\mathrm{d}y = \frac{\delta_k^*\delta_n W(z_{k_B^{(n)}}-z_{k_B^{(k)}})}{|k_B^{(k)}|+|k_B^{(n)}|}\,. \qquad (7.6)$$

In the gated region ($0 \le y \le L$) we have to distinguish $k \neq n$ and $k = n$. We treat the former case first, for simplicity only one summand at a time:

$$\begin{aligned}
&\int_0^W \int_0^L \psi_{A,k}^{(K)^*} \psi_{B,n}^{(K)} \mathrm{d}x\,\mathrm{d}y \\
&= \int_0^W \int_0^L \left(\beta_k^* e^{-i(qx+k_G^{(k)}y)} + \gamma_k^* z_{k_G^{(k)}}^* e^{-i(qx-k_G^{(k)}y)}\right)\left(\beta_n z_{k_G^{(n)}} e^{i(qx+k_G^{(n)}y)} + \gamma_n e^{i(qx-k_G^{(n)}y)}\right) \mathrm{d}x\,\mathrm{d}y \\
&= \int_0^W \int_0^L \Big(\beta_k^*\beta_n z_{k_G^{(n)}} e^{-i(k_G^{(k)}-k_G^{(n)})y} + \beta_k^*\gamma_n e^{-i(k_G^{(k)}+k_G^{(n)})y} \\
&\qquad\qquad + \gamma_k^* z_{k_G^{(k)}}^* \beta_n z_{k_G^{(n)}} e^{i(k_G^{(k)}+k_G^{(n)})y} + \gamma_k^* z_{k_G^{(k)}}^* \gamma_n e^{i(k_G^{(k)}-k_G^{(n)})y}\Big) \mathrm{d}x\,\mathrm{d}y \\
&= \beta_k^*\beta_n z_{k_G^{(n)}} W \frac{e^{-i(k_G^{(k)}-k_G^{(n)})L}-1}{-i(k_G^{(k)}-k_G^{(n)})} + \beta_k^*\gamma_n W \frac{e^{-i(k_G^{(k)}+k_G^{(n)})L}-1}{-i(k_G^{(k)}+k_G^{(n)})} \\
&\quad + \gamma_k^* z_{k_G^{(k)}}^* \beta_n z_{k_G^{(n)}} W \frac{e^{i(k_G^{(k)}+k_G^{(n)})L}-1}{i(k_G^{(k)}+k_G^{(n)})} + \gamma_k^* z_{k_G^{(k)}}^* \gamma_n W \frac{e^{i(k_G^{(k)}-k_G^{(n)})L}-1}{i(k_G^{(k)}-k_G^{(n)})}\,. \qquad (7.7)
\end{aligned}$$

The other summand is

$$\begin{aligned}
&-\int_0^W \int_0^L \psi_{B,k}^{(K')^*} \psi_{A,n}^{(K')} \mathrm{d}x\,\mathrm{d}y \\
&\qquad = -\beta_k^* z_{k_G^{(k)}}^* \beta_n W \frac{e^{-i(k_G^{(k)}-k_G^{(n)})L}-1}{-i(k_G^{(k)}-k_G^{(n)})} - \beta_k^* z_{k_G^{(k)}}^* \gamma_n z_{k_G^{(n)}} W \frac{e^{-i(k_G^{(k)}+k_G^{(n)})L}-1}{-i(k_G^{(k)}+k_G^{(n)})} \\
&\qquad\quad -\gamma_k^*\beta_n W \frac{e^{i(k_G^{(k)}+k_G^{(n)})L}-1}{i(k_G^{(k)}+k_G^{(n)})} - \gamma_k^*\gamma_n z_{k_G^{(n)}} W \frac{e^{i(k_G^{(k)}-k_G^{(n)})L}-1}{i(k_G^{(k)}-k_G^{(n)})}\,.
\end{aligned}$$

and they add up to

$$\begin{aligned}
&\int_0^W \int_0^L \left(\psi_{A,k}^{(K)^*}\psi_{B,n}^{(K)} - \psi_{B,k}^{(K')^*}\psi_{A,n}^{(K')}\right) \mathrm{d}x\,\mathrm{d}y \\
&\qquad = \frac{z_{k_G^{(k)}}^* - z_{k_G^{(n)}}}{i(k_G^{(k)}-k_G^{(n)})} W \left(\beta_k^*\beta_n\left(e^{-i(k_G^{(k)}-k_G^{(n)})L}-1\right) + \gamma_k^*\gamma_n\left(e^{i(k_G^{(k)}-k_G^{(n)})L}-1\right)\right) \\
&\qquad\quad + \frac{z_{k_G^{(k)}}^* z_{k_G^{(n)}} - 1}{i(k_G^{(k)}+k_G^{(n)})} W \left(\gamma_k^*\beta_n\left(e^{i(k_G^{(k)}+k_G^{(n)})L}-1\right) + \beta_k^*\gamma_n\left(e^{-i(k_G^{(k)}+k_G^{(n)})L}-1\right)\right)\,. \qquad (7.8)
\end{aligned}$$

If $k = n$, we follow the first steps of (7.7) but make use $k_G^{(k)} = k_G^{(n)}$, leading to

$$\begin{aligned}
&\int_0^W \int_0^L \left(\psi_{A,n}^{(K)^*}\psi_{B,n}^{(K)} - \psi_{B,n}^{(K')^*}\psi_{A,n}^{(K')^*}\right) \mathrm{d}x\,\mathrm{d}y \\
&= \int_0^W \int_0^L \left(\beta_n^*\beta_n z_{k_G^{(n)}} + \beta_n^*\gamma_n e^{-2ik_G^{(n)}y} + \gamma_n^*\beta_n z_{k_G^{(n)}}^* z_{k_G^{(n)}} e^{2ik_G^{(n)}y} + \gamma_n^*\gamma_n z_{k_G^{(n)}}^*\right) \mathrm{d}x\,\mathrm{d}y \\
&- \int_0^W \int_0^L \left(\beta_n^*\beta_n z_{k_G^{(n)}}^* + \beta_n^*\gamma_n z_{k_G^{(n)}}^* z_{k_G^{(n)}} e^{-2ik_G^{(n)}y} + \gamma_n^*\beta_n e^{2ik_G^{(n)}y} + \gamma_n^*\gamma_n z_{k_G^{(n)}}\right) \mathrm{d}x\,\mathrm{d}y \\
&\overset{(*)}{=} \int_0^W \int_0^L \left(\beta_n^*\beta_n (z_{k_G^{(n)}} - z_{k_G^{(n)}}^*) + \gamma_n^*\gamma_n (z_{k_G^{(n)}}^* - z_{k_G^{(n)}})\right) \mathrm{d}x\,\mathrm{d}y \\
&= (z_{k_G^{(n)}} - z_{k_G^{(n)}}^*)(\beta_n^*\beta_n - \gamma_n^*\gamma_n) LW \propto |\beta_n|^2 - |\gamma_n|^2 = 0\,,
\end{aligned}$$

where we have used $|z_{k_G^{(n)}}| = 1$ in step $(*)$. Symmetry dictates $|\beta_n|^2 = |\gamma_n|^2$ such that the integral becomes zero. For $k = n$, this is also holds for the sum of (7.5) and (7.6), as $|\alpha_n|^2 = |\delta_n|^2$. That is, $(H_R)^{\downarrow\uparrow}_{nn} = 0$. For $k \neq n$, the integral in (7.4) is given by the sum of terms (7.5), (7.6) and (7.8). All integrals are confirmed numerically and it turns out that the sum is zero not only for $k - n = 0$ but more generally[4] for $k - n = 0$, $\pm 2$, $\pm 4$, ... and finite otherwise.

For opposite spins, we find accordingly (see table 3.5)

$$(H_R)^{\uparrow\downarrow}_{kn} = 2i\lambda_R \int_0^W \int_{-\infty}^{\infty} \left( \psi^{(K)^*}_{B,k} \psi^{(K)}_{A,n} - \psi^{(K')^*}_{A,k} \psi^{(K')}_{B,n} \right) \mathrm{d}x \, \mathrm{d}y \,.$$

From (7.3) we see that the integral in the barrier region $y \leq 0$ can be inferred from the above result with the replacements $\alpha_k \to \alpha_k z_{k_B^{(k)}}$ and $\alpha_k z_{k_B^{(k)}} \to \alpha_k$:

$$\begin{aligned} (7.5) \quad \Rightarrow \quad & \frac{\alpha_k^* \alpha_n W(z^*_{k_B^{(k)}} - z_{k_B^{(n)}})}{|k_B^{(k)}| + |k_B^{(n)}|} \\ \to \quad & \frac{\alpha_k^* \alpha_n W(z_{k_B^{(n)}} - z^*_{k_B^{(k)}})}{|k_B^{(k)}| + |k_B^{(n)}|} = \int_0^W \int_{-\infty}^{0} \left( \psi^{(K)^*}_{B,k} \psi^{(K)}_{A,n} - \psi^{(K')^*}_{A,k} \psi^{(K')}_{B,n} \right) \mathrm{d}x \, \mathrm{d}y \,. \end{aligned}$$

The integrals in for $0 \leq y \leq L$ and $L \leq y$ are obtained with analog replacements for $\beta_k$, $\gamma_k$ and $\delta_k$. All integrals are the negative of those above such that, with the prefactor $2i\lambda_R$ instead of $-2i\lambda_R$ the matrix elements are the same[5] $(H_R)^{\uparrow\downarrow}_{kn} = (H_R)^{\downarrow\uparrow}_{kn}$.

The correction coefficients $d^{(k,1)}_{n\uparrow}$ and $d^{(k,1)}_{n\downarrow}$ are obtained from these matrix elements via division by $E_n - E_k \pm g\mu_B B$. We point out that the energy splitting is dominated by $E_n - E_k$ (for $k \neq n$) such that the coefficients with $k = n$ would contribute the dominant corrections. However, the numerator of these terms is zero such that only smaller corrections contribute.

### 7.1.3. Electron-phonon matrix elements

The admixture mechanism allows an electron to dissipate its Zeeman energy into the lattice via phonon emission. For sufficiently low temperature we can assume initial phononic vacuum, $|N_i\rangle = |0\rangle$, and a single phonon with the Zeeman energy in the final state, $|N_f\rangle = |1_{\alpha,\pm q_{z\alpha}}\rangle$. The phonon can travel in both ribbon directions and the contributions to the relaxation rate are the same. That is we can focus on one direction and then multiply the obtained rate by two. As previously, the indices $_{\alpha,q}$ label dispersion branch and wavenumber, respectively. On branch $\alpha$, wavenumbers $\pm q_{z\alpha}$ satisfy the Zeeman condition, $\hbar\omega_{\alpha,q_{z\alpha}} = g\mu_B B$, figure 7.3. With these phonon states the matrix element

[4] We enumerate the states in order of increasing energy.

[5] With the explicit form of the indexed quantities ($\alpha_k$ etc.) this result can be confirmed by complex conjugation and interchange of indices, $k \leftrightarrow n$.

$\langle n\downarrow^{(1)}, N_f|H_{EPC}|n\uparrow^{(1)}, N_i\rangle$ in (7.2) becomes

$$\langle n\downarrow^{(1)}, 1_{\alpha,\pm q_{z\alpha}}|H_{EPC}|n\uparrow^{(1)}, 0\rangle \approx \sum_k \langle n, 1_{\alpha,\pm q_{z\alpha}}|H_{EPC}|k, 0\rangle d_{n\uparrow}^{(k,1)} + \langle k, 1_{\alpha,\pm q_{z\alpha}}|H_{EPC}|n, 0\rangle d_{n\downarrow}^{(k,1)*}. \tag{7.9}$$

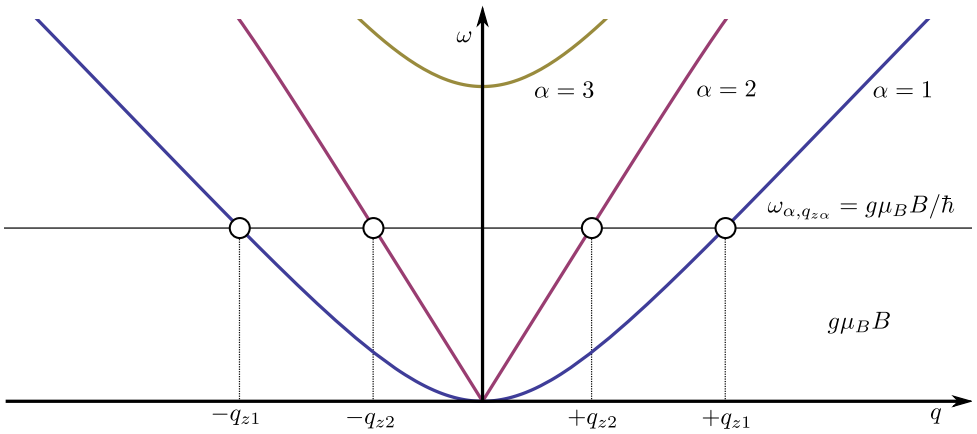


Figure 7.3.: We plot once more the dispersion of in-plane phonons (see also figure 5.7 (c); here, we plot polynomial fits to those data points). Wavenumbers that satisfy the Zeeman condition, $\hbar\omega_{\alpha,q_{z\alpha}} = g\mu_B B$, are indicated with circles. For convenient magnetic fields only the branches $\alpha = 1, 2$ are available. It turns out that the contribution to the deformation potential from $\alpha = 1$ cancels out over the ribbon width such that only the modes $(2, \pm q_{z2})$ are relevant for spin flip.

The electron-phonon coupling $H_{EPC}$ has been discussed in section 6.3 and from the sum in (6.13) it follows that only the term $q = q_{z\alpha}$ contributes. Due to symmetry, both final states $|1_{\alpha,\pm q_{z\alpha}}\rangle$ are equivalent but for convenience[6] we treat $|1_{\alpha,-q_{z\alpha}}\rangle$. Then, the left hand side of (7.9) becomes $\langle n\downarrow^{(1)}, 1_{\alpha,-q_{z\alpha}}|H_{EPC}^{(\alpha,q_{z\alpha})}|n\uparrow^{(1)}, 0\rangle$ and the typical matrix element on the right hand side is

$$\begin{aligned}\langle n, 1_{\alpha,-q_{z\alpha}}|H_{EPC}^{(\alpha,q_{z\alpha})}|k, 0\rangle &\overset{(6.13)}{=} C_{\alpha,q_{z\alpha}} \Big(\langle n|g^{(\alpha,q_{z\alpha})}\ (x,y)|k\rangle\langle 1_{\alpha,-q_{z\alpha}}|b_{\alpha,q_{z\alpha}}(t) + b^\dagger_{\alpha,-q_{z\alpha}}(t)|0\rangle \\ &\qquad + \langle n|g^{(\alpha,q_{z\alpha})^*}\ (x,y)|k\rangle\langle 1_{\alpha,-q_{z\alpha}}|b_{\alpha,-q_{z\alpha}}(t) + b^\dagger_{\alpha,q_{z\alpha}}(t)|0\rangle\Big) \\ &= C_{\alpha,q_{z\alpha}}\langle n|g^{(\alpha,q_{z\alpha})}(x,y)|k\rangle\,,\end{aligned}$$

[6]The electron-phonon coupling (6.13) contains creation and annihilation operators. Here, we treat phonon emission, that is creation. We find it convenient to deal with the explicit part of (6.13), which creates a phonon with negative wavenumber $(-q_{z\alpha})$.

where we have used the short hand notation

$$C_{\alpha,q_{z\alpha}}\langle n|g^{(\alpha,q_{z\alpha})}(x,y)|k\rangle = \underbrace{g_D\sqrt{\frac{\hbar}{2\,\rho LW\omega_{\alpha,q_{z\alpha}}}}}_{=:\,C_{\alpha,q_{z\alpha}}}\langle n|\underbrace{(\partial_x f_x^{(\alpha,q_{z\alpha})}(x)+iq_{z\alpha}f_y^{(\alpha,q_{z\alpha})}(x))e^{iq_{z\alpha}y}}_{=:\,g^{(\alpha,q_{z\alpha})}(x,y)}|k\rangle$$
$$= C_{\alpha,q_{z\alpha}}\int_0^W\int_{-\infty}^{\infty}\psi_n^\dagger(x,y)g^{(\alpha,q_{z\alpha})}(x,y)\psi_k(x,y)\,\mathrm{d}x\,\mathrm{d}y\,.$$

Again, we carry out the integration separately for barrier and gated regions. For $y\le 0$ we find

$$\begin{aligned}
&\int_0^W\int_{-\infty}^0\psi_n^\dagger g^{(\alpha,q_{z\alpha})}\psi_k\,\mathrm{d}x\,\mathrm{d}y\\
&\quad=\int_0^W\int_{-\infty}^0 g^{(\alpha,q_{z\alpha})}\left(\psi_{A,n}^{(K)^*}\psi_{A,k}^{(K)}+\psi_{B,n}^{(K)^*}\psi_{B,k}^{(K)}+\psi_{A,n}^{(K')^*}\psi_{A,k}^{(K')}+\psi_{B,n}^{(K')^*}\psi_{B,k}^{(K')}\right)\mathrm{d}x\,\mathrm{d}y\\
&\quad\overset{(7.3)}{=}\int_0^W\int_{-\infty}^0 g^{(\alpha,q_{z\alpha})}(x,y)\alpha_n^*\alpha_k\left(z^*_{k_B^{(n)}}z_{k_B^{(k)}}+1+z^*_{k_B^{(n)}}z_{k_B^{(k)}}+1\right)\\
&\qquad\times e^{i(q_e-q_e)x}e^{(|k_B^{(n)}|+|k_B^{(k)}|)y}\,\mathrm{d}x\,\mathrm{d}y\\
&\quad=2\alpha_n^*\alpha_k(1+z_{k_B^{(n)}}z_{k_B^{(k)}})\int_0^W(\partial_x f_x^{(\alpha,q_{z\alpha})}(x)+iq_{z\alpha}f_y^{(\alpha,q_{z\alpha})}(x))\,\mathrm{d}x\\
&\qquad\times\underbrace{\int_{-\infty}^0 e^{iq_{z\alpha}y+(|k_B^{(n)}|+|k_B^{(k)}|)y}\,\mathrm{d}y}_{=1/(|k_B^{(n)}|+|k_B^{(k)}|+iq_{z\alpha})}\\
&\quad=\underbrace{\frac{2\alpha_n^*\alpha_k(1+z_{k_B^{(n)}}z_{k_B^{(k)}})}{|k_B^{(n)}|+|k_B^{(k)}|+iq_{z\alpha}}}_{=:\,M_{y1}^{(\alpha,q_{z\alpha})}}\underbrace{\int_0^W(\partial_x f_x^{(\alpha,q_{z\alpha})}(x)+iq_{z\alpha}f_y^{(\alpha,q_{z\alpha})}(x))\,\mathrm{d}x}_{=:\,M_x^{(\alpha,q_{z\alpha})}}\,,
\end{aligned}\tag{7.10}$$

where we denote the electron's transverse wavenumber as $q_e$ in order to disambiguate it from the longitudinal phonon wavenumber $q_{z\alpha}$. However, it cancels out since $\psi_n^*$ and $\psi_k$ are of the same (lowest) transverse excitation. With the explicit form of functions $f_{x,y}$, (5.16), we perform the $x$-integration:

$$\begin{aligned}
\partial_x f_x(x)+iqf_y(x) &= \left(\lambda_1-\frac{q^2}{\lambda_1}\right)c_1e^{\lambda_1 x}+\left(\lambda_2-\frac{q^2}{\lambda_2}\right)c_2e^{\lambda_2 x}\\
&\quad+\underbrace{(\lambda_3-\lambda_3)\,c_3e^{\lambda_3 x}+(\lambda_4-\lambda_4)\,c_4e^{\lambda_4 x}}_{=0}\,,\\
\Rightarrow\quad\int_0^W(\partial_x f_x(x)+iqf_y(x))\,\mathrm{d}x &= \int_0^W\left(\left(\lambda_1-\frac{q^2}{\lambda_1}\right)c_1e^{\lambda_1 x}+\left(\lambda_2-\frac{q^2}{\lambda_2}\right)c_2e^{\lambda_2 x}\right)\mathrm{d}x\\
&\overset{(*)}{=}\left(1-\frac{q^2}{\lambda_1^2}\right)\left[c_1e^{\lambda_1 x}+c_2e^{-\lambda_1 x}\right]_0^W\,,\\
\Rightarrow\quad M_x^{(\alpha,q_{z\alpha})} &= \left(1-\frac{q_{z\alpha}^2}{\lambda_1^{(\alpha,q_{z\alpha})^2}}\right)\left(c_1^{(\alpha,q_{z\alpha})}\left(e^{\lambda_1^{(\alpha,q_{z\alpha})}W}-1\right)+c_2^{(\alpha,q_{z\alpha})}\left(e^{-\lambda_1^{(\alpha,q_{z\alpha})}W}-1\right)\right)\,.
\end{aligned}\tag{7.11}$$

In step $(*)$, we have used $\lambda_1 = -\lambda_2$. Noticeably, terms from $c_3 e^{\lambda_3 x}$ and $c_4 e^{\lambda_4 x}$ vanish. While these expressions do deform the ribbon as well, they only change the local shape but do not affect the local surface area because dilation in one direction is compensated by compression in the other direction. Consequently, there is no contribution to the deformation potential.

The total integral for the barrier region $y \leq 0$ is given by (7.10) with the above result, which also holds for the other regions ($0 \leq y \leq L$ and $L \leq y$) as the according expressions factorize similarly into $x$- and $y$-integrations. For the other barrier region ($L \leq y$) we find

$$\begin{aligned}
&\int_0^W \int_L^\infty \psi_n^\dagger g^{(\alpha,q_{z\alpha})} \psi_k \,\mathrm{d}x\,\mathrm{d}y \\
&\qquad = 2\delta_n^* \delta_k (1 + z_{k_B^{(n)}} z_{k_B^{(k)}}) \int_0^W (\partial_x f_x^{(\alpha,q_{z\alpha})}(x) + i q_{z\alpha} f_y^{(\alpha,q_{z\alpha})}(x)) \,\mathrm{d}x \\
&\qquad\quad \times \underbrace{\int_L^\infty e^{i q_{z\alpha} y} e^{-(|k_B^{(n)}| + |k_B^{(k)}|)(y-L)} \,\mathrm{d}y}_{= -e^{i q_{z\alpha} L}/(i q_{z\alpha} - |k_B^{(n)}| - |k_B^{(k)}|)} \\
&\qquad = \underbrace{\frac{2\delta_n^* \delta_k (1 + z_{k_B^{(n)}} z_{k_B^{(k)}}) e^{-i q_{z\alpha} L}}{|k_B^{(n)}| + |k_B^{(k)}| - i q_{z\alpha}}}_{=: M_{y3}^{(\alpha,q_{z\alpha})}} \int_0^W (\partial_x f_x^{(\alpha,q_{z\alpha})}(x) + i q_{z\alpha} f_y^{(\alpha,q_{z\alpha})}(x)) \,\mathrm{d}x
\end{aligned} \tag{7.12}$$

and for the gated region ($0 \leq y \leq L$) we have to integrate

$$\begin{aligned}
&\int_0^W \int_0^L \psi_n^\dagger g^{(\alpha,q_{z\alpha})} \psi_k \,\mathrm{d}x\,\mathrm{d}y \\
&\quad = \int_0^L \Big( 2\beta_n^* \beta_k (1 + z^*_{k_G^{(n)}} z_{k_G^{(k)}}) e^{i(-k_G^{(n)} + k_G^{(k)} + q_{z\alpha})y} + 2\beta_n^* \gamma_k (z^*_{k_G^{(n)}} + z_{k_G^{(k)}}) e^{i(-k_G^{(n)} - k_G^{(k)} + q_{z\alpha})y} \\
&\qquad + 2\gamma_n^* \beta_k (z^*_{k_G^{(n)}} + z_{k_G^{(k)}}) e^{i(k_G^{(n)} + k_G^{(k)} + q_{z\alpha})y} + 2\gamma_n^* \gamma_k (1 + z^*_{k_G^{(n)}} z_{k_G^{(k)}}) e^{i(k_G^{(n)} - k_G^{(k)} + q_{z\alpha})y} \Big) \,\mathrm{d}y \,. \\
&\quad \times \int_0^W (\partial_x f_x^{(\alpha,q_{z\alpha})}(x) + i q_{z\alpha} f_y^{(\alpha,q_{z\alpha})}(x)) \,\mathrm{d}x \,.
\end{aligned}$$

The $y$-integral of this expression is

$$\begin{aligned}
\int_0^L \cdots \mathrm{d}y = \; 2 \Bigg( & \frac{\beta_n^* \beta_k (1 + z^*_{k_G^{(n)}} z_{k_G^{(k)}})}{i(q_{z\alpha} - k_G^{(n)} + k_G^{(k)})} \left( e^{i(q_{z\alpha} - k_G^{(n)} + k_G^{(k)})L} - 1 \right) \\
& + \frac{\beta_n^* \gamma_k (z^*_{k_G^{(n)}} + z_{k_G^{(k)}})}{i(q_{z\alpha} - k_G^{(n)} - k_G^{(k)})} \left( e^{i(q_{z\alpha} - k_G^{(n)} - k_G^{(k)})L} - 1 \right) \\
& + \frac{\gamma_n^* \beta_k (z^*_{k_G^{(n)}} + z_{k_G^{(k)}})}{i(q_{z\alpha} + k_G^{(n)} + k_G^{(k)})} \left( e^{i(q_{z\alpha} + k_G^{(n)} + k_G^{(k)})L} - 1 \right) \\
& + \frac{\gamma_n^* \gamma_k (1 + z^*_{k_G^{(n)}} z_{k_G^{(k)}})}{i(q_{z\alpha} + k_G^{(n)} - k_G^{(k)})} \left( e^{i(q_{z\alpha} + k_G^{(n)} - k_G^{(k)})L} - 1 \right) \Bigg) =: M_{y2}^{(\alpha,q_{z\alpha})}
\end{aligned} \tag{7.13}$$

and the $x$-integration as above. With (7.10), (7.11), (7.12) and (7.13) we put the matrix element on the right hand side of (7.9) together:

$$\langle n, 1_{\alpha,-q_{z\alpha}}|H_{EPC}^{(\alpha,q_{z\alpha})}|k,0\rangle = C_{\alpha,q_{z\alpha}} M_x^{(\alpha,q_{z\alpha})} \left(M_{y1}^{(\alpha,q_{z\alpha})} + M_{y2}^{(\alpha,q_{z\alpha})} + M_{y3}^{(\alpha,q_{z\alpha})}\right) . \qquad (7.14)$$

The other term, $\langle k, 1_{\alpha,-q_{z\alpha}}|H_{EPC}|n,0\rangle$, is *not* the complex conjugate of this result[7], but can be calculated the same way. For the final state $|1_{\alpha,+q_{z\alpha}}\rangle$ amplitudes are the same but there is a phase shift due to $e^{\pm i q_{z\alpha} y}$.

While the dimensionless quantities $d_{n\uparrow}^{(k,1)}$ are independent of the ribbon width, this does not apply for $\langle n|H_{EPC}|k\rangle$. To assign the Zeeman energy $g\mu_B B$ a wavenumber $q_{z\alpha}$ and a frequency $\omega_{\alpha,q_{z\alpha}}$, the ribbon width $W$ needs to be fixed. We choose $W = 30\,\mathrm{nm}$. For a magnetic field of $B = 1T$, we resolve from (5.22)

$$\begin{aligned} & \omega_{\alpha,q_{z\alpha}} = 18 \times 10^{10}\,\frac{1}{\mathrm{s}} = 2\pi \times 28.6\,\mathrm{GHz} \\ \Rightarrow \quad & \tilde{\omega}_{\alpha,q_{z\alpha}} = 0.18\,. \end{aligned}$$

Only the two lowest in-plane phonon branches have modes for this parameter, figure 7.3. The deformation potential for the $\alpha = 1$ branch is antisymmetric with respect to the ribbon axis such that the integration in (7.11) yields zero, $M_x^{(1,q_{z1})} = 0$. Consequently only the other branch, $\alpha = 2$, can induce spin-flips via the admixture mechanism. On this branch, the wavenumber goes linearly with frequency, $q \propto \omega$, for magnetic fields up to more than 10 T.

### 7.1.4. Squared spin-flip matrix element

Now, we have all the terms that constitute the matrix element (7.2). We explicitly put in all analytical and numerical quantities to calculate

$$\left|\langle n\downarrow^{(1)}, 1_{\alpha,-q_{z\alpha}}|H_{EPC}|n\uparrow^{(1)},0\rangle\right|^2 = \left(\frac{g_D\lambda_R}{\hbar v_F \pi/3}\right)^2 \frac{\hbar}{2\,\rho L W \omega_{\alpha,q_{z\alpha}}} |\tilde{H}_{\downarrow\uparrow,EPC}^{nn,(\alpha,\tilde{q}_{z\alpha})}|^2\,, \qquad (7.15)$$

where $|\tilde{H}_{\downarrow\uparrow,EPC}^{nn,(\alpha,\tilde{q}_{z\alpha})}|^2$ is the dimensionless analogon of the left hand side and determined numerically. For $n = 1$ (QD ground state), $\alpha = 2$ (only contributing branch for conventional magnetic fields), $W = 30\,\mathrm{nm}$ and $B = 1\,\mathrm{T}$, we find

$$|\tilde{H}_{\downarrow\uparrow,EPC}^{11,(2,\tilde{q}_{z2})}|^2 = 1.38 \times 10^{-6}\,.$$

We have calculated this quantity for 23 values between $\tilde{\omega}_{2,q_{z2}} = 0.024$ ($B = 0.13\,\mathrm{T}$) and 0.2 (1.1 T). An $ax^b$ fit to these data points reveals a proportionality $\propto B^6$, figure 7.4,

$$\begin{aligned} & |\tilde{H}_{\downarrow\uparrow,EPC}^{11,(2,\tilde{q}_{z2})}(\tilde{\omega})|^2 \propto \tilde{\omega}^6 \propto B^6 \quad (\tilde{\omega} \in [0.024,\, 0.2])\,, \qquad (7.16) \\ \Rightarrow \quad & |\tilde{H}_{\downarrow\uparrow,EPC}^{11,(2,\tilde{q}_{z2})}(\tilde{\omega})|^2 = 1.22 \times 10^{-6} \times (B[\,\mathrm{T}])^6 \quad (W = 30\,\mathrm{nm},\, B \in [0.13\,\mathrm{T},\, 1.1\,\mathrm{T}])\,. \end{aligned}$$

[7] The phonon state must be respected, too: $\left(\langle n, 1_{\alpha,-q_{z\alpha}}|H_{EPC}^{(\alpha,q_{z\alpha})}|k,0\rangle\right)^* = \langle k, 1_{\alpha,+q_{z\alpha}}|H_{EPC}|n,0\rangle$.

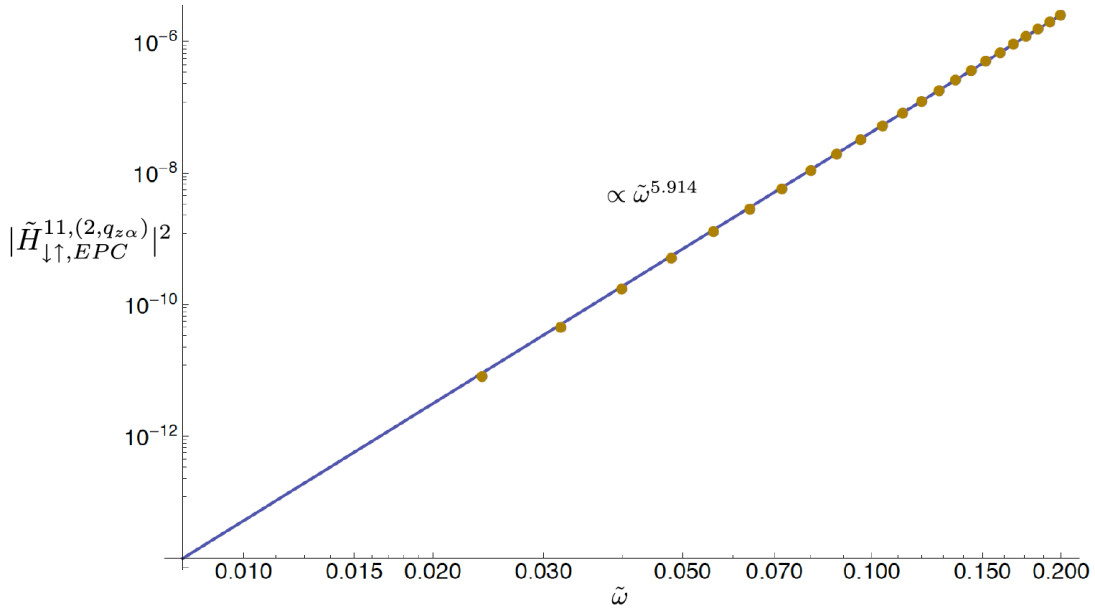


Figure 7.4.: This log-log plot illustrates agreement of the $\tilde{\omega}^6$ fit with data points. For $\tilde{\omega} < 0.024$ our numerical output is zero, thus prohibiting further numerical analysis. For $\tilde{\omega} \gg 0.2$ the behavior differs from $\tilde{\omega}^6$.

Another $B$-dependence arises from[8] the prefactor $\tilde{\omega}^{-1}$ such that the overall magnetic field dependence of (7.15) is $B^5$. However, we emphasize that this result is a numerical fit in said interval and not analytic. In particular, the behavior changes for $\tilde{\omega} \gg 0.2$. Numerical problems prohibit further analysis for $\tilde{\omega} < 0.024$.

## 7.2. Relaxation time

In this chapter, we calculate the spin relaxation time $T_1$. As explained in section 1.1, this is the typical time scale for the relaxation between the Zeeman-split states $|\uparrow\rangle$ and $|\downarrow\rangle$. The inverse of this time is the relaxation rate $\Gamma_1 = 1/T_1$, where

$$\Gamma_1 := \frac{\mathrm{d}p_{|\uparrow\rangle\to|\downarrow\rangle}}{\mathrm{d}t}$$

is the probability per time. First, we show that it is justified to obtain $\Gamma_1$ via Fermi's Golden Rule. Then, we explicitly calculate this rate for our system and finally, we discuss the results.

[8]The normalization $N^{(2,q_{z2})}$ has no $B$-dependence for $\tilde{\omega} \in [0.024, 0.2]$, where it is constant, (6.4).

### 7.2.1. Fermi's Golden Rule

A common measure for the stability of a quantum state is its transition rate to other quantum states. The transition rate from the initial state $|i\rangle$ to a final state $|f\rangle$ is the probability per time, $\Gamma := \mathrm{d}p_{|i\rangle\to|f\rangle}/\mathrm{d}t$. Under certain conditions this rate can be calculated via Fermi's Golden Rule,

$$\Gamma = \frac{2\pi}{\hbar}|\langle f|H'|i\rangle|^2\rho(E_i)\,, \tag{7.17}$$

where $\rho(E_i)$ is the density of states at $E = E_i$ and $H'$ is a perturbation to energy eigenstates $|i\rangle$, $|f\rangle$. In the Dirac representation of quantum mechanics the time evolution of states is determined by the perturbation $H'$. Projecting the time-evolved initial state $|i(t)\rangle$ onto $|f\rangle$ leads to (7.17). A full derivation of Fermi's Golden Rule can be found in e.g. [Burkard (QII), Nolting 5/2]. The rule is justified under the following conditions:

- After switching it on, the perturbation $H'(t)$ must be constant: $H'(t) = \theta(t)H'$.
- The spectrum of final states must satisfy the continuum approximation,

  $$\Delta E_f > \frac{2\pi\hbar}{t} \gg \delta E_f\,,$$

  where $\Delta E_f = |E_i - E_f|$ is the energy difference between initial and final state, $\delta E_f$ is the energy spacing of final states and $t$ is the elapsed time since switching on the perturbation. For sufficiently long times the middle term becomes basically zero such that the left inequality even allows for transitions between degenerate states ($\Delta E_f = 0$). The right inequality demands a (quasi-) continuous spectrum of final states. A finite $\delta E_f$, which is always the case in finite systems, gives an upper bound for $t$ and therefore for the timescale on which the theory is valid.

We want to apply Fermi's Golden Rule to spin relaxation $|\uparrow\rangle \to |\downarrow\rangle$. For admixture mechanism assisted relaxation of the Zeeman energy into the lattice, we consider first order spin-orbit admixed electron states and phonon states. Then, the perturbation corresponds to electron-phonon coupling and the density of states refers to phonon states,

$$|i\rangle \to |n\uparrow^{(1)}, N_i\rangle\,, \quad |f\rangle \to |n\downarrow^{(1)}, N_f\rangle\,, \quad H'(t) \to H_{EPC}(t)\,, \quad \rho(E) \to \frac{D(\omega)}{\hbar}\,.$$

We check the above conditions:

- The perturbation $H_{EPC}(t)$ contains operators $b^{(\dagger)}_{\alpha,\pm q}(t) \propto e^{\pm i\omega_{\alpha,q}t}$. Single phonon processes, which we deal with here, involve only one such operator. Its phase and therefore its time dependence can be omitted, since only the amplitude of the matrix element in (7.17) matters. ✓
- Since the spin-orbit mixed electron states are discrete the phonon states must be continuous. The assumption of a finite ribbon length and periodic boundaries leads to discrete phonon wavenumbers thus allowing for correct counting of the phonon modes. Discrete wavenumbers lead to a discrete phonon spectrum. However, the rate $\Gamma$ is independent of the ribbon length $L$, such that it is the same for any value of $L$, (7.19). In a gedankenexperiment, we can assume $L \to \infty$, corresponding to a continuous phonon spectrum. ✓

With these conditions satisfied, we can use (7.17) to calculate the relaxation rate. All phonon modes at the Zeeman energy represent parallel channels via which the spin can relax, figure 7.3, and these rates add up,

$$\begin{aligned}\Gamma_1 &= \sum_{\alpha,\pm q_{z\alpha}} \frac{2\pi}{\hbar} \left|\langle n\downarrow^{(1)}, 1_{\alpha,\pm q_{z\alpha}}|H_{EPC}|n\uparrow^{(1)},0\rangle\right|^2 \frac{D(\omega_{\alpha,q_{z\alpha}})}{\hbar} \\ &= \sum_{\alpha,q_{z\alpha}} \frac{4\pi}{\hbar} \left|\langle n\downarrow^{(1)}, 1_{\alpha,-q_{z\alpha}}|H_{EPC}|n\uparrow^{(1)},0\rangle\right|^2 \frac{D(\omega_{\alpha,q_{z\alpha}})}{\hbar}\,, \end{aligned} \tag{7.18}$$

where we assume initial phonon vacuum ($|N_i\rangle = |0\rangle$). As above, $\pm q_{z\alpha}$ are those wavenumbers, where branch $\alpha$ satisfies $\hbar\omega_{\alpha,q_{z\alpha}} = g\mu_B B$. Due to symmetry, this condition is always satisfied for both signs and the contributions of $\pm q_{z\alpha}$ are identical[9].

## 7.2.2. Relaxation time and magnetic field dependence

The relaxation time is given by the inverse of (7.18). The remaining task is merely to evaluate this expression. As argued above, only the dispersion branches $\alpha = 1, 2$ are available for conventional Zeeman splittings and the $\alpha = 1$ branch cannot induce spin flips since the deformation potential cancels out over the ribbon width. Due to monotony, $q_{z\alpha}$ is unique for $\alpha = 2$ (figure 7.3), such that (7.18) simplifies to

$$\begin{aligned}\Gamma_1 &= \frac{4\pi}{\hbar^2} \left|\langle n\downarrow^{(1)}, 1_{2,-q_{z2}}|H_{EPC}|n\uparrow^{(1)},0\rangle\right|^2 D(\omega_{2,q_{z2}}) \\ &= \frac{4\pi}{\hbar^2}\left(\frac{g_D\lambda_R}{\hbar v_F\pi/3}\right)^2 \frac{\hbar}{2\,\rho LW\omega_{2,q_{z2}}} |\tilde{H}^{nn,(2,-\tilde{q}_{z2})}_{\downarrow\uparrow,EPC}|^2 \sqrt{\frac{\rho}{Eh}}\frac{L}{\pi}\left.\frac{\mathrm{d}\tilde{\omega}}{\mathrm{d}\tilde{q}}\right|_{\tilde{\omega}_{2,\tilde{q}_{z2}}} \\ &= \frac{18}{g\mu_B BW}\left(\frac{g_D\lambda_R}{\hbar v_F\pi}\right)^2 |\tilde{H}^{nn,(2,-\tilde{q}_{z2})}_{\downarrow\uparrow,EPC}|^2 \frac{1}{\sqrt{\rho Eh}}\left.\frac{\mathrm{d}\tilde{\omega}}{\mathrm{d}\tilde{q}}\right|_{\tilde{\omega}_{2,\tilde{q}_{z2}}}\,. \end{aligned} \tag{7.19}$$

In the second step, we have substituted (5.23) and (7.15). Indeed, the ribbon length cancels out, as required for a continuous spectrum of final states. This expression contains three quantities that have been determined numerically:

1. The density of states $\mathrm{d}\tilde{\omega}/\mathrm{d}\tilde{q}|_{\tilde{\omega}}$. It is constant, $\mathrm{d}\tilde{\omega}/\mathrm{d}\tilde{q} = 1$, in the interval $\tilde{\omega} \in [0, 2]$, see figure 7.3 and equation (5.23). (Figure 5.7 shows the total density of states but here, we mean only the phonon branch $\alpha = 2$.)

2. The squared matrix element $|\tilde{H}^{nn,(2,-\tilde{q}_{z2})}_{\downarrow\uparrow,EPC}|^2$, for which we find a $\propto \tilde{\omega}^6$-dependence for $\tilde{\omega} \in [0.024, 0.2]$, see (7.16). For $\tilde{\omega} > 0.2$, the behavior is below $\tilde{\omega}^6$, which we use as an upper bound.

3. The numerical normalization $N^{(2,-q_{z2})}$ is absorbed in the phonons and hence in the matrix element. For $\tilde{\omega} \in [0, 0.2]$, it is constant, (6.4) and figure 6.1. Up to $\tilde{\omega} = 2$ there is only a deviation from this constant of 30%.

[9] As explained below (7.14) the matrix elements differ by a phase but have the same amplitude.

Despite the second constraint, we extrapolate the results to $\tilde{\omega} \in [0; 0.2]$. For $\tilde{\omega} \in [0.2; 2]$, the non-constant behavior of the normalization is overcompensated by the $\tilde{\omega}^6$-dependence of the squared matrix element such that we give an upper (lower) bound for the relaxation rate (time) in this interval. After putting in all the constants ($g_D = 25\,\mathrm{eV}$ and[10] $\lambda_R = 20\,\mu\mathrm{eV}$), we find

$$\begin{aligned} \Gamma_1 &= \frac{230\,(B[\,\mathrm{T}])^5}{W[\,\mathrm{nm}]}\,\mathrm{s}^{-1} \\ T_1 &= \Gamma_1^{-1} = \frac{W[\,\mathrm{nm}]}{230\,(B[\,\mathrm{T}])^5}\,\mathrm{s}\,, \end{aligned}$$

where $W$ and $B$ must satisfy $W[\,\mathrm{nm}] \times B[\,\mathrm{T}] \in [0; 340]$ in order to conform $\tilde{\omega} \in [0; 2]$. In table 7.1, we list the relaxation rate $\Gamma_1(W, B)$ and time $T_1(W, B)$ for several valid combinations of these parameters. Plots for $W = 30\,\mathrm{nm}$, $B = 1\,\mathrm{T}$ and for $W = 100\,\mathrm{nm}$, $B = 0.2\,\mathrm{T}$ are shown in figure 7.5.

| $W[\,\mathrm{nm}]$ | $B[\,\mathrm{T}]$ | $\Gamma_1[\,\mathrm{s}^{-1}]$ | $T_1[\,\mathrm{s}]$ |
|---|---|---|---|
| 10 | 0.5 | $720 \times 10^{-3}$ | 1.4 |
| 10 | 1 | 23 | $43 \times 10^{-3}$ |
| 10 | 3 | $5.6 \times 10^{3}$ | $180 \times 10^{-6}$ |
| 10 | 10 | $< 2.3 \times 10^{6}$ | $> 430 \times 10^{-9}$ |
| 30 | 0.2 | $2.5 \times 10^{-3}$ | 410 |
| 30 | 0.5 | $240 \times 10^{-3}$ | 4.2 |
| 30 | 1 | 7.7 | $130 \times 10^{-3}$ |
| 30 | 10 | $< 770 \times 10^{3}$ | $> 1.3 \times 10^{-6}$ |
| 100 | 0.1 | $23 \times 10^{-6}$ | $43 \times 10^{3}$ |
| 100 | 0.3 | $5.6 \times 10^{-3}$ | 180 |
| 100 | 1 | $< 2.3$ | $> 430 \times 10^{-3}$ |
| 100 | 3 | $< 560$ | $> 1.8 \times 10^{-3}$ |
| 200 | 0.2 | $< 370 \times 10^{-6}$ | $> 2.7 \times 10^{3}$ |
| 200 | 0.5 | $< 36 \times 10^{-3}$ | $> 28$ |
| 200 | 1 | $< 1.15$ | $> 870 \times 10^{-3}$ |
| 200 | 1.5 | $< 8.7$ | $> 110 \times 10^{-3}$ |

Table 7.1.: Relaxation rates and times for different parameters $W$, $B$. Upper (lower) bounds for the relaxation rate (time) are indicated with "<" (">"). Due to the $B^5$-dependence the relaxation rate is tunable over about ten magnitudes for a fixed width. The width, that is, the design of the device, also affects the relaxation.

[10]The Rashba coupling is proportional to the electric field, $\lambda_R = 5\,\mu\mathrm{eV} \times E[\,\mathrm{V/nm}]$, and a typical value for the electric field induced by a substrate is $1\,\mathrm{V/nm}$, [Gmitra (2009)]. Since an additional gate voltage might be applied, we assume $E = 4\,\mathrm{V/nm}$.

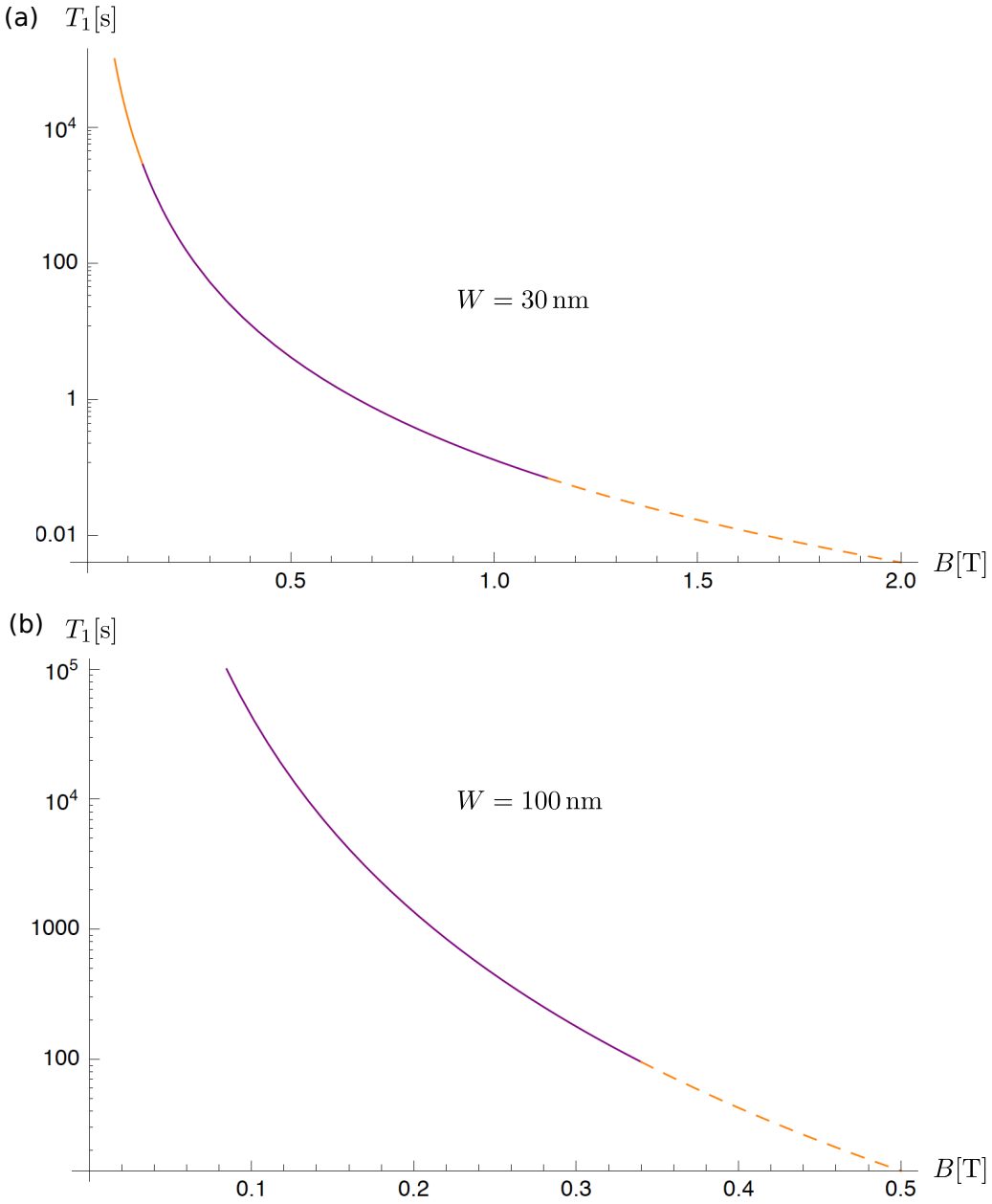


Figure 7.5.: Plot of the relaxation time (logarithmic axis) for two ribbon widths: $W = 30\,\mathrm{nm}$ (a) and $W = 100\,\mathrm{nm}$ (b). Our numerical results correspond to the purple section, which we extrapolated to smaller values (solid orange section). The dashed orange section is a lower bound for the relaxation time for higher magnetic fields. Due to other physical effects, we expect our theory to be invalid beyond $10^5\,\mathrm{s}$.

# 8. Conclusion and Outlook

In this final chapter, we summarize the above work and point out the most important results, which encourage a further study of this system.

## 8.1. Conclusion

Among other requirements, a quantum computer requires long coherence times. A spintronics implementation appears promising because of the convenience and versatility of solid state physics, proven in classical electronics, and the prospect of long coherence times. Spin qubits in graphene QD are a specific spintronics implementation with additional benefits in qubit coherence and coupling of distant qubits. In carbon, nuclear spin effects are weaker than in conventional semiconducting materials (e.g. GaAs) such that spin-relaxation via spin-phonon coupling is important.

In chapter 2, the electronic properties of graphene have been reviewed. In particular the quasi-relativistic electronic behavior, pseudo-spin, which refers to the two atoms per unit cell and the Klein paradox. The spin-orbit hamiltonian has been derived from the orbital configuration[1], whereby it has become clear that the form of the hamiltonian depends on the lattice orientation, similarly to the tight-binding hamiltonian. All calculations have been done with the orientation as depicted in figure 2.1 which has led to a consistent form of tight-binding and spin-orbit hamiltonians ((2.8) and (3.5)). As a byproduct of these calculations, we have obtained the energy level diagram of the $n = 2$ atomic shell of carbon, which in graphene forms an $sp_2$ hybrid and decoupled $p_z$ states. Degenerate bonding and antibonding $p_z$ states explain the vanishing gap at the Fermi energy for bulk graphene, figure 3.2. For a quasi-one-dimensional graphene ribbon with armchair edges, the electron wavefunction must vanish at the edges on both lattice sites and this leads, depending on the number of atoms along the width, to gapped and ungapped graphene. While ungapped graphene makes it hard to confine electrons due to the Klein paradox, gapped graphene like an armchair GNR allow for confinement and hence for electrostatic QD. The energy spectrum of such electrostatically confined electrons has been derived. There are infinitely many transverse (that is with respect to the ribbon width) excitations, each of which supports a finite series of longitudinal excitations, depending on confinement parameters. However, the energy increases rapidly for higher transverse excitations such that usually only the lowest series will be relevant.

By means of the continuum model we have derived for the first time the dispersion and

[1] We have not included the $d$-orbitals, however. As a consequence, we have not derived the coupling constants but use those of Gmitra et. al, who respect the $d$-orbitals, [Gmitra (2009)].

explicit form of in-plane and out-of-plane acoustic phonons at the zone center, where atomic distances are negligible with respect to the wavelength. With periodic boundaries in the longitudinal direction, the obtained PDE that describe the motion simplify to ODE in the transverse direction. Free boundaries in the transverse direction correspond to minimal free energy for the out-of-plane modes and a vanishing of certain components of the stress tensor for in-plane modes. In agreement with classical experience, we have found infinitely many transverse excitations for the out-of-plane. In contrast to bulk, where the dispersion at the zone center is quadratic, the lowest mode features a linear behavior that is due to the boundary conditions. This leads to finite density of states for zero energy. For large wavenumbers all modes behave like in bulk. This has been expected as the finite ribbon width appears like bulk for sufficiently small wavelengths. The in-plane modes form vector fields as the boundary conditions mix longitudinal and transversal modes. Still, we have managed to identify modes with dominant longitudinal/transverse character and derived the longitudinal and transverse sound velocity associated with these modes. These values depend on elastic constants that have not been settled, yet. For reasonable choices of these constants, the sound velocities compare well with literature values for bulk graphene and carbon nanotubes (table 5.2). There are two modes that originate from zero energy: a flat one and a linear one. Due to the flat mode the density of states diverges for zero energy. Again, all modes behave like bulk (i.e. linear) for sufficiently large wavenumbers.

These classical modes have been quantized by virtue of the right orthonormality relations. While orthogonality is an inherent property of the PDE, normalization has been achieved numerically. We have derived the normal coordinates and the associated Lagrangian, hamiltonian and canonical momentum and have quantized coordinate and momentum in terms of phonon creation and annihilation operators. While this procedure works for in-plane as well as for out-of-plane modes, we have restricted it to the in-plane modes, here, since the deformation potential has no lowest-order contributions from out-of-plane modes. The deformation potential is one of several electron-phonon coupling mechanisms and the underlying effect is that a phonon causes a dilation or compression of the material. This changes the local charge density and therefore the coulomb potential that influences electrons. We have expressed this coupling mechanism as an operator in terms of ribbon phonon creators and annihilators and we have confirmed its hermiticity.

The deformation potential does not couple to electron spin directly. A combination of electron-phonon coupling and spin-orbit coupling, however, allows for an effective spin-phonon coupling mechanism via which the Zeeman energy can be released. In the admixture mechanism proposed by Khaetskii and Nazarov, spin-orbit coupling perturbs the electronic states such that the orbital states mix. Coupling to these mixed orbital states, the deformation potential can cause a spin flip, figure 7.1. The mixing of the orbital states, which correspond to the energy levels in the QD that had been discussed beforehand, and the coupling of the deformation potential have been treated analytically and in detail. Although there is also an effect from intrinsic spin-orbit coupling to the mixing of electronic states it only occurs in higher order. For a preliminary result we have focused on lowest order effects, that is, Rashba-type spin-orbit coupling and the series of lowest transverse excitation, figure 7.2. It has turned out that, in this series, only every second second longitudinal excitation contributes to the mixing of the state, which we

have calculated in first order perturbation theory. In particular, the state with opposite spin and same longitudinal excitation (i.e. the same orbital state) does not contribute. Since all non-zero contribution are weighted with the inverse of the energy difference this strongly suppresses the admixing. An even further suppression arises from the Van Vleck cancellation, which we have expected since the electronic states conserve time-reversal symmetry[2] [Van Vleck (1940)]. In addition, we have assumed phononic vacuum and the creation of only one phonon that absorbs the Zeeman energy. For conventional magnetic fields ($\approx 1\,\mathrm{T}$) only modes on the two lowest branches of the in-plane dispersion are available. For modes on the flat branch, however, the local deformation potential cancels out over the ribbon width such that only modes on the linear branch contribute to relaxation via this mechanism. Due to the linearity of this branch, the density of states is small compared to the flat branch, which further suppresses spin relaxation.

In order to calculate the relaxation rate via Fermi's Golden Rule we had to ensure a continuous spectrum of final states. Since the ribbon length cancels out, the rate is the same for a ribbon of arbitrary length. In particular, a sufficiently long ribbon can be assumed such that the continuum approximation is satisfied. The resulting relaxation rate goes inversely with the ribbon width and thus, in principle, allows for tailor-made devices. Magnetic fields can be adjusted well over a range of two magnitudes such that the $B^5$-dependence of the rate leads to relaxation times that differ by about ten magnitudes. The behavior with $B^5$ applies for a certain parameter interval, where relaxation times range from $180\,\mu\mathrm{s}$ to $43 \times 10^3 s$, table 7.1. For parameters beyond our numerically available regime, we have given a lower bound for the relaxation time.

In total, the entire theory for spin relaxation in GNR has been introduced and demonstrated for one relaxation mechanism in lowest order. In this case, spin relaxation is efficiently suppressed by several effects:

- Only every second longitudinal excitation contributes to spin-orbit admixing.
- The electronic states conserve time-reversal symmetry, leading to Van Vleck cancellation.
- We have assumed phononic vacuum. This is justified for sufficiently low temperatures.
- For conventional magnetic fields only one dispersion branch contributes to the deformation potential and this branch has a low density of states.

All values are satisfactory for the third DiVincenzo criterion and this motivates a more detailed investigation of this system [DiVincenzo (1999), Loss (1998)]. With the basics understood in detail, we expect further studies to proceed conveniently.

[2] This symmetry is related to the degeneracy of the Dirac points $K$ and $K'$, which is indeed unbroken in this system.

## 8.2. Outlook

The simplifying assumptions in this work have led to results that encourage a more realistic model. As for the ribbon phonons, we have assumed free boundaries, that is, freestanding graphene. In reality, true freestanding graphene cannot exist because of divergent long-range interactions in two-dimensional lattices, thus implying the necessity of a substrate or fixed boundaries (see comment in section 1.3). This affects electron-phonon coupling and the density of states, and consequently the relaxation rate. Moreover, the assumption of phononic vacuum can be generalized to non-zero phonon occupation numbers via Bose statistics with a finite temperature: $N_\omega = 1/(e^{\hbar\omega/k_B T} - 1)$. We have focused on single phonon processes but in higher order there are also multiple phonon processes and the out-of-plane modes contribute to the deformation potential.

The dominant contributions to the admixing of electronic states come from the series of lowest transverse excitation and we have neglected all higher series. While we do not expect these contributions to change the rate by magnitudes they should be included in a more general calculation. This also applies for unbound electronic states, which travel freely across the ribbon. It might turn out, however, that there is no net effect from these states for symmetry reasons. Intrinsic spin-orbit coupling does increase the admixture of states as a higher order effect.

Here, we have focused on the deformation potential but spin can relax via various mechanisms and this might change the rate significantly. Predictions for circular QD in bulk graphene indicate strong contributions from bond length change and direct spin-phonon deflection coupling to out-of-plane modes, [Struck (2010)]. All these effects add up as parallel relaxation channels and thus increase the relaxation rate.

On the other hand, any theoretical model can only be confirmed by experiment and therefore progress in the fabrication of graphene nanodevices is highly desirable, too. In addition, several material parameters (e.g. elastic constants) remain to be settled experimentally. The suitability of GNR for spintronics devices remains to be determined by future work.

# A. Continuum model

The continuum model [Landau & Lifschitz, Chaikin & Lubensky] can be applied for acoustic modes near the center of the Brillouin zone, that is with small wavenumber. The atomic structure becomes negligible for wavelengths much larger than the length of the lattice vectors. The notion of continuous material does not allow for optical modes as different atoms within the same unit cell need to vibrate against each other for these.

### Strain tensor

External forces deform solid bodies to a certain extent thus changing their shape as well as their volume. A point inside the undeformed body, described by the position vector $\vec{r}$, shall be displaced to $\vec{r'}$ after the deformation. Then

$$\vec{u} = \vec{r'} - \vec{r} \tag{A.1}$$

is called the *displacement vector* with components $u_i$, which usually depend on the position. The deformation of the entire object is known if $\vec{u}(\vec{r})$ can be determined for the whole body.

With $\mathrm{d}x_i$ we denote the components of the vector connecting two infinitesimally close volume elements prior to the deformation. In first order they change to

$$\mathrm{d}x_i' = \mathrm{d}x_i + \mathrm{d}u_i \approx \mathrm{d}x_i + \frac{\partial u_i}{\partial x_j}\mathrm{d}x_j \tag{A.2}$$

after the deformation. Accordingly, the distance between the points changes from

$$\mathrm{d}l = \sqrt{\mathrm{d}x_1^2 + \mathrm{d}x_2^2 + \mathrm{d}x_3^2}$$

to

$$\mathrm{d}l' = \sqrt{\mathrm{d}x_1'^2 + \mathrm{d}x_2'^2 + \mathrm{d}x_3'^2}\,.$$

Taking the square of the last two equations results in $\mathrm{d}l^2 = \mathrm{d}x_i^2$ and

$$\begin{aligned} \mathrm{d}l'^2 &= \mathrm{d}x_i'^2 = (\mathrm{d}x_i + \mathrm{d}u_i)^2 = \mathrm{d}x_i^2 + 2\mathrm{d}x_i\mathrm{d}u_i + \mathrm{d}u_i^2 \\ &\overset{(A.2)}{\approx} \mathrm{d}l^2 + 2\frac{\partial u_i}{\partial x_k}\mathrm{d}x_k\mathrm{d}x_i + \frac{\partial u_i}{\partial x_k}\frac{\partial u_i}{\partial x_l}\mathrm{d}x_k\mathrm{d}x_l\,. \end{aligned}$$

Using

$$\frac{\partial u_i}{\partial x_k}\mathrm{d}x_i\mathrm{d}x_k = \frac{\partial u_i}{\partial x_k}\mathrm{d}x_k\mathrm{d}x_i \overset{i\leftrightarrow k}{=} \frac{\partial u_k}{\partial x_i}\mathrm{d}x_i\mathrm{d}x_k$$

the second term can be written as

$$\left(\frac{\partial u_i}{\partial x_k} + \frac{\partial u_k}{\partial x_i}\right) \mathrm{d}x_i \mathrm{d}x_k \,,$$

and we find

$$\mathrm{d}l'^2 \approx \mathrm{d}l^2 + 2u_{ik}\mathrm{d}x_i\mathrm{d}x_k \,, \tag{A.3}$$

where

$$u_{ik} = \frac{1}{2}\left(\frac{\partial u_i}{\partial x_k} + \frac{\partial u_k}{\partial x_i} + \frac{\partial u_l}{\partial x_i}\frac{\partial u_l}{\partial x_k}\right)$$

is defined as the *strain tensor*. As a symmetric tensor, $u_{ik}$ can be diagonalized with $u^{(1)} := u_{11}$, $u^{(2)} := u_{22}$ and $u^{(3)} := u_{33}$ being the eigenvalues of $u_{ik}$. Then (A.3) takes the form

$$\begin{aligned} \mathrm{d}l'^2 &\approx (\delta_{ik} + 2u_{ik})\mathrm{d}x_i\mathrm{d}x_k \\ &= (1 + 2u^{(1)})dx_1^2 + (1 + 2u^{(2)})\mathrm{d}x_2^2 + (1 + 2u^{(3)})\mathrm{d}x_3^2 \,. \end{aligned}$$

Each summand corresponds to the length shift along one of the three orthogonal principal axes. For example the length element $\mathrm{d}x_1$ is elongated or compressed to $\mathrm{d}x_1' = \sqrt{1 + 2u^{(1)}}\mathrm{d}x_1$. Consequently the relative length shifts $(\mathrm{d}x_i' - \mathrm{d}x_i)/\mathrm{d}x_i$ along the principal axes are $\sqrt{1 + 2u^{(i)}} - 1$.

Usually, deformations throughout the body are small, that is, relative length shifts resulting from such a deformation are small compared to unity. In this case second order terms can be neglected such that the relative length shifts become

$$\frac{\mathrm{d}x_i' - \mathrm{d}x_i}{\mathrm{d}x_i} = \sqrt{1 + 2u^{(i)}} - 1 \approx u^{(i)} \,, \tag{A.4}$$

and the strain tensor can be written as

$$u_{ik} \approx \frac{1}{2}\left(\frac{\partial u_i}{\partial x_k} + \frac{\partial u_k}{\partial x_i}\right) . \tag{A.5}$$

The volume element is given by $\mathrm{d}V = \mathrm{d}x_1\mathrm{d}x_2\mathrm{d}x_3$ and with (A.4) the deformed volume element is

$$\begin{aligned} \mathrm{d}V' &= \mathrm{d}x_1'\mathrm{d}x_2'\mathrm{d}x_3' = (1 + u^{(1)})\mathrm{d}x_1(1 + u^{(2)})\mathrm{d}x_2(1 + u^{(3)})\mathrm{d}x_3 \\ &= (1 + u^{(1)})(1 + u^{(2)})(1 + u^{(3)})\mathrm{d}V \,. \end{aligned}$$

Respecting only first order terms again,

$$\mathrm{d}V' \approx (1 + u^{(1)} + u^{(2)} + u^{(3)})\mathrm{d}V \,,$$

such that the relative volume change becomes

$$\frac{\mathrm{d}V' - \mathrm{d}V}{\mathrm{d}V} \approx u^{(1)} + u^{(2)} + u^{(3)} = u_{ii} \,. \tag{A.6}$$

**Stress tensor**

In a non-deformed body all molecules are arranged in their mechanical equilibrium positions, that is, all internal forces acting on a volume element sum up to zero. External forces will change the arrangement of molecules in the body and thus cause a deformation. The internal tensions resulting from this deformation seek to restore the non-deformed arrangement and counteract the external forces. The effective internal force acting on a certain volume can be denoted as

$$\int \vec{F} \mathrm{d}V \,, \tag{A.7}$$

where said volume is integrated and $\vec{F}$ is the force per volume such that the force acting on $\mathrm{d}V$ is $\vec{F}\mathrm{d}V$. By introducing the *stress tensor* $\sigma_{ik}$ via

$$F_i = \frac{\partial \sigma_{ik}}{\partial x_k} \tag{A.8}$$

and using Gauss' Law[1] it is possible to rewrite (A.7) as

$$\int F_i \mathrm{d}V = \int \frac{\partial \sigma_{ik}}{\partial x_k} \mathrm{d}V = \oint \sigma_{ik} \mathrm{d}f_k \,.$$

We notice that $\sigma_{ik}\mathrm{d}f_k$ is the $i$-th component of the force acting on the surface element $\mathrm{d}f$. Consider a surface normal to the $x$-axis. Then $\sigma_{xx}$ is the force per surface unit that acts normal to this surface and $\sigma_{yx}$ and $\sigma_{zx}$ are the forces acting tangential to it, see figure A.1.

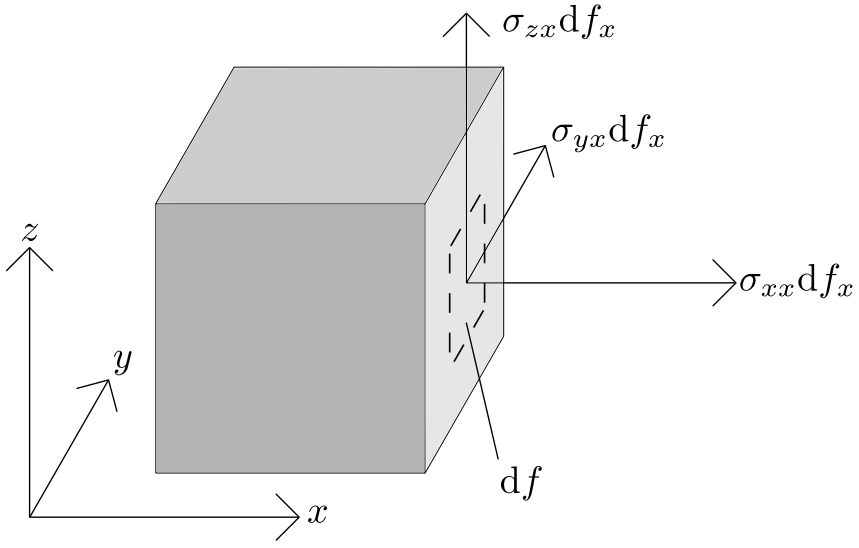


Figure A.1.: By virtue of Gauss' law the force acting on volume element $\mathrm{d}V$, can be expressed in terms of the strain tensor $\sigma_{ik}$. The $i$-th component of the force acting on the surface element $\mathrm{d}f$ is $\sigma_{ik}\mathrm{d}f_k$.

[1]The integral of a gradient over a volume can be replaced by an integral over the surface enclosing said volume: $\int \frac{\partial h_i}{\partial x_i}\mathrm{d}V = \oint h_i \mathrm{d}f_i$, where $\mathrm{d}\vec{f}$ is a vector normal to the enclosing surface.

In mechanical equilibrium, all internal tensions on a volume element must cancel each other, that is

$$\frac{\partial \sigma_{ik}}{\partial x_k} = F_k = 0\,.$$

We denote the external force per surface element of the body with $\vec{P}$ such that the surface element $\mathrm{d}f$ experiences the force $\vec{P}\mathrm{d}f$. This force deforms the body until it is counteracted by internal strain $\sigma_{ik}\mathrm{d}f_k$. With such boundary conditions, equilibrium is achieved when $P_i\mathrm{d}f = \sigma_{ik}\mathrm{d}f_k$. Using $\mathrm{d}f_k = \eta_k\mathrm{d}f$, where $\eta_k$ is the unit vector normal to the surface, this condition becomes

$$\sigma_{ik}\eta_k = P_i\,. \tag{A.9}$$

Consider a small deformation $\delta u_i$. The required mechanical energy per volume is $\delta R = F_i\delta u_i = \frac{\partial \sigma_{ik}}{\partial x_k}\delta u_i$. Integrating the entire volume yields

$$\int \delta R\mathrm{d}V = \int \frac{\partial \sigma_{ik}}{\partial x_k}\delta u_i \mathrm{d}V\,,$$

the total work required for the deformation of the body. Using partial integration and Gauss' Law, we find

$$\int \delta R\mathrm{d}V = \oint \sigma_{ik}\delta u_i \mathrm{d}f_k - \int \sigma_{ik}\frac{\partial \delta u_i}{\partial x_k}\mathrm{d}V\,.$$

The first term vanishes for $\sigma_{ik} = 0$ or if an infinite body with $\delta u_i = 0$ at infinity is assumed. Also making use of the symmetry[2] of $\sigma_{ik}$ the above can be written as

$$\begin{aligned}\int \delta R\mathrm{d}V &= -\frac{1}{2}\int \sigma_{ik}\left(\frac{\partial \delta u_i}{\partial x_k} + \frac{\partial \delta u_k}{\partial x_i}\right)\mathrm{d}V = -\frac{1}{2}\int \sigma_{ik}\delta\left(\frac{\partial u_i}{\partial x_k} + \frac{\partial u_k}{\partial x_i}\right)\mathrm{d}V \\ &= -\int \sigma_{ik}\delta u_{ik}\mathrm{d}V\,,\end{aligned}$$

such that $\delta R = -\sigma_{ik}\delta u_{ik}$. The differential internal energy per volume, $\mathrm{d}E$ equals the difference between the thermal energy absorbed by the volume element and the mechanical work performed by its internal tensions,

$$\mathrm{d}E = T\mathrm{d}S - \mathrm{d}R = T\mathrm{d}S + \sigma_{ik}\mathrm{d}u_{ik}\,. \tag{A.10}$$

A Legendre transformation in $T$ and $S$ turns the internal energy into the free energy,

$$\mathrm{d}F = \mathrm{d}(E - TS) = \mathrm{d}E - S\mathrm{d}T - T\mathrm{d}S = -S\mathrm{d}T + \sigma_{ik}\mathrm{d}u_{ik}\,. \tag{A.11}$$

From the thermodynamical potentials (A.10) and (A.11) it is easy to derive the stress tensor:

$$\begin{aligned}\sigma_{ik} &= \left(\frac{\partial E}{\partial u_{ik}}\right)_S\,, \\ \sigma_{ik} &= \left(\frac{\partial F}{\partial u_{ik}}\right)_T\,.\end{aligned} \tag{A.12}$$

Below, we concentrate on the stress tensor in terms of the free energy.

[2]The stress tensor $\sigma_{ik}$ is not unambiguously fixed by (A.8) but allows for the addition of a gradient $\frac{\partial \chi_{ikl}}{\partial x_l}$ (where $\chi_{ikl} = -\chi_{ilk}$). By virtue of this gradient the stress tensor can be symmetrized. For more details we refer the reader to [Landau & Lifschitz].

**The elastic energy functional**

To proceed with our calculations we expand the free energy per volume, $F(T, u_{ik})$, in powers of $u_{ik}$. Since the free energy is a scalar each of its summand must be a scalar, too. The temperature is assumed to remain constant during the deformation, which is necessary to exclude thermal expansion. Then, starting from mechanical equilibrium, $u_{ik} = 0$ implies $\sigma_{ik} = 0$ and therefore

$$\frac{\partial F}{\partial u_{ik}} \overset{(A.12)}{=} 0\,,$$

such that no linear terms appear in our expansion (as expected for mechanical equilibrium). Only two independent, invariant scalars of second order can be formed from the strain tensor, namely e. g. the square of the trace, $u_{ii}^2$, and the sum[3] of all squared elements, $u_{ik}^2$. For small deformations higher order terms can be neglected and we find

$$F = \frac{\lambda_{3D}}{2} u_{ii}^2 + \mu_{3D} u_{ik}^2\,. \tag{A.13}$$

The energy scale is chosen in such a way that $F = 0$ for the non-deformed body and the quantities $\lambda_{3D}$ and $\mu_{3D}$ are Lamé's constants for a three-dimensional body. It is common to express these constants in terms of Young's modulus $\mathcal{E}$ and Poisson's ratio $\sigma$ which are a measure for the stiffness of the material and its transverse contraction upon axial elongation, respectively:

$$\lambda_{3D} = \frac{\mathcal{E}\sigma}{(1-2\sigma)(1+\sigma)}\,, \quad \mu_{3D} = \frac{\mathcal{E}}{2(1+\sigma)}\,. \tag{A.14}$$

With these expressions, (A.13) becomes

$$\begin{aligned} F &= \frac{\mathcal{E}\sigma}{2(1-2\sigma)(1+\sigma)} u_{ii}^2 + \frac{\mathcal{E}}{2(1+\sigma)} u_{ik}^2 \\ &= \frac{\mathcal{E}}{2(1+\sigma)} \left( u_{ik}^2 + \frac{\sigma}{1-2\sigma} u_{ii}^2 \right)\,. \end{aligned} \tag{A.15}$$

This form of the free energy will be used to derive differential equations for deformations of a thin plate. The stress tensor can be expressed in terms of the strain tensor,

$$\sigma_{ik} \overset{(A.12)}{=} \frac{\partial F}{\partial u_{ik}} = \frac{\mathcal{E}}{1+\sigma} \left( u_{ik} + \frac{\sigma}{1-2\sigma} u_{ll} \delta_{ik} \right)\,,$$

[3] Note that $u_{ik}^2 = u_{ik} u_{ik} = u_{11} u_{11} + u_{12} u_{12} + \ldots$.

with the explicit components

$$\begin{aligned}
\sigma_{xx} &= \frac{\mathcal{E}}{1+\sigma}\left(u_{xx} + \frac{\sigma}{1-2\sigma}(u_{xx}+u_{yy}+u_{zz})\right) \\
&= \frac{\mathcal{E}}{(1+\sigma)(1-2\sigma)}\left((1-2\sigma)u_{xx} + \sigma(u_{xx}+u_{yy}+u_{zz})\right) \\
&= \frac{\mathcal{E}}{(1+\sigma)(1-2\sigma)}\left((1-\sigma)u_{xx} + \sigma(u_{yy}+u_{zz})\right)\,, \\
\sigma_{yy} &= \frac{\mathcal{E}}{(1+\sigma)(1-2\sigma)}\left((1-\sigma)u_{yy} + \sigma(u_{xx}+u_{zz})\right) \\
\sigma_{zz} &= \frac{\mathcal{E}}{(1+\sigma)(1-2\sigma)}\left((1-\sigma)u_{zz} + \sigma(u_{xx}+u_{yy})\right) \\
\sigma_{xy} &= \frac{\mathcal{E}}{1+\sigma}u_{xy}\,, \quad \sigma_{xz} = \frac{\mathcal{E}}{1+\sigma}u_{xz} \quad \text{and} \quad \sigma_{yz} = \frac{\mathcal{E}}{1+\sigma}u_{yz}\,.
\end{aligned} \tag{A.16}$$

**Thin plates**

If the thickness of a plate is much smaller than its width and length (like in the case of graphene) all forces can be assumed to be constant with respect to the thickness such that we are allowed to describe them with the model for a thin plate. The deformation coordinates are

$$u_x = 0\,, \quad u_y = 0 \quad \text{and} \quad u_z \approx \zeta(x,y)\,,$$

where $\zeta$ is the displacement of the "neutral" plane in the middle of the plate, as depicted in figure A.2. Due to its small thickness only very weak forces need to be applied to the

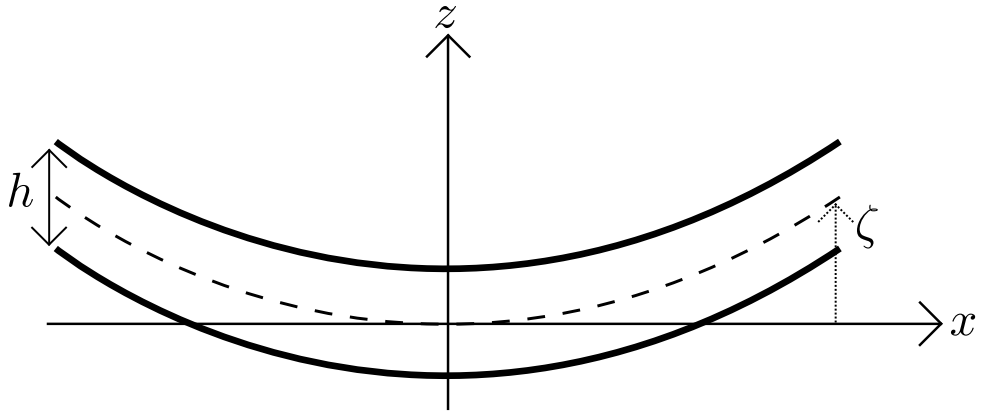


Figure A.2.: For sufficiently small thickness $h$ the out-of-plane displacement $u_z(x,y)$ is sufficiently well described by the displacement of the neutral plane in the middle of the plate, $\zeta(x,y)$.

plate surface in order to bend it. These external surface forces $\vec{P}$ can be neglected when compared to internal tensions such that $\sigma_{ik}n_k = 0$ (see (A.9)). For a small bending the surface normal vector $\vec{n}$ points along the $z$-axis, such that

$$\sigma_{xz} = \sigma_{yz} = \sigma_{zz} = 0\,.$$

These components vanish throughout the thin plate due to homogeneity. With (A.5) and (A.16) we infer

$$u_{xz} = 0 \;\Rightarrow\; \frac{\partial u_x}{\partial z} = -\frac{\partial u_z}{\partial x}\,, \quad u_{yz} = 0 \;\Rightarrow\; \frac{\partial u_y}{\partial z} = -\frac{\partial u_z}{\partial y}\,,$$
$$u_{zz} = -\frac{\sigma}{1-\sigma}(u_{xx} + u_{yy})\,. \tag{A.17}$$

For a small bending, it is sufficiently exact to replace $u_z$ by $\zeta(x, y)$. It follows that

$$\frac{\partial u_x}{\partial z} = -\frac{\partial \zeta}{\partial x}\,, \quad \frac{\partial u_y}{\partial z} = -\frac{\partial \zeta}{\partial y}\,,$$

and hence

$$u_x = -z\frac{\partial \zeta}{\partial x}\,, \quad u_y = -z\frac{\partial \zeta}{\partial y}\,,$$

where integration constants have been set to zero. The components of the strain tensor become

$$u_{xx} = -z\frac{\partial^2 \zeta}{\partial x^2}\,, \quad u_{yy} = -z\frac{\partial^2 \zeta}{\partial y^2}\,, \quad u_{xy} = -z\frac{\partial^2 \zeta}{\partial x \partial y}\,,$$
$$u_{xz} = u_{yz} = 0\,, \quad u_{zz} \overset{(A.17)}{=} \frac{\sigma z}{1-\sigma}\left(\frac{\partial^2 \zeta}{\partial x^2} + \frac{\partial^2 \zeta}{\partial y^2}\right)\,.$$

With this form of the strain tensor we write (A.15) as

$$\begin{aligned}
F &= \frac{\mathcal{E}}{2(1+\sigma)}\left(u_{ik}^2 + \frac{\sigma}{1-2\sigma}u_{ii}^2\right) \\
&= \frac{\mathcal{E}}{2(1+\sigma)}\Big((u_{xx}^2 + u_{xy}^2 + u_{xz}^2 + u_{yx}^2 + u_{yy}^2 + u_{yz}^2 + u_{zx}^2 + u_{zy}^2 + u_{zz}^2) \\
&\quad + \frac{\sigma}{1-2\sigma}(u_{xx}^2 + u_{yy}^2 + u_{zz}^2 + 2u_{xx}u_{yy} + 2u_{xx}u_{zz} + 2u_{yy}u_{zz})\Big) \\
&= \frac{\mathcal{E}z^2}{2(1+\sigma)}\left\{\left((\partial_x^2\zeta)^2 + (\partial_y^2\zeta)^2 + \frac{\sigma^2}{(1-\sigma)^2}\left(\partial_x^2\zeta + \partial_y^2\zeta\right)^2 + 2(\partial_x\partial_y\zeta)^2\right)\right. \\
&\quad + \frac{\sigma}{1-2\sigma}\left((\partial_x^2\zeta)^2 + (\partial_y^2\zeta)^2 + \frac{\sigma^2}{(1-\sigma)^2}\left(\partial_x^2\zeta + \partial_y^2\zeta\right)^2 + 2\partial_x^2\zeta\partial_y^2\zeta\right. \\
&\quad \left.\left. -2\partial_x^2\zeta\frac{\sigma}{1-\sigma}(\partial_x^2\zeta + \partial_y^2\zeta) - 2\partial_y^2\zeta\frac{\sigma}{1-\sigma}(\partial_x^2\zeta + \partial_y^2\zeta)\right)\right\} \\
&= \frac{\mathcal{E}z^2}{2(1+\sigma)}\left\{\left((\partial_x^2\zeta)^2 + (\partial_y^2\zeta)^2\right)\left(\underbrace{1 + \frac{\sigma^2}{(1-\sigma)^2} + \frac{\sigma}{1-2\sigma}\left(1 + \frac{\sigma^2}{(1-\sigma)^2} - \frac{2\sigma}{1-\sigma}\right)}_{=:\,c_1}\right)\right. \\
&\quad \left. + 2(\partial_x\partial_y\zeta)^2 + \partial_x^2\zeta\partial_y^2\zeta\left(\underbrace{\frac{2\sigma^2}{(1-\sigma)^2} + \frac{\sigma}{1-2\sigma}\left(\frac{2\sigma^2}{(1-\sigma)^2} + 2 - \frac{4\sigma}{1-\sigma}\right)}_{=:\,c_2}\right)\right\}\,.
\end{aligned}$$

The constants simplify to

$$\begin{aligned} c_1 &= \frac{(1-\sigma)^2(1-2\sigma)+\sigma^2(1-2\sigma)+\sigma(1-\sigma)^2+\sigma^3-2\sigma^2(1-\sigma)}{(1-\sigma)^2(1-2\sigma)} \\ &= \frac{1-2\sigma+\sigma^2-2\sigma+4\sigma^2-2\sigma^3+\sigma^2-2\sigma^3+\sigma-2\sigma^2+\sigma^3+\sigma^3-2\sigma^2+2\sigma^3}{1-2\sigma+\sigma^2-2\sigma+4\sigma^2-2\sigma^3} \\ &= \frac{1-3\sigma+2\sigma^2}{1-4\sigma+5\sigma^2-2\sigma^3} = \frac{1-3\sigma+2\sigma^2}{(1-3\sigma+2\sigma^2)(1-\sigma)} = \frac{1}{1-\sigma} \end{aligned}$$

and

$$\begin{aligned} c_2 &= \frac{2\sigma^2(1-2\sigma)+2\sigma^3+2\sigma(1-\sigma)^2-4\sigma^2(1-\sigma)}{(1-\sigma)^2(1-2\sigma)} \\ &= \frac{2\sigma^2-4\sigma^3+2\sigma^3+2\sigma-4\sigma^2+2\sigma^3-4\sigma^2+4\sigma^3}{(1-\sigma)(1-\sigma-2\sigma+2\sigma^2)} \\ &= \frac{2\sigma}{1-\sigma}\cdot\frac{1-3\sigma+2\sigma^2}{1-3\sigma+2\sigma^2} = \frac{2\sigma}{1-\sigma} = \frac{2-2+2\sigma}{1-\sigma} = \frac{2}{1-\sigma}-2\,. \end{aligned}$$

Then, the free energy per volume turns out to be

$$\begin{aligned} F &= z^2\frac{\mathcal{E}}{2(1+\sigma)}\left(\frac{1}{1-\sigma}\left((\partial_x^2\zeta)^2+(\partial_y^2\zeta)^2\right)+\frac{2}{1-\sigma}\partial_x^2\zeta\partial_y^2\zeta+2\left(\partial_x\partial_y\zeta\right)^2-2\partial_x^2\zeta\partial_y^2\zeta\right) \\ &= z^2\frac{\mathcal{E}}{1+\sigma}\left(\frac{1}{2(1-\sigma)}\left(\partial_x^2\zeta+\partial_y^2\zeta\right)^2+(\partial_x\partial_y\zeta)^2-\partial_x^2\zeta\partial_y^2\zeta\right)\,. \end{aligned}$$

To obtain the free energy of the whole plate we must integrate the energy density over its volume. In the $z$-direction, we integrate from $-h/2$ to $h/2$, where $h$ is the thickness of the plate. The other dimensions are integrated over the entire surface of the plate,

$$\begin{aligned} F_{Pl} &= \int F\,\mathrm{d}V \\ &= \frac{2\mathcal{E}h^3}{3\cdot 8(1+\sigma)}\iint\left(\frac{1}{2(1-\sigma)}\left(\partial_x^2\zeta+\partial_y^2\zeta\right)^2+(\partial_x\partial_y\zeta)^2-\partial_x^2\zeta\partial_y^2\zeta\right)\mathrm{d}x\,\mathrm{d}y \\ &= \frac{\mathcal{E}h^3}{24(1-\sigma^2)}\iint\left(\left(\partial_x^2\zeta+\partial_y^2\zeta\right)^2+2(1-\sigma)\left((\partial_x\partial_y\zeta)^2-\partial_x^2\zeta\partial_y^2\zeta\right)\right)\mathrm{d}x\,\mathrm{d}y \end{aligned} \tag{A.18}$$

**Out-of-plane deformations**

To find the equilibrium of the plate we have to minimize its total energy. Therefore, we first calculate the variation of the free energy (A.18). The integral consists of two terms, which we treat separately. With $\mathrm{d}f = \mathrm{d}x\,\mathrm{d}y$ and $\triangle = \partial_x^2+\partial_y^2$, the former term becomes

$$\frac{1}{2}\delta\int(\triangle\zeta)^2\,\mathrm{d}f = \int(\triangle\zeta)\,\delta\left(\triangle\zeta\right)\mathrm{d}f\,.$$

The correct prefactor will be restored later. With

$$\begin{aligned}\delta\left(\triangle\zeta\right) &= \sum_i \left(\partial_i\left(\triangle\zeta\right)\right)\delta_i = \sum_i \left(\triangle\left(\partial_i\zeta\right)\right)\delta_i = \sum_i \triangle\left(\left(\partial_i\zeta\right)\delta_i\right) - \sum_i \left(\partial_i\zeta\right)\underbrace{\left(\triangle\delta_i\right)}_{=0} \\ &= \triangle\underbrace{\sum_i \left(\partial_i\zeta\right)\delta_i}_{=\delta\zeta} = \triangle\left(\delta\zeta\right)\,,\end{aligned}$$

we infer

$$\begin{aligned}\frac{1}{2}\delta\int\left(\triangle\zeta\right)^2\mathrm{d}f &= \int\left(\triangle\zeta\right)\underbrace{\left(\vec{\nabla}\right)^2}_{=\triangle}\left(\delta\zeta\right)\mathrm{d}f \\ &= \underbrace{\int\vec{\nabla}\cdot\left(\left(\triangle\zeta\right)\vec{\nabla}(\delta\zeta)\right)\mathrm{d}f}_{=:S_1} - \underbrace{\int\left(\vec{\nabla}(\triangle\zeta)\right)\cdot\vec{\nabla}(\delta\zeta)\,\mathrm{d}f}_{=:S_2}\,.\end{aligned}$$

Using Gauss' Law, $S_1$ transforms to an integral over the plate boundaries,

$$S_1 = \oint\left(\triangle\zeta\right)\left(\vec{\nabla}(\delta\zeta)\right)\cdot\vec{n}\,\mathrm{d}l = \oint\left(\triangle\zeta\right)\left(\partial_n(\delta\zeta)\right)\mathrm{d}l\,,$$

where $\vec{n}$ is the vector in the $x-y$-plane normal to the plate boundary and $\partial_n = \vec{n}\cdot\vec{\nabla}$ is the derivative along this direction, see figure A.3 (a).

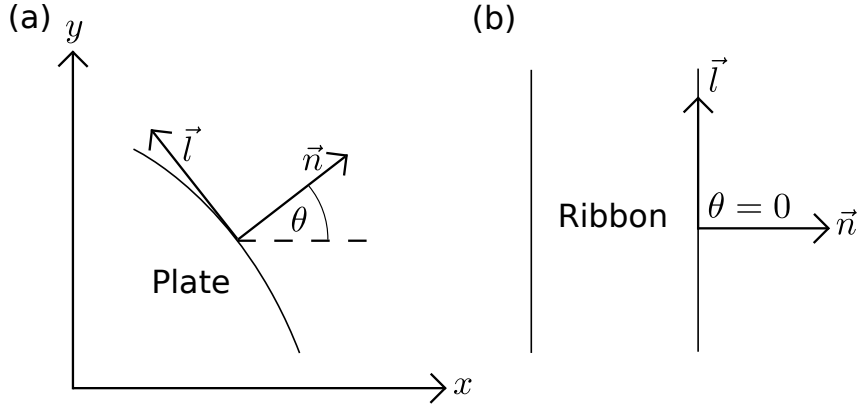


Figure A.3.: The line element $\mathrm{d}l$ refers to the tangential $\vec{l}$ and the derivative $\partial_n$ to the normal $\vec{n}$ ((a) and (b)). For a rectangular ribbon ((b) and figure 5.1) $\cos\theta$ and $\sin\theta$ terms greatly simplify (A.25) and (A.26).

With Gauss' Law once again, $S_2$ becomes

$$\begin{aligned}S_2 &= \int\vec{\nabla}\left(\delta\zeta\left(\vec{\nabla}(\triangle\zeta)\right)\right)\mathrm{d}f - \int\delta\zeta\vec{\nabla}\left(\vec{\nabla}(\triangle\zeta)\right)\mathrm{d}f \\ &= \oint\delta\zeta\left(\vec{\nabla}(\triangle\zeta)\right)\cdot\vec{n}\,\mathrm{d}l - \int\delta\zeta\triangle(\triangle\zeta)\,\mathrm{d}f \\ &= \oint\delta\zeta\partial_n(\triangle\zeta)\,\mathrm{d}l - \int\delta\zeta\left(\triangle^2\zeta\right)\mathrm{d}f\,.\end{aligned}$$

Now, the variation of the first term in (A.18) can be written as

$$\frac{1}{2}\delta\int(\triangle\zeta)^2\,\mathrm{d}f=\int\delta\zeta\triangle^2\zeta\,\mathrm{d}f-\oint\delta\zeta\partial_n(\triangle\zeta)\,\mathrm{d}l+\oint\triangle\zeta\partial_n(\delta\zeta)\,\mathrm{d}l\,. \tag{A.19}$$

Again omitting the prefactor, we vary the second term in (A.18):

$$\begin{aligned}&\delta\int\left((\partial_x\partial_y\zeta)^2-\left(\partial_x^2\zeta\right)\left(\partial_y^2\zeta\right)^2\right)\mathrm{d}f\\&\quad=\int\left(2(\partial_x\partial_y\zeta)(\partial_x\partial_y(\delta\zeta))-\left(\partial_x^2(\delta\zeta)\right)\left(\partial_y^2\zeta\right)-\left(\partial_x^2\zeta\right)\left(\partial_y^2(\delta\zeta)\right)\right)\mathrm{d}f\,.\end{aligned}$$

For the integrand we use the equality

$$\begin{aligned}&\partial_x\underbrace{\left(\partial_y(\delta\zeta)\partial_x\partial_y\zeta-\partial_x(\delta\zeta)\partial_y^2\zeta\right)}_{=:v_x}+\partial_y\underbrace{\left(\partial_x(\delta\zeta)\partial_x\partial_y\zeta-\partial_y(\delta\zeta)\partial_x^2\zeta\right)}_{=:v_y}\\&\quad=\partial_x\partial_y(\delta\zeta)\partial_x\partial_y\zeta+\partial_y(\delta\zeta)\partial_x^2\partial_y\zeta-\partial_x^2(\delta\zeta)\partial_y^2\zeta-\partial_x(\delta\zeta)\partial_x\partial_y^2\zeta\\&\qquad+\partial_x\partial_y(\delta\zeta)\partial_x\partial_y\zeta+\partial_x(\delta\zeta)\partial_x\partial_y^2\zeta-\partial_y^2(\delta\zeta)\partial_x^2\zeta-\partial_y(\delta\zeta)\partial_x^2\partial_y\zeta\\&\quad=2\partial_x\partial_y\zeta\partial_x\partial_y(\delta\zeta)-\partial_x^2(\delta\zeta)\partial_y^2\zeta-\partial_y^2(\delta\zeta)\partial_x^2\zeta\,,\end{aligned}$$

where the left hand side is the divergence of a two-dimensional vector $\vec{v}$. Integrating this divergence, we find

$$\begin{aligned}&\int(\partial_x v_x+\partial_y v_y)\,\mathrm{d}f=\oint\vec{v}\cdot\vec{n}\,\mathrm{d}l\\&\quad=\oint\left(\underbrace{\cos\theta\left(\partial_y(\delta\zeta)\partial_x\partial_y\zeta-\partial_x(\delta\zeta)\partial_y^2\zeta\right)}_{=n_xv_x}+\underbrace{\sin\theta\left(\partial_x(\delta\zeta)\partial_x\partial_y\zeta-\partial_y(\delta\zeta)\partial_x^2\zeta\right)}_{=n_yv_y}\right)\mathrm{d}l\,.\end{aligned}$$

On the plate boundaries we can express the partial derivations by

$$\partial_x=\cos\theta\partial_n-\sin\theta\partial_l\,,\quad\partial_y=\sin\theta\partial_n+\cos\theta\partial_l\,,$$

and find

$$\begin{aligned}&\oint\big\{\cos\theta\left(\sin\theta\partial_n(\delta\zeta)\partial_y\partial_y\zeta+\cos\theta\partial_l(\delta\zeta)\partial_x\partial_y\zeta-\cos\theta\partial_n(\delta\zeta)\partial_y^2\zeta+\sin\theta\partial_l(\delta\zeta)\partial_y^2\zeta\right)\\&\qquad+\sin\theta\left(\cos\theta\partial_n(\delta\zeta)\partial_x\partial_y\zeta-\sin\theta\partial_l(\delta\zeta)\partial_x\partial_y\zeta-\sin\theta\partial_n(\delta\zeta)\partial_x^2\zeta-\cos\theta\partial_l(\delta\zeta)\partial_x^2\zeta\right)\big\}\,\mathrm{d}l\\&\quad=\oint\partial_n(\delta\zeta)\left(2\sin\theta\cos\theta\partial_x\partial_y\zeta-\cos^2\theta\partial_y^2\zeta-\sin^2\theta\partial_x^2\theta\right)\mathrm{d}l\\&\qquad+\oint\partial_l(\delta\zeta)\left(\cos^2\theta\partial_x\partial_y\zeta+\sin\theta\cos\theta\partial_y^2\zeta-\sin^2\theta\partial_x\partial_y\zeta-\sin\theta\cos\theta\partial_x^2\zeta\right)\mathrm{d}l\\&\quad=\oint\partial_n(\delta\zeta)\left(2\sin\theta\cos\theta\partial_x\partial_y\zeta-\sin^2\theta\partial_x^2\zeta-\cos^2\theta\partial_y^2\zeta\right)\mathrm{d}l\\&\qquad+\oint\partial_l(\delta\zeta)\left(\sin\theta\cos\theta\left(\partial_y^2\zeta-\partial_x^2\zeta\right)+\left(\cos^2\theta-\sin^2\theta\right)\partial_x\partial_y\zeta\right)\mathrm{d}l\,.\end{aligned}$$

By partial integration the very last integral becomes

$$\underbrace{\oint \partial_l \left((\delta\zeta)\left(\sin\theta\cos\theta\left(\partial_y^2\zeta - \partial_x^2\zeta\right) + \left(\cos^2\theta - \sin^2\theta\right)\partial_x\partial_y\zeta\right)\right) \mathrm{d}l}_{=0}$$
$$- \oint (\delta\zeta)\partial_l \left(\sin\theta\cos\theta\left(\partial_y^2\zeta - \partial_x^2\zeta\right) + \left(\cos^2\theta - \sin^2\theta\right)\partial_x\partial_y\zeta\right) \mathrm{d}l\,,$$

such that

$$\begin{aligned}
\delta \int \left((\partial_x\partial_y\zeta)^2 - \left(\partial_x^2\zeta\right)\left(\partial_y^2\zeta\right)^2\right) & \\
= & \oint \partial_n(\delta\zeta)\left(2\sin\theta\cos\theta\partial_x\partial_y\zeta - \sin^2\theta\partial_x^2\zeta - \cos^2\theta\partial_y^2\zeta\right) \mathrm{d}l \\
& - \oint (\delta\zeta)\partial_l \left(\sin\theta\cos\theta\left(\partial_y^2\zeta - \partial_x^2\zeta\right) + \left(\cos^2\theta - \sin^2\theta\right)\partial_x\partial_y\zeta\right) \mathrm{d}l\,. \qquad \text{(A.20)}
\end{aligned}$$

Restoring all constants and with (A.19) and (A.20) we get the variation of the free energy,

$$\begin{aligned}
\delta F_{Pl} = & \kappa \Bigg\{ \int \delta\zeta \triangle^2\zeta \,\mathrm{d}f \qquad \text{(A.21)} \\
& - \oint \delta\zeta \,(\partial_n(\triangle\zeta) \\
& \qquad +(1-\sigma)\partial_l \left(\sin\theta\cos\theta\left(\partial_y^2\zeta - \partial_x^2\zeta\right) + \left(\cos^2\theta - \sin^2\theta\right)\partial_x\partial_y\zeta\right)\Big) \mathrm{d}l \\
& + \oint \partial_n(\delta\zeta)\left(\triangle\zeta + (1-\sigma)\left(2\sin\theta\cos\theta\partial_x\partial_y\zeta - \sin^2\theta\partial_x^2\zeta - \cos^2\theta\partial_y^2\zeta\right)\right) \mathrm{d}l \Bigg\}\,,
\end{aligned}$$

where we have introduced the *bending rigidity*

$$\kappa = \frac{\mathcal{E}h^3}{12(1-\sigma^2)}\,. \qquad \text{(A.22)}$$

In order to get the total energy minimum we have to add the potential energy. The potential energy is minus the work performed against external forces. Therefore, its variation $\delta U$ is

$$\delta U = -\int P_z \delta\zeta \,\mathrm{d}f\,,$$

where $P_z$ is an external force per area that acts perpendicular to the $x-y$-plane. Finally, the equilibrium condition is given by

$$\delta F_{Pl} - \delta U = 0\,. \qquad \text{(A.23)}$$

There are area and line integrals on the left hand side. The area integral

$$\int \left(\kappa\triangle^2\zeta - P_z\right)\delta\zeta \,\mathrm{d}f$$

only vanishes for arbitrary $\delta\zeta$ if

$$\kappa\triangle^2\zeta - P_z = 0\,. \qquad \text{(A.24)}$$

This equation describes equilibrium for out-of-plane deformations. The line integrals in (A.23) need to vanish as well, and this translates to boundary conditions. For free floating edges, $\delta\zeta$ and $\partial_n\delta\zeta$ may take any values at the boundaries such that the coefficients of the line integrals in (A.21), (A.23) have to vanish:

$$-\partial_n(\triangle\zeta) + (1-\sigma)\partial_l\left(\cos\theta\sin\theta\left(\frac{\partial^2\zeta}{\partial x^2} - \frac{\partial^2\zeta}{\partial y^2}\right) + \left(\sin^2\theta - \cos^2\theta\right)\frac{\partial^2\zeta}{\partial x\partial y}\right) = 0\,, \quad \text{(A.25)}$$

$$\triangle\zeta + (1-\sigma)\left(2\sin\theta\cos\theta\frac{\partial^2\zeta}{\partial x\partial y} - \sin^2\theta\frac{\partial^2\zeta}{\partial x^2} - \cos^2\theta\frac{\partial^2\zeta}{\partial y^2}\right) = 0\,. \quad \text{(A.26)}$$

In the special case of a rectangular plate aligned along the $x$- and $y$-axes (figures A.3 (b) and 5.1) and with periodic boundaries along the $y$-axis, (A.25) becomes

$$\begin{aligned} 0 &= \mp\partial_x(\triangle\zeta) \pm (1-\sigma)\partial_y\left(-\frac{\partial^2\zeta}{\partial x\partial y}\right) \\ &= \pm\left(-\partial_x^3\zeta\partial_x\partial_y^2\zeta - (1-\sigma)\partial_x\partial_y^2\zeta\right) \\ &= \partial_x^3\zeta + (2-\sigma)\partial_x\partial_y^2\zeta = 0\,. \end{aligned} \quad \text{(A.27)}$$

Accordingly, (A.26) can be written as

$$0 = \partial_x^2\zeta + \partial_y^2\zeta + (1-\sigma)\left(-\frac{\partial^2\zeta}{\partial y^2}\right) = \partial_x^2\zeta + \sigma\partial_y^2\zeta\,,$$

such that (A.27) simplifies to

$$\begin{aligned} 0 &= -\sigma\partial_x\partial_y^2\zeta + (2-\sigma)\partial_x\partial_y^2\zeta \\ &= 2(1-\sigma)\partial_x\partial_y^2\zeta\,. \end{aligned}$$

That is, with open boundaries the out-of-plane displacements of the plate need to satisfy

$$\partial_x^2\zeta + \sigma\partial_y^2\zeta = 0\,, \quad \text{(A.28)}$$

$$\partial_x\partial_y^2\zeta = 0 \quad \text{(A.29)}$$

along its edges.

**In-plane deformations**

Another type of deformation is one that takes place within the plane of the plate with no bending involved. Again, we assume homogeneous deformations for sufficiently thin plates such that the strain tensor only depends on $x$ and $y$. Usually, such deformations arise from forces acting on the plate edges or on the plate volume (like gravity) such that no forces act on the surface of the plate. A vanishing force per surface element means $\sigma_{ik}\eta_k = 0$, see (A.9). As there is no bending for in-plane deformations the normal vector points along the $z$-axis and we infer

$$\sigma_{xz} = \sigma_{yz} = \sigma_{zz} = 0\,.$$

Since the stress tensor can be expressed in terms of the strain tensor, it must be homogenous about the thickness of the plate, as well. From the above conditions and (A.16) we derive

$$u_{xz} = u_{yz} = 0\,, \quad u_{zz} = -\frac{\sigma}{1-\sigma}(u_{xx} + u_{yy})\,.$$

Using (A.16) again, the non-vanishing components of the strain tensor are

$$\sigma_{xx} = \frac{\mathcal{E}}{1-\sigma^2}(u_{xx} + \sigma u_{yy})\,, \quad \sigma_{yy} = \frac{\mathcal{E}}{1-\sigma^2}(u_{yy} + \sigma u_{xx})\,, \quad \sigma_{xy} = \frac{\mathcal{E}}{1+\sigma}u_{xy}\,. \tag{A.30}$$

For a free floating plate, no forces act on the plate edges,

$$\sigma_{ik} n_k = 0\,, \tag{A.31}$$

where $\vec{n}$ is the vector in the plate plane and normal to the plate boundary ($n_i$ takes the role of $\mathrm{d}f_i$ in figure A.1). As above, we explicitly treat the special case of a rectangular plate as depicted in figure A.3 (b). Since $\vec{n} = (\pm 1, 0, 0)$, the $\sigma_{xx}$ and $\sigma_{yx}$ components of the stress tensor must vanish along the edges. That is, the deformations need to satisfy

$$\begin{aligned} & \sigma_{xx} = \frac{\mathcal{E}}{1-\sigma^2}(u_{xx} + \sigma u_{yy}) = 0\,, \\ \Rightarrow \quad & \partial_x u_x + \sigma \partial_y u_y = 0\,, \qquad (A.32) \\ & \sigma_{xy} = \frac{\mathcal{E}}{1+\sigma} u_{xy} = 0\,, \\ \Rightarrow \quad & \partial_x u_y + \partial_y u_x = 0\,, \qquad (A.33) \end{aligned}$$

at the plate boundaries.

Due to homogeneity along the $z$-direction we can use $P_i = F_i h$ in (A.8), such that the plate is in equilibrium if the equations

$$\begin{aligned} h\left(\frac{\partial \sigma_{xx}}{\partial x} + \frac{\partial \sigma_{xy}}{\partial y}\right) + P_x &= 0\,, \\ h\left(\frac{\partial \sigma_{xy}}{\partial x} + \frac{\partial \sigma_{yy}}{\partial y}\right) + P_y &= 0 \end{aligned}$$

are satisfied. Inserting (A.30) into these equations, we get

$$\begin{aligned} \mathcal{E}h\left(\frac{1}{1-\sigma^2}\frac{\partial^2 u_x}{\partial x^2} + \frac{1}{2(1+\sigma)}\frac{\partial^2 u_x}{\partial y^2} + \frac{1}{2(1-\sigma)}\frac{\partial^2 u_y}{\partial x \partial y}\right) + P_x &= 0\,, \\ \mathcal{E}h\left(\frac{1}{1-\sigma^2}\frac{\partial^2 u_y}{\partial y^2} + \frac{1}{2(1+\sigma)}\frac{\partial^2 u_y}{\partial x^2} + \frac{1}{2(1-\sigma)}\frac{\partial^2 u_x}{\partial x \partial y}\right) + P_y &= 0\,. \end{aligned}$$

With

$$\begin{aligned} B_{3D} &:= \mu_{3D} + \lambda_{3D} \overset{(A.14)}{=} \frac{\mathcal{E}}{2(1+\sigma)} + \frac{E\sigma}{(1-2\sigma)(1+\sigma)} = \frac{\mathcal{E}(1-2\sigma) + 2\mathcal{E}\sigma}{2(1-2\sigma)(1+\sigma)} \\ &= \frac{\mathcal{E}}{2(1+\sigma-2\sigma-2\sigma^2)} = \frac{\mathcal{E}}{2(1-\sigma-2\sigma^2)} \approx \frac{\mathcal{E}}{2(1-\sigma)}\,, \qquad (A.34) \\ B_{3D} + \mu_{3D} &= 2\mu_{3D} + \lambda_{3D} \overset{(A.14)}{=} \frac{\mathcal{E}}{1+\sigma} + \frac{\mathcal{E}\sigma}{(1-2\sigma)(1+\sigma)} = \frac{\mathcal{E}(1-2\sigma) + \mathcal{E}\sigma}{(1+\sigma)(1-2\sigma)} \\ &= \frac{\mathcal{E}(1-\sigma)}{(1+\sigma)(1-2\sigma)} = \frac{\mathcal{E}(1-2\sigma-\sigma^2)}{(1-\sigma^2)(1-2\sigma)} \approx \frac{\mathcal{E}}{1-\sigma^2} \qquad (A.35) \end{aligned}$$

we can express the bulk ($B_{3D}$) and shear ($\mu_{3D}$) moduli of a three-dimensional body in terms of its Young's modulus and Poisson's ratio[4]. Due to homogeneity it is common to consider $\mu := \mu_{3D}h$ and $B := B_{3D}h$ for thin plates such that the equations for in-plane equilibrium become

$$(B+\mu)\frac{\partial^2 u_x}{\partial x^2} + \mu\frac{\partial^2 u_x}{\partial y^2} + B\frac{\partial^2 u_y}{\partial x \partial_y} + P_x = 0\,, \tag{A.36}$$

$$(B+\mu)\frac{\partial^2 u_y}{\partial y^2} + \mu\frac{\partial^2 u_y}{\partial x^2} + B\frac{\partial^2 u_x}{\partial x \partial_y} + P_y = 0\,. \tag{A.37}$$

[4]Since $\sigma \in [0,\, 0.5]$ it is arguable wether these approximations are justified but they seem to be common in literature, [Landau & Lifschitz], [Mariani (2009)], [Suzuura (2002)]. For our choice of Poisson's ratio, $\sigma = 0.16$, $\sigma^2 = 0.0256 \ll 1$ is indeed true.

# B. Theorems about ordinary differential equations

The ODE in section 5.3 can be solved with the appropriate theorems from calculus, (see e. g. [Denk (2006)]). The first theorem applies for out-of-plane vibrations, (5.5), and the second for in-plane vibrations, (5.6). While the first theorem is included in the second we treat both theorems separately for convenience.

### Theorem 1

- Let

$$x^{(k)}(t) + a_1 x^{(k-1)}(t) + \cdots + a_k x(t) = 0 \tag{B.1}$$

be an ODE with constant coefficients. We define

$$y(t) := \begin{pmatrix} x(t) \\ x'(t) \\ \vdots \\ x^{(k-1)}(t) \end{pmatrix} \quad \text{and} \quad A := \begin{pmatrix} 0 & 1 & & \\ & \ddots & \ddots & \\ & & 0 & 1 \\ -a_k & -a_{k-1} & \cdots & -a_1 \end{pmatrix}.$$

Then (B.1) is equivalent to $y'(t) = Ay(t)$.

- Theorem

  (a) The characteristic polynomial of matrix $A$ is given by

$$\chi_A(\lambda) := \det(\lambda \mathbb{I}_k - A) = \lambda^k + a_1\lambda^{k-1} + \cdots + a_{k-1}\lambda + a_k\,.$$

  (b) Let $\lambda$ be a $p$-fold root of $\chi_A$. Then it follows that

$$x_1(t) := e^{\lambda t}\,, \quad x_2(t) := te^{\lambda t}\,, \quad \ldots\,, \quad x_p(t) := t^{p-1}e^{\lambda t}$$

  are linear independent solutions to the differential equation (B.1). Considering these solutions for all roots of $\chi_A$ leads to a fundamental system.

### Theorem 2

- Consider the ODE

$$y'(t) = Ay(t)\,, \quad (t \in \mathbb{R})\,, \tag{B.2}$$

where $A \in \mathbb{C}^{n\times n}$ is a constant matrix.

- It is known from algebra that there exists an invertible matrix $S$ with which we can transform $A$ to its Jordan canonical form,

$$S^{-1}AS = \begin{pmatrix} J(\lambda_1) & & & & \\ & \ddots & & & \\ & & J(\lambda_1) & & \\ & & & J(\lambda_2) & \\ & & & & \ddots \end{pmatrix},$$

where $\lambda_i$ are pairwise different eigenvalues of $A$, and

$$J_p(\lambda_i) = \begin{pmatrix} \lambda_i & 1 & & \\ & \ddots & \ddots & \\ & & \lambda_i & 1 \\ & & & \lambda_i \end{pmatrix}$$

is a Jordan block of appropriate dimension $p$. There might be more than one Jordan block for one $\lambda_i$.

- For each Jordan block, there are generalized eigenvectors $h_1, \ldots, h_p$ which are characterized by

$$(A - \lambda_i \mathbb{I}_n)h_j = h_{j-1}\,, \quad (j = 1, \ldots, p)\,,$$

with $h_0 := 0$. Consequently, $h_1$ is an eigenvector and $h_j$ is a generalized eigenvector of level $j$. The invertible matrix $S$ consists of all the generalized eigenvectors of matrix $A$. This can be seen by defining $h_j := Se_j$ ($j$-th column of Matrix $S$). Then

$$S^{-1}ASe_j = \lambda e_j + e_{j-1}$$

means

$$Ah_j = S(\lambda e_j + e_{j-1}) = \lambda h_j + h_{j-1}\,, \Rightarrow (A - \lambda \mathbb{I}_n)h_j = h_{j-1}\,. \quad \checkmark$$

- Theorem

Be $h_j$ ($j = 1, \ldots, p$) the generalized eigenvector of level $j$ to the eigenvalue $\lambda$ of Matrix $A$. Then

$$y_j(t) := e^{\lambda t}\left(h_j + th_{j-1} + \frac{t^2}{2}h_{j-2} + \cdots + \frac{t^{j-1}}{(j-1)!}h_1\right)$$

is a solution of the differential equation (B.2). The system of all these solution (for all Jordan blocks) constitutes a fundamental system.

# Bibliography


[Ashcroft] Neil W. Ashcroft and David N. Mermin, *Festkörperphysik*, 3. Auflage, Oldenburg Wissenschaftsverlag, 2007

[Bennett (1993)] Charles H. Bennett, Gilles Brassard, Claude Crépeau, Richard Jozsa, Asher Peres and William K. Wootters, *Teleporting an unknown quantum state via dual classical and Einstein-Podolsky-Rosen channels*, Physical Review Letters **70**, 1993

[Bolotin (2008)] K. I. Bolotin, K. J. Sikes, J. Hone, H. L. Stormer and P. Kim, *Temperature-Dependent Transport in Suspended Graphene*, Physical Review Letters **101**, 2008

[Brey (2006)] L. Brey and H. A. Fertig, *Electronic states of graphene nanoribbons studied with the Dirac equation*, Physical Review B **73**, 2006

[Brennen (1999)] Gavin K. Brennen, Carlton M. Caves, Poul S. Jessen and Ivan H. Deutsch, *Quantum Logic Gates in Optical Lattices*, Physical Review Letters **82**, 1999

[Burkard (QII)] Guido Burkard, *Höhere Quantenmechanik und Elektrodynamik*, Wintersemester 2008/09, Universität Konstanz (Fachbereich Physik), 2009

[Castro Neto (2009)] A. H. Castro Neto, F. Guinea, N. M. R. Peres, K. S. Novoselov and A. K. Geim, *The electronic properties of graphene*, Reviews of Modern Physics **81**, 2009

[Cirac (1995)] J. I. Cirac and P. Zoller, *Quantum Computations with Cold Trapped Ions*, Physical Review Letters **74**, 1995

[Chaikin & Lubensky] P. M. Chaikin and T. C. Lubensky, *Principles of condensed matter physics*, Cambridge University Press, 1995

[Chen (2008)] Jian-Hao Chen, Chaun Jang, Shudong Xiao, Masa Ishigami and Michael S. Fuhrer, *Intrinsic and extrinsic performance limits of graphene devices in* $SiO_2$; Nature Nanotechnology **3**, 2008

[Chirolli (2008)] Luca Chirolli and Guido Burkard, *Decoherence in solid-state qubits*, Advances in Physics **57**, 2008

[Chuang (1998)] Isaac L. Chuang, Neil Gershenfeld and Mark Kubinec, *Experimental Implementation of Fast Quantum Searching*, Physical Review Letters **80**, 1998

[Dato (2009)] We thank the group for permission to use this figure. Resource: Alberto Dato, Zonghoon Lee, Ki-Joon Jeon, Rolf Erni, Velimir Radmilovic, Thomas J. Richardson and Michael Frenklach, *Clean and highly ordered graphene synthesized in the gas phase*, Chemical Communications **40**, 2009

[Denk (2006)] Robert Denk, *Skript zur Vorlesung Analysis III*, Wintersemester 2005/06, Universität Konstanz (Fachbereich Mathematik und Statistik), 2006

[Devoret (2004)] M. H. Devoret, A. Wallraff and J. M. Martinis, *Superconducting Qubits: A Short Review*, arXiv:cond-mat/0411174v1, 2004

[DiVincenzo (1999)] D. P. DiVincenzo, G. Burkard, D. Loss and E. V. Sukhorukov, *Quantum computation and spin electronics*, arXiv:cond-mat/9911245v1; Published in *Quantum Mesoscopic Phenomena and Mesoscopic Devices in Microelectronics*, eds. I. O. Kulik and R. Ellialtioglu (NATO Advanced Study Institute, Turkey, June 13-25, 1999)

[Faccio (2009)] Ricardo Faccio, Pablo A. Denis, Helena Pardo, Cacilia Goyenola and Álvaro W. Mombrú, *Mechanical properties of graphene nanoribbons*, Journal of Physics: Condensed Matter **21**, 2009

[Falkovsky (2008)] L. A. Falkovsky, *Symmetry constraints on phonon dispersion in graphene*, Physics Letters A **372**, 2008

[Fasolino (2007)] A. Fasolino, J. H. Los and M. I. Katsnelson, *Intrinsic ripples in graphene*, Nature Materials **6**, 2007

[Fox] Mark Fox, *Optical Properties of Solids*, Oxford University Press, 2001

[Frank (2007)] I. W. Frank, D. M. Tanenbaum, A. M. van der Zande and P. L. McEuen, *Mechanical properties of suspended graphene sheets*, Journal of Vacuum Science and Technology B **25**, 2007

[Gaebel (2006)] Torsten Gaebel, Michael Domhan, Iulian Popa, Christoffer Wittmann, Philipp Neumann, Fedor Jelezko, James R. Rabeau, Nikolas Stavarias, Andrew D. Greentree, Steven Prawer, Jan Meijer, Jason Twamley, Philip R. Heimer and Jörg Wrachtrup, *Room-temperature coherent coupling of single spins in diamond*, Nature Physics **2**, 2006

[Gazit (2009)] Doron Gazit, *Theory of spontaneous buckling of doped graphene*, Physical Review B **79**, 2009

[Geim (2007)] Andrey K. Geim and Allan H. MacDonald, *Graphene: Exploring carbon flatland*, Physics Today, August 2007

[Geim (2007-2)] A. K. Geim and K. S. Novoselov, *The rise of graphene*, Nature Materials **6**, 2007

[Gmitra (2009)] M. Gmitra, S. Konschuh, C. Ertler, C. Ambrosch-Draxl and J. Fabian, *Band-structure topologies of graphene: Spin-orbit coupling effects from first principles*, Physical Review B **80**, 2009

[Haken & Wolf] Hermann Haken und Hans Christian Wolf, *Atom- und Quantenphysik*, 7. Auflage, Springer Verlag, 2000

[Hanson (2007)] R. Hanson, L. P. Kouwenhoven, J. R. Petta, S. Tarucha and L. M. K.

Vandersypen, *Spins in few-electron quantum dots*, Reviews of Modern Physics **79**, 2007

[IdqCerberis] IDQ quantum key distribution *Cerberis*, datasheet, www.idquantique.com, 09.06.2010

[Jaksch (1999)] D. Jaksch, H.-J. Briegel, J. I. Cirac, C. W. Gardiner and P. Zoller, *Entanglement of Atoms via Cold Controlled Collisions*, Physical Review Letters **82**, 1999

[Jiao (2009)] Liying Jiao, Li Zhang, Xinran Wang, Georgi Diankov and Hongjie Dai, *Narrow graphene nanoribbons from carbon nanotubes*, Nature **458**, 2009

[Kane (2005)] C. L. Kane and E. J. Mele, *Quantum Spin Hall Effect in Graphene*, Physical Review Letters **95**, 2005

[Katsnelson (2006)] M. I. Katsnelson, K. S. Novoselov and A. K. Geim, *Chiral tunneling and the Klein paradox in graphene*, Nature Physics **2**, 2006

[Khaetskii (2001)] Alexander V. Khaetskii and Yuli V. Nazarov, *Spin-flip transitions between Zeeman sublevels in semiconductor quantum dots*, Pysical Review B **64**, 2001

[Kosynkin (2009)] Dmitry V. Kosynkin, *et al.*, *Longitudinal unzipping of carbon nanotubes to form graphene nanoribbons*, Nature **458**, 2009

[Kudin (2001)] Konstantin N. Kudin and Gustavo E. Scuseria, *$C_2F$, BN, and C nanoshell elasticity from ab initio computations*, Physical Review B **64**, 2001

[Landau & Lifschitz] L. D. Landau and E. M. Lifschitz, *Lehrbuch der theoretischen Physik, Band VII - Elastizitätstheorie*, 7. Auflage, Akademie Verlag, 1991

[Lanyon (2007)] B. P. Lanyon, T. J. Weinhold, N. K. Langford, M. Barbieri, D. F. V. James, A. Gilchrist and A. G. White, *Experimental Demonstration of a Compiled Version of Shor's Algorithm with Quantum Entanglement*, Physical Review Letters **99**, 2007

[Lee (2008)] Changgu Lee, *et al.*, *Measurement of the Elastic Properties and Intrinsic Strength of Monolayer Graphene*, Science **321**, 2008

[Levitt] Malcolm H. Levitt, *spin dynamics*, Wiley, 2005

[Li (2008)] Xiaolin Li, *et al.*, *Chemically Derived, Ultrasmooth Graphene Nanoribbon Semiconductors*, Science **319**, 2008

[Lin (2008)] Yu-Ming Lin, Keith A. Jenkins, Alberto Valdes-Garcia, Joshua P. Small, Damon B. Farmer and Phaedon Avouris, *Operation of Graphene Transistors at Gigahertz Frequencies*, Nano Letters **9**, 2009

[Liu (2009)] P. Liu and Y. W. Zhang, *Temperature-dependent bending rigidity of graphene*, Applied Physics Letters **94**, 2009

[Loss (1998)] Daniel Loss and David P. DiVincenzo, *Quantum computation with quantum dots*, Physical Review A **57**, 1998

[Lu (2007)] Chao-Yang Lu, Daniel E. Browne, Tao Yang and Jian-Wei Pan, *Demonstra-*

*tion of a Compiled Version of Shor's Quantum Factoring Algorithm Using Photonic Qubits*, Physical Review Letters **99**, 2007

[Magiq8505] Magiq QPN Security Gateway *QPN - 8505*, datasheet, www.magiqtech.com, 09.06.2010

[Mariani (2009)] Eros Mariani and Felix von Oppen, *Electron-vibron coupling in suspended carbon nanotube quantum dots*, Physical Review B **80**, 2009

[Mermin (1966)] N. D. Mermin and H. Wagner, *Absence of ferromagnetism or antiferromagnetism in one- or two-dimensional isotropic Heisenberg models*, Physical Review Letters **17**, 1966

[Mermin (1968)] N. D. Mermin, *Crystalline Order in Two Dimensions*, Physical Review **176**, 1968

[Min (2006)] Hongki Min, J. E. Hill, N. A. Sinitsyn, B. R. Sahu, Leonard Kleinman and A. H. MacDonald, *Intrinsic and Rashba spin-orbit interactions in graphene sheets*, Physical Review B **74**, 2006

[Nielsen & Chuang] Michael A. Nielsen and Isaac L. Chuang, *Quantum Computation and Quantum Information*, Cambridge University Press, 2004

[Nolting 5/2] Wolfgang Nolting, *Grundkurs Theoretische Physik 5/2*, 6. Auflage, Springer Verlag, 2006

[Nolting 7] Wolfgang Nolting, *Grundkurs Theoretische Physik 7*, 6. Auflage, Springer Verlag, 2005

[Recher (2010)] Patrick Recher and Björn Trauzettel, *Quantum dots and spin qubits in graphene*, arXiv:1004.2136v1, 2010

[Reddy (2006)] C. D. Reddy, S. Rajendran and K. M. Liew, *Equilibrium configuration and continuum elastic properties of finite sized graphene*, Nanotechnology **17**, 2006

[Rivest (1978)] R. L. Rivest, A. Shamir and L. Adlemand,*A Method for Obtaining Digital Signatures and Public-Key Cryptosystems*, Communications of the Association for Computing Machinery **21**, 1978

[Rössler] Ulrich Rössler, *Solid State Theory*, Springer Verlag, 2004

[Saito (1992)] Riichiro Saito, Mitsutaka Fujita, G. Dresselhaus and M. S. Dresselhaus, *Electronic structure of graphene tubules based on* $C_{60}$, Physical Review B **46**, 1992

[Sánchez-Portal (1999)] Daniel Sánchez-Portal, Emilio Artacho and José M. Soler, *Ab initio structural, elastic, and vibrational properties of carbon nanotubes*, Physical Review B **59**, 1999

[Shor (1994)] Peter W. Shor, *Algorithms for Quantum Computation: Discrete Logrithms and Factoring*, IEEE, 1994

[Shor (1997)] Peter W. Shor, *Polynomial-Time Algorithms for Prime Factorization on a Quantum Computer*, SIAM Journal on Computing **26**, 1997

[Steele (2009)] G. A. Steele, G. Gotz and L. P. Kouwenhoven, *Tunable few-electron double quantum dots and Klein tunneling in ultraclean carbon nanotubes*, Nature Nanotechnology **4**, 2009

[Stoller (2008)] Meryl D. Stoller, Sungjin Park, Yanwu Zhu, Jinho An and Rodney S. Ruoff, *Graphene-Based Ultracapacitors*, Nano Letters **8**, 2008

[Struck (2010)] Philipp R. Struck and Guido Burkard, *Effective time-reversal symmetry breaking in the spin relaxation in a graphene quantum dot*, arXiv:1003.2088v1

[Sutton] Adrian P. Sutton, *Elektronische Struktur in Materialien*, VCH Verlagsgesellschaft, 1996

[Suzuura (2002)] Hidekatsu Suzuura and Tsuneya Ando, *Phonons and electron-phonon scattering in carbon nanotubes*, Physical Review B **65**, 2002

[Svore (2005)] Krysta M. Svore, Barbara M. Terhal and David P. DiVincenzo, *Local fault-tolerant quantum computation*, Physical Review A **72**, 2005

[Szkopek (2008)] We thank Thomas Szkopek for permission to use this figure. Resource: http://www.ece.mcgill.ca/∼ts7kop/images/graphene_xyz.jpg

[Trauzettel (2007)] Björn Trauzettel, Denis V. Bulaev, David Loss and Guido Burkard, *Spin qubits in graphene quantum dots*, Nature Physics **3**, 2007

[Ursin (2004)] Rupert Ursin, Thomas Jennewein, Markus Aspelmeyer, Rainer Kaltenbaek, Michael Lindenthal, Philip Walther and Anton Zeilinger, *Quantum teleportation across the Danube*, Nature **430**, 2004

[Ursin (2007)] R. Ursin, F. Tiefenbacher, T. Schmitt-Manderbach, H. Weier, T. Scheidl, M. Lindenthal, B. Blauensteiner, T. Jennewein, J. Perdigues, P. Trojek, B. Ömer, M. Fürst, M. Meyenburg, J. Rarity, Z. Sodnik, C. Barbieri, H. Weinfurter and A. Zeilinger, *Entanglement-based quantum communication over 144 km*, Nature Physics **3**, 2007

[Ursin (2009)] R. Ursin *et al.*, *Space-quest, experiments with quantum entanglement in space*, Europhysics News **40**, 2009

[Vandersypen (2001)] Lieven M. K. Vandersypen, Matthias Steffen, Gregory Breyta, Costantino S. Yannoni, Mark H. Sherwood and Isaac L. Chuang, *Experimental realization of Shor's quantum factoring algorithm using nuclear magnetic resonance*, Nature **414**, 2001

[Van Vleck (1940)] J. H. Van Vleck, *Paramagnetic Relaxation Times for Titanium and Chrome Alum*, Physical Review **57**, 1940

[Varykhalov (2008)] A. Varykhalov, J. Sánchez-Barriga, A. M. Shikin, C. Biswas, E. Vescovo, A. Rybkin, D. Marchenko and O. Rader, *Electronic and Magnetic Properties of Quasifreestanding Graphene on Ni*, Physical Review Letters **101**,2008

[Wallace (1947)] P. R. Wallace, *The Band Theory of Graphite*, Physical Review **71**, 1947

[Wei (2010)] Zhongqing Wei, Debin Wang, Suenne Kim, Soo-Young Kim, Yike Hu,

Michael K. Yakes, Arnaldo R. Laracuente, Zhenting Dai, Seth R. Marder, Claire Berger, William P. King, Walter A. de Heer, Paul E. Sheehan and Elisa Riedo, *Nanoscale Tunable Reduction of Graphene Oxide for Graphene Electronics*, Science **328**, 2010

[Wu (2010)] Qiong Wu, Yuxi Zu, Zhiyi Yao, Anran Liu and Gaoquan Shi, *Supercapacitors Based on Flexible Graphene/Polyaniline Nanofiber Composite Films*, ACS Nano **4**, 2010

[Yu & Cardona] Peter Y. Yu and Manuel Cardona, *Fundamentals of Semiconductors*, 3rd edition, Springer Verlag, 2001

[Zhang (2006)] Y. Zhang, *et al.*, *Landau-Level Splitting in Graphene in High Magnetic Fields*, Physical Review Letters **96**, 2006